

PORTABLE INSTRUMENTATION FOR UV-VISIBLE SPECTROSCOPY OF AMBIENT AND
LABORATORY-GENERATED AEROSOLS

by

D. ALPHONSE FISCHER, JR.

(Under the Direction of Geoffrey D. Smith)

ABSTRACT

Aerosols directly affect Earth's climate by scattering and absorbing solar radiation. Although they are ubiquitous in Earth's atmosphere, direct, *in-situ*, wavelength-resolved measurements of aerosol optical properties remain elusive. As a result, the so-called aerosol direct effects are one of the largest uncertainties in predictions of Earth's future climate, and new instrumentation is needed to provide measurements of the scattering and absorption of sunlight by atmospheric particles, especially in the UV. This work involved the development of three pieces of equipment to address the gap in instrumentation: (1) a UV-visible broadband cavity enhanced spectrometer for the measurement of wavelength-resolved extinction from 375–700 nm; (2) a four-wavelength, single-cell photoacoustic spectrometer for simultaneous measurement of aerosol absorption at 406, 532, 662, and 780 nm; and (3) a three-wavelength, single-cell UV photoacoustic spectrometer for measurements of absorption at 320, 377, and 445 nm. Extra effort has been made to make these instruments compact and robust while maintaining exceptional detection limits ($< 1 \text{ Mm}^{-1}$ of absorption/extinction). Various versions of these instruments, and their earlier prototypes have been used in collaborations at other laboratories to make the first measurements of the Ångström exponent (the wavelength dependence to extinction/absorption) of flame-generated soot in the UV, to test traditional

calibration methods for photoacoustic spectroscopy, to validate methods of measuring aerosol absorption, and in international intercomparisons of aerosol absorption measurements.

INDEX WORDS: Photoacoustic spectroscopy, Cavity enhanced spectroscopy, Aerosols, Black carbon, Brown carbon, Soot, Climate change

PORTABLE INSTRUMENTATION FOR UV-VISIBLE SPECTROSCOPY OF AMBIENT AND
LABORATORY-GENERATED AEROSOLS

by

D. ALPHONSE FISCHER, JR.

BS, The Evergreen State College, 2011

A Dissertation Submitted to the Graduate Faculty
of The University of Georgia in Partial Fulfillment

of the

Requirements for the Degree

DOCTOR OF PHILOSOPHY

ATHENS, GEORGIA

2018

© 2018 D. Alphonse Fischer, Jr.

All Rights Reserved

PORTABLE INSTRUMENTATION FOR UV-VISIBLE SPECTROSCOPY OF AMBIENT AND
LABORATORY-GENERATED AEROSOLS

by

D. ALPHONSE FISCHER, JR.

Approved:

Major Professor: Geoffrey D. Smith

Committee: Gary E. Douberly
Michael A. Duncan

Suzanne Barbour
Dean of the Graduate School
The University of Georgia
May 2018

In memory of my dad, Donald A. Fischer, Sr.

Thanks for getting me here.

ACKNOWLEDGMENTS

This work has been made possible by numerous people and agencies along the way. I gratefully acknowledge the support of the University of Georgia Graduate School and the UGA Philbrook Scholarship Fund for providing a research fellowship for the first several years of my graduate career; I also acknowledge the support of the National Science Foundation through grants AGS-1241621 and AGS-1638307. The facilities of the UGA Instrument Shop and wisdom and experience of Lewis Fortner were invaluable to this work. I appreciate the collaborators I've worked with along the way, including the scientists involved with the BC4 study (chapter 5) and Rawad Saleh and Zezhen Cheng of the UGA College of Engineering for providing me the opportunity to share my instruments with them and graciously loaning me numerous pieces of equipment and samples.

More personally, I thank my advisor, Dr. Geoffrey Smith, for support, direction, and patience from the time of my first communication with him as a prospective student through to now. The learning environment provided by my professors and mentors at Evergreen was “instrumental” in my pursuit of analytical chemistry and chemical instrumentation (pardon the pun). Those individuals include my undergraduate advisor Dr. Clyde Barlow and supervisor Jenna Nelson, along with many other faculty and students. Similarly, the opportunities afforded me by Hummingbird Scientific provided me with skills that led to my success in graduate school. Finally, I am forever grateful to my family for their continual support, especially the Fischer-Kobussens.

TABLE OF CONTENTS

ACKNOWLEDGMENTS	v
1 INTRODUCTION: EARTH'S ATMOSPHERE	1
1.1 Atmospheric Aerosols	2
1.2 Goals of This Work	7
References	11
2 CAVITY RINGDOWN AND PHASE-SHIFT CAVITY RINGDOWN SPECTROSCOPY	13
2.1 Introduction	13
2.2 Materials and Methods	16
2.3 Results and Discussion	20
2.4 Conclusion	22
References	24
3 A FOUR-CHANNEL, UV-VISIBLE BROADBAND CAVITY ENHANCED SPECTROMETER FOR AMBIENT AEROSOL EXTINCTION	26
3.1 Introduction	26
3.2 Experimental	28
3.3 Results and Discussion	34
3.4 Major Limitations and Recommendations	41
3.5 Conclusion	43

References	45
4 A “HYBRID” LASER-LAMP UV-VISIBLE PHOTOACOUSTIC SPECTROMETER	48
4.1 Introduction	48
4.2 Materials and Methods	50
4.3 Results and Discussion	54
4.4 Summary & Conclusions	57
References	60
5 UV-VISIBLE ABSORPTION SPECTRUM OF LABORATORY-GENERATED SOOT PAR- TICLES	62
5.1 Introduction	63
5.2 Materials and Methods	64
5.3 Results and Discussion	68
5.4 Conclusions	77
5.5 Acknowledgements	78
References	79
6 MULTIPAS-IV: A PORTABLE, FOUR-WAVELENGTH, SINGLE-CELL PHOTOACOUS- TIC SPECTROMETER FOR AMBIENT AEROSOL ABSORPTION	81
6.1 Introduction	82
6.2 Materials and Methods	85
6.3 Instrument Performance	92
6.4 Conclusions and Outlook	106
References	107
7 CAN OZONE BE USED TO CALIBRATE AEROSOL PHOTOACOUSTIC SPECTROM- ETERS?	112

7.1	Introduction	113
7.2	Materials and Methods	115
7.3	Results	119
7.4	Conclusions	125
	References	127
8	MULTIPAS-UV: A PORTABLE, THREE-WAVELENGTH, SINGLE-CELL PHOTOACOUSTIC SPECTROMETER FOR AMBIENT AEROSOL ABSORPTION IN THE UV AND VISIBLE	129
8.1	Introduction	129
8.2	Materials and Methods	130
8.3	Results and Discussion	136
8.4	Conclusions	143
8.5	Acknowledgements	145
	References	146
9	THE SPECTRAL DEPENDENCE OF THE AETHALOMETER CORRECTION FACTOR	148
9.1	Introduction	149
9.2	Materials and Methods	151
9.3	Results and Discussion	155
9.4	Conclusions	159
9.5	Acknowledgements	160
	References	161
10	SUMMARY AND CONCLUSIONS	164
	References	168
	APPENDICES	169

A	SUPPLEMENTAL INFORMATION: A PORTABLE, FOUR-WAVELENGTH, SINGLE-CELL PHOTOACOUSTIC SPECTROMETER FOR AMBIENT AEROSOL ABSORPTION	169
A.1	Comparison to a 7-wavelength Aethalometer	170
A.2	Calibration with Nitrogen Dioxide and Nigrosin	171
	References	180
B	BLOCK DIAGRAM OF THE THREE-WAVELENGTH PAS	183
C	PAS DATA PROCESSING WITH AERO	185
C.1	aeRo Package	185
C.2	Loading Data into R	186
C.3	Exploring MultiPAS Data	187
C.4	Processing the Data	188
C.5	Plotting the Data	188
D	TROUBLESHOOTING THE PAS	189
D.1	Common Software Errors	189
D.2	Common Hardware Errors	190
E	MICROPROCESSOR CODE AND CUSTOM PCB FOR PASS	191
F	OVERVIEW OF MULTIPAS LABVIEW PROGRAM	198
	References	200
G	MICROPROCESSOR CODE AND DIAGRAM FOR BBCES	201

LIST OF FIGURES

1.1	A Portrait of Global Aerosols	4
1.2	Aerosol Radiative Forcing	6
1.3	Hypothetical C_{Br} and BC absorption spectra.	8
2.1	Block diagram of the phase shift cavity ringdown.	17
2.2	Model of the cavity ringdown spectrometer	19
2.3	Ozone cross section measured with PS-CRDS	20
2.4	Absorption of NO_2 measured by the lamp PS-CRDS	21
2.5	NO_2 absorption cross section at 662 nm from CRDS	22
3.1	Diagram of the BBCES	29
3.2	Typical raw intensity and reflectivity spectra from BBCES	32
3.3	NO_2 absorption spectrum and absorption cross sections from BBCES	36
3.4	Typical Allan deviation for each BBCES cell	38
3.5	Comparison of ambient extinction by BBCES and CRDS	39
3.6	Extinction, scattering, and SSA for ambient aerosols	40
3.7	Ambient extinction from BBCES and scattering from nephelometry	42
3.8	BBCES throughput as a function of $1 - L/R$	43
4.1	Block diagram of the lamp PAS	51
4.2	Calibration Curve for the Hybrid PAS	55
4.3	Chlorophyll Spectrum from the Hybrid PAS	56

4.4	Ambeint Spectrum from the Hybrid PAS	58
5.1	Block Diagram of the Experimental Setup for BC4	65
5.2	Comparison of Soot Absorption Measurements at BC4	69
5.3	Nascent Soot Mass Absorption Cross Sections	71
5.4	UV-visible Mass Absorption Spectrum for Nascent Soot Particles	75
5.5	Wavelength-dependence of the BC ΔE	77
6.1	Schematic diagram of the MultiPAS-IV	87
6.2	Detection Limits of MultiPAS-IV	93
6.3	Ambient time series from MP-IV, a 7-wavelength Aethalometer, and SMPS .	96
6.4	Nigrosin aerosol absorption cross sections measured with the MultiPAS-IV .	98
6.5	Time series and histogram of ΔE_{BC} values	100
6.6	Time series and histogram of ΔE_{BC} values	103
7.1	Block Diagram of the Experimental Setup.	116
7.2	Calibrations via Various Methods.	121
7.3	Photolysis of Ozone in the PAS.	122
7.4	Time Series of O ₂ Addition During Ozone Calibration	123
8.1	Schematic diagram of the MultiPAS-UV	132
8.2	Calibration of the MP-UV with NO ₂	137
8.3	Determination of PAS Effective Powers with Nigrosin	139
8.4	Results of Allan Deviation from MP-UV	141
8.5	Spectrum of NIST Carbon Black	142
8.6	Spectrum of Ambient Aerosols Acquired with MP-UV and MP-IV	144
9.1	Block Diagram of Aethalometer-PAS Intercomparison	154
9.2	Comparison of Non-linear and Log-transform Fits	156

9.3	Unscaled Aethalometer Spectrum vs. PAS Spectrum	156
9.4	Comparison of Low- AAE Spectra for PAS and Aethalometer	158
9.5	Wavelength-dependent Correction Factors for the Aethalometer	159
A.1	Microphone Response as a Function of Modulation Frequency	174
A.2	Calibration Curves for the MP-IV	175
A.3	Correlation Plots of Aethalometer and PAS Absorption Measurements	176
A.4	Time series and histograms of AAE_{BC}	177
A.5	AAE for Different Values of α_{785}	178
A.6	Time series and Histograms of Fraction of Absorption Due to C_{Br}	179
B.1	Block Diagram of MultiPAS-III	184
E.1	Electrical Schematic of the MultiPAS PCB	192
E.2	Layout of the MultiPAS PCB	193
F.1	Conceptual Block Diagram of the PAS LabVIEW Program	199
G.1	Block Diagram of the TEC Control Loop for the BBCES	202

LIST OF TABLES

3.1	BBCES Optical Components	30
3.2	Results of Linear Regression with NO_2	35
5.1	Measured Mass Absorption Cross Sections for Black Carbon	72
5.2	Literature Review of MAC_{550} and AÅE.	74
A.1	Comparison of Aerosol PAS Instruments	172

CHAPTER 1

INTRODUCTION: EARTH'S ATMOSPHERE

The Earth's atmosphere (from the Greek *atmos* for “vapor” and *sphaira* for “sphere”) is a relatively thin layer of gases and aerosols that makes up the outer layer of planet Earth. It is held in place by Earth's gravity, and forms a buffer between Earth's solid lithosphere and outer space. The Kármán line is generally accepted as the boundary between outer space and Earth's atmosphere, and lies only 100 km above sea level, the altitude at which the atmosphere becomes too thin to support aeronautical flight.¹ Despite the thin, blanket-like nature of the atmosphere, it is imperative for life. It is composed roughly 21% oxygen, 78% nitrogen, and 1% argon; about 0.05% of the atmosphere is composed of trace gases, including carbon dioxide. Humans and other heterotrophs depend on the oxygen for cellular respiration, while autotrophs depend on the trace carbon dioxide for life. Likewise, CO₂ and other trace gases create a greenhouse effect on Earth that keeps the planet at the “Goldilocks” temperature that is just right for life, while stratospheric ozone protects life from harmful UV rays. [1]

Structurally, the atmosphere is divided into four or five layers, which are primarily defined by temperature. The troposphere is closest to Earth and is where most life resides. It extends up to the tropopause at roughly 10 km above sea level, although the tropopause is specifically defined as the point in the atmosphere at which temperature stops decreasing

¹ This altitude approximately coincides with the turbopause, or the boundary above which atmospheric gases are not well-mixed.

with altitude. Most commercial airliners fly near the tropopause. Above the troposphere is the stratosphere, where weather balloons fly and the ozone layer resides. The temperature in the stratosphere increases with altitude up to the stratopause. The stratopause forms the boundary between the stratosphere and the mesosphere, in which temperature again decreases with altitude. Above the mesosphere is the thermosphere, where the aurora borealis occurs. The thermosphere is bounded on the top by the Kármán line, which is defined as the point at which the speed required to keep an aircraft buoyant is greater than the orbital velocity for the Earth. Sometimes, a fifth layer is cited and termed the exosphere, though this may also be considered “outer space”. [1]

Although the atmosphere sustains and protects life on Earth, it can also have detrimental effects on life. For example, stratospheric ozone protects life from ultraviolet light, but ozone in the troposphere causes lung damage in humans and damages plant tissues. [2, 3] Acid rain, the result of sulfate emissions, is well known to damage vegetation, buildings, and statues. [4, 5] Particulate matter at ground level, especially particulate matter smaller than $2.5\ \mu\text{m}$, causes asthma attacks and lung damage. [6] Further, feedbacks between human activities and the atmosphere can have significant effects around the world. Most notably, the effects of anthropogenic CO_2 on climate are a current global focus of remediation efforts. This work was focused on the UV-visible optical properties of climate-relevant aerosols in the atmosphere, whether natural or anthropogenic.

1.1 Atmospheric Aerosols

Aerosols are ubiquitous in Earth’s atmosphere. They are emitted both naturally and anthropogenically. Figure 1.1 shows a snapshot from a NASA simulation of aerosol movement around the globe. It shows sulfate aerosols that originate from power plants and volcanoes in white, which are especially evident over the northeast United States, Europe, and Southeast Asia. Blueish-white areas show sea salt aerosols generated by breaking ocean waves,

which are seen in the rough seas of the South Pacific and North Atlantic. Green areas show aerosols from biomass burning, including forest fires, agricultural burns, and cooking and heating fires. These are evident in South America, sub-Saharan Africa, and Indonesia, where biomass is abundant and often burnt for agricultural reasons [7, 8] and for heating and cooking (as in West Africa). [9] The most prominent feature in Figure 1.1 is the orange-red dust emitted from the Saharan Desert and transported northward to Europe and westward across the Atlantic to the Americas; these aerosols are prominent enough to cause a demonstrable increase of asthma outbreaks in the Caribbean, trigger red tides that harm the shellfish industry in Florida, and provide the sustaining source of phosphorous for the plants of the Amazon rain forests. [10–14] Also of note are the areas where there are no aerosols. For example, the Tibetan Plateau has few local sources of aerosols and is shielded to the south by the Himalayas that block aerosols from the Indian sub-continent; this makes the Tibetan Plateau one of the cleanest environments on Earth in terms of aerosols. [15] Of course, Figure 1.1 merely provides a snapshot of aerosol activity. Aerosols have a lifetime from roughly 1.5 to 14 days depending on the location. [16] Thus, as sources change based on human activities, natural disasters, and seasonal trends, the portrait of global aerosols will change drastically. Contrast this with carbon dioxide: After 20 centuries, an estimated 60 % of fossil-fuel CO_2 will dissolve into the oceans and reach equilibrium while the remaining 40% remains in the atmosphere. [17] In other words, if aerosol emissions were stopped tomorrow, the effects on climate and air quality would be fully realized in 2 weeks; if CO_2 emissions were stopped tomorrow, the effects would not be seen for centuries. This makes aerosols an attractive target for reduction of global warming, both through reduction of absorbing aerosols and by increasing non-absorbing aerosols. [18]

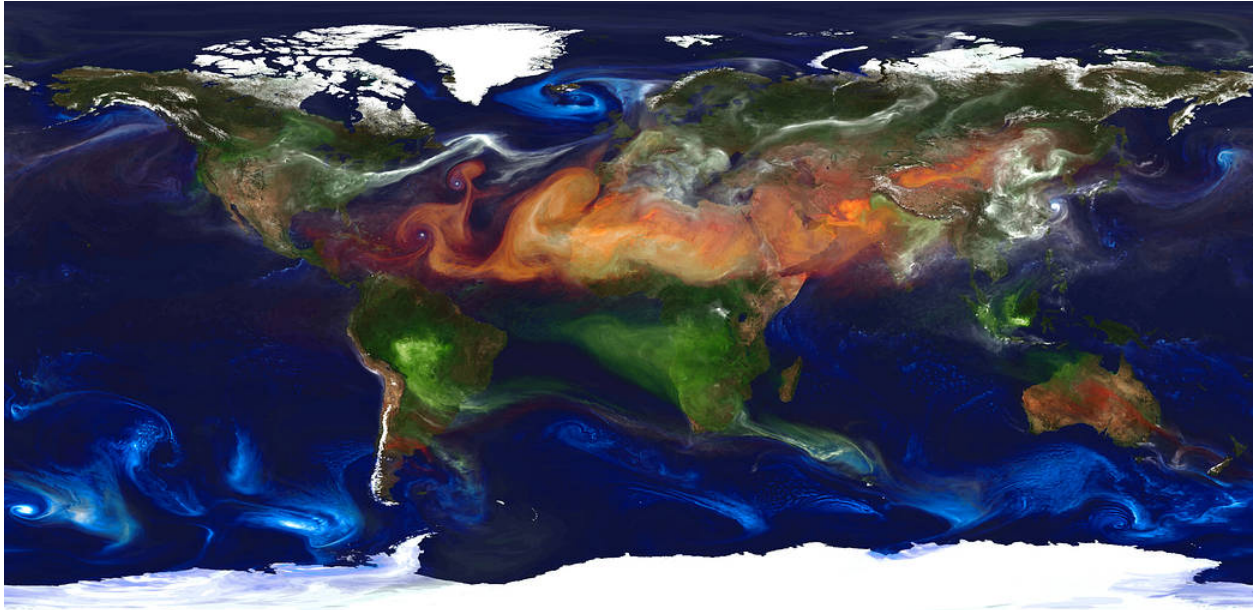


Figure 1.1: A high-resolution global atmospheric modeling run on the Discover supercomputer at the NASA Center for Climate Simulation at Goddard Space Flight Center, Greenbelt, Md., provides a unique tool to study the role of weather in Earth's climate system. The Goddard Earth Observing System Model, Version 5 (GEOS-5) is capable of simulating worldwide weather at resolutions of 10 to 3.5 kilometers (km). This portrait of global aerosols was produced by a GEOS-5 simulation at a 10-kilometer resolution. Dust (red) is lifted from the surface, sea salt (blue) swirls inside cyclones, smoke (green) rises from fires, and sulfate particles (white) stream from volcanoes and fossil fuel emissions. *Public domain image and caption by William Putman, NASA/Goddard.*

1.1.1 Aerosols and Climate: Black and Brown Carbon

Atmospheric aerosols affect Earth's climate directly by scattering and absorbing solar radiation, and these aerosol direct effects represent a large uncertainty in predictions of Earth's future climate. [19] Strongly absorbing aerosols, such as black carbon (i.e. soot), have a net positive effect on radiative forcing, thereby warming the Earth. It is believed that BC has an effect equivalent to roughly 33% that of CO₂, and it is the second-largest climate forcer after CO₂. [19, 20] Conversely, purely scattering aerosols, like ammonium sulfate, reflect sunlight back toward space and contribute a negative (cooling) effect to Earth's radiative budget. [21] In recent years, the loosely categorized, often weakly absorbing aerosols called brown carbon have gained recognition as important contributors to the aerosol direct effects. The net climate effects of these aerosols, which result from incomplete combustion of organic matter and biogenic secondary organic aerosol production, has proven difficult to quantify due to their weakly absorbing nature, and they thus contribute significantly to uncertainties in climate models. [22] For example, Figure 1.2 shows the radiative forcing (ability to warm or cool) due to greenhouse gases (which have a net warming affect), aerosols (which have a net cooling affect), and the total anthropogenic radiative forcing. Note that the width of the distribution, which represents the uncertainty of the estimate, is relatively small for greenhouse gases but quite large for aerosols, and that the width of the total anthropogenic radiative forcing appears to be dominated by aerosol forcing uncertainties.

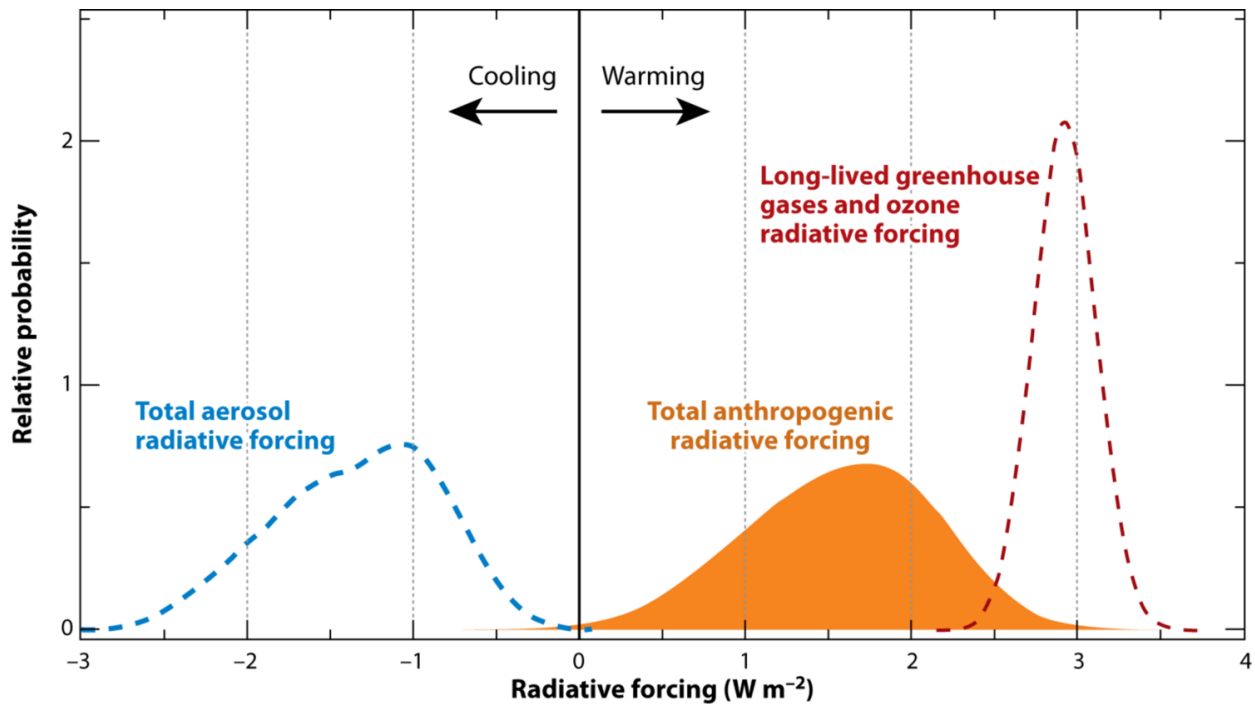


Figure 1.2: Probability distribution functions of combined anthropogenic radiative forcings (RFs) as estimated by the IPCC. The area under the solid orange curve indicates the sum of all anthropogenic RFs; RFs by greenhouse gases and ozone are represented by the dashed red curve, and aerosol direct and indirect RFs are represented by the dashed blue curve. *Figure reprinted from Forster et al. [23], Figure 2.20; caption from Pósfai and Buseck [24].*

1.1.2 Absorbing Aerosols

Often, absorbing aerosols are operationally defined by the shape of their absorption spectrum, which can be represented by the absorption Ångström exponent (AÅE). Generally, aerosol absorption is assumed to follow a power law of the form:

$$b_{abs}(\lambda) = \beta\lambda^{-\hat{a}} \quad (1.1)$$

where b_{abs} is absorption, λ is wavelength, β is a scaling factor, and \hat{a} is the AÅE that describes how quickly aerosol absorption increases toward the UV. Figure 1.3 shows two typical aerosol spectra with varying AÅEs. Some aerosols, such as black carbon (i.e. soot) with an AÅE of 1, have a spectrum that varies weakly with wavelength. [20] Such aerosols typically result from high-temperature combustion by engines and power production, and absorb strongly throughout the UV-visible spectrum. However, other aerosols, such as brown carbon (C_{Br}) scantily absorb visible light, but absorb strongly in the UV, and thus contribute to climate forcing but are difficult to study optically. Because C_{Br} is defined by its absorption spectrum and not its strict composition, it can have many sources, including low temperature combustion (e.g. smoldering biomass), biogenic secondary organic aerosols, and primary biogenic aerosols. [22, 25]

1.2 Goals of This Work

This work was focused on developing instrumentation to measure light scattering and absorption by atmospheric aerosols, primarily C_{Br} and BC. The aim was to measure the balance of scattering and absorption with a suite of instrumentation. Photoacoustic spectroscopy was the technique of choice for absorption because of its low detection limits and insensitivity to scattering. The cavity enhanced spectroscopies, including broadband cavity enhanced spectroscopy and cavity ringdown spectroscopy, were chosen for measuring light extinction

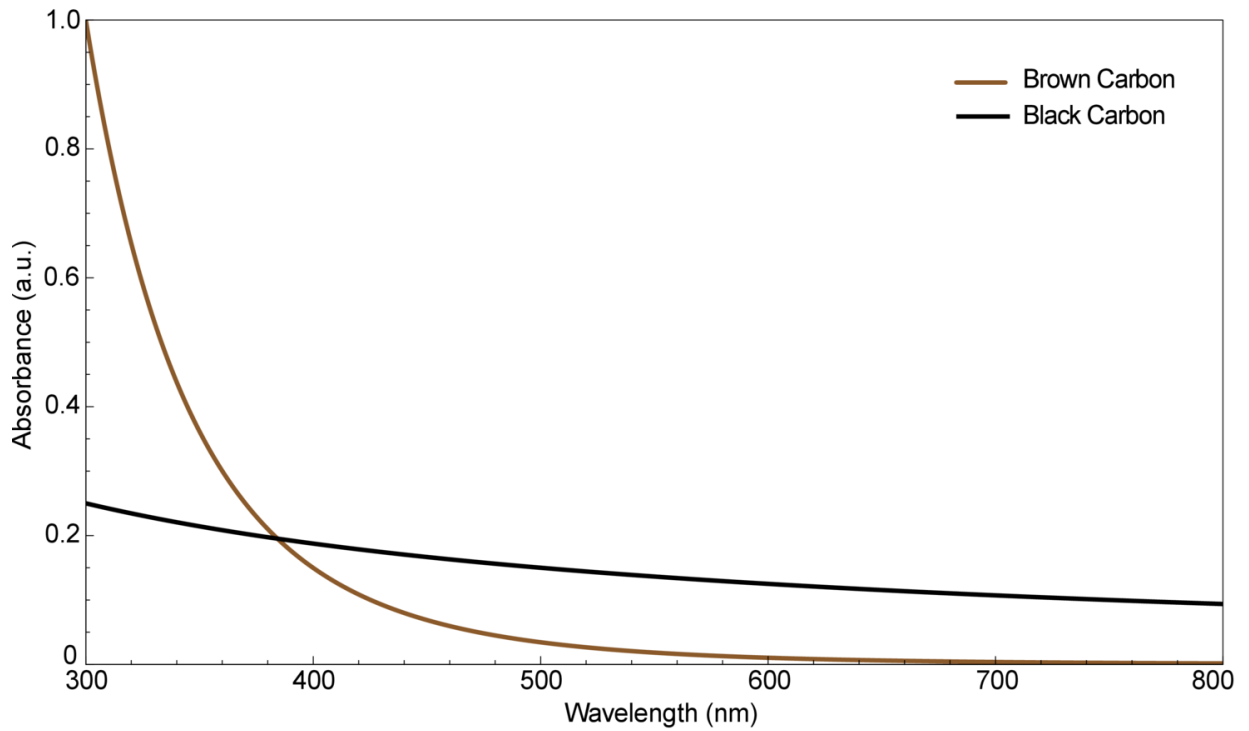


Figure 1.3: Hypothetical C_{Br} and BC absorption spectra. These two species are defined largely by their absorption spectra. Although both spectra are relatively featureless and presumed to follow a power law, C_{Br} exhibits strong absorption in the UV and scant absorption in the visible and NIR. Conversely, BC absorbs relatively strongly throughout the UV-visible-NIR spectrum. This dependence is characterized by the absorption Ångström exponent, $A\AA E$, which is roughly 1 for BC and $\gg 1$ for C_{Br} .

(scattering + absorption). Significant effort was taken to ensure the instruments were compact, robust, and portable so that they could be easily deployed in laboratory and field campaigns as necessary. Indeed, the instruments were deployed in a laboratory campaign at Boston College and in collaborations with other scientists at the University of Georgia. These studies focused on the light-absorbing properties of C_{Br} and BC, and also provided comparisons to commercially available instrumentation.

This work began by exploring the feasibility of using phase-shift cavity ringdown spectroscopy to build a multi-wavelength, lamp-based cavity ringdown spectrometer. Although this was ultimately determined to be unfeasible, the work is presented in chapter 2 for future reference. This chapter also presents the instrument that was ultimately settled upon: a laser-based cavity ringdown spectrometer (CRD). Chapter 3 presents an alternative to this CRD known as broadband cavity enhanced spectroscopy (BBCES). BBCES has the advantage over CRD that it uses a broadband light source (i.e. an LED) and a wavelength-resolved detector to provide a cavity enhanced instrument capable of measuring many wavelengths at once. However, it has the disadvantage of requiring careful, daily measurement of the mirror reflectivity, which hinders its portability.

Chapters 4, 6, and 8 describe photoacoustic spectrometers that were constructed as part of this work. Chapter 4 presents an early version of a multi-wavelength photoacoustic spectrometer that employed a lamp and two lasers to measure aerosol absorption at up to eight distinct wavelengths from 301–662 nm. Although this instrument was used extensively, it was ultimately redesigned and reincarnated as two laser-based, multi-wavelength photoacoustic spectrometers. Chapter 6 describes one of these photoacoustic spectrometers. It is a four-wavelength, laser-based photoacoustic spectrometer operating at 406, 532, 662, and 780 nm. The other of these is described in chapter 8, and is a three-wavelength, laser-based photoacoustic spectrometer operating at 320, 377, and 445 nm.

Chapters 5, 7, and 7 describe various applications of the photoacoustic spectrometers. Chapter 5 describes the results of a laboratory campaign employing the hybrid lamp-laser photoacoustic spectrometer that was focused on measuring soot particles and the effect of non-absorbing coatings on their absorption. This Hybrid PAS provided the first UV-visible absorption spectrum of flame-generated soot during this campaign. This campaign also provided the opportunity to conduct an intercomparison to other academic and commercial instruments. Chapter 7 discusses calibration of multiwavelength, multipass photoacoustic spectrometers. It suggests ozone, a commonly used PAS calibrant, should not be used to calibrate photoacoustic spectrometers due to a dependence of PAS signal on oxygen concentration during ozone measurement. The results from ozone are compared to both nitrogen dioxide and nigrosin aerosols. Chapter 9 presents an intercomparison between three laser-based photoacoustic spectrometers constructed during this work and a commercial filter-based instrument called an aethalometer. It demonstrates significant problems with aethalometer measurements, and presents preliminary correction factors for the instrument.

In addition, several appendices are provided that describe calibration and measurement details for the 4-wavelength PAS (Appendix A), a 3-wavelength photoacoustic spectrometer that was built for Dr. Rawad Saleh (UGA College of Engineering) as part of this work (B), the data format and data processing workflow for the PASs (Appendix C), common troubleshooting techniques for the PASs (Appendix D), and a discussion of the code structure of the PAS LabVIEW program architecture (Appendix F). Other appendices provide code for the instruments' microcontrollers, specifically the code to control the valve and lasers on the PASs (Appendix E) and the code to control the thermoelectric coolers on the BBCES (Appendix G).

References

- (1) Seinfeld, J.; Pandis, S., *Atmospheric Chemistry and Physics: From Air Pollution to Climate Change*; Wiley: 2016.
- (2) Lippmann, M. *Journal of Exposure Analysis and Environmental Epidemiology* **1993**, *3*, 103–129.
- (3) Fuhrer, J.; Skärby, L.; Ashmore, M. *Environmental Pollution*, *97*, 91–106.
- (4) Likens, G. E.; Wright, R. F.; Galloway, J. N.; Butler, T. J. *Scientific American* **1979**, *241*, 43–51.
- (5) Saxena, V. K.; Stogner, R. E.; Hendler, A. H.; Felice, T. P. D.; Yeh, R.-Y.; Lin, N.-H. *Tellus B: Chemical and Physical Meteorology*, *41*, 92–109.
- (6) Kampa, M.; Castanas, E. *Environmental Pollution* **2008**, *151*, 362–367.
- (7) Bin Abas, M. R.; Oros, D. R.; Simoneit, B. *Chemosphere* **2004**, *55*, 1089–1095.
- (8) Fuzzi, S. et al. *Journal of Geophysical Research* **2007**, *112*, DOI: 10.1029/2005jd006741.
- (9) Brocard, D.; Lacaux, J.-P.; Eva, H. *Global Biogeochemical Cycles* **1998**, *12*, 127–139.
- (10) Walsh, J. J.; Steidinger, K. A. *Journal of Geophysical Research: Oceans* **2001**, *106*, 11597–11612.
- (11) Gyan, K.; Henry, W.; Lacaille, S.; Laloo, A.; Lamsee-Ebanks, C.; McKay, S.; Antoine, R. M.; Monteil, M. A. *International Journal of Biometeorology* **2005**, *49*, 371–376.
- (12) Koren, I.; Kaufman, Y. J.; Washington, R.; Todd, M. C.; Rudich, Y.; Martins, J. V.; Rosenfeld, D. *Environmental Research Letters* **2006**, *1*, 014005.
- (13) Longueville, F. D.; Hountondji, Y.-C.; Henry, S.; Ozer, P. *Science of The Total Environment* **2010**, *409*, 1–8.

- (14) Mattingly, K.; Johnson, B.; Fischer, A. *Papers in Applied Geography* **2015**, *1*, 286–293.
- (15) Cong, Z.; Kang, S.; Smirnov, A.; Holben, B. *Atmospheric Research* **2009**, *92*, 42–48.
- (16) Ogren, J.; Charlson, R. *Tellus B* **1983**, *35B*, 241–254.
- (17) Archer, D.; Eby, M.; Brovkin, V.; Ridgwell, A.; Cao, L.; Mikolajewicz, U.; Caldeira, K.; Matsumoto, K.; Munhoven, G.; Montenegro, A.; Tokos, K. *Annual Review of Earth and Planetary Sciences* **2009**, *37*, 117–134.
- (18) Jacobson, M. Z. *Journal of Geophysical Research* **2002**, *107*, DOI: 10.1029/2001jd001376.
- (19) Stocker, T.; Qin, D.; Plattner, G.; Tignor, M.; Allen, S.; Boschung, J.; Nauels, A.; Xia, Y.; Bex, V.; Midgley, P. *The Physical Science Basis* **2013**.
- (20) Bond, T. C. et al. *Journal of Geophysical Research: Atmospheres* **2013**, *118*, 5380–5552.
- (21) Intergovernmental Panel on Climate Change *Climate Change 2013: The Physical Science Basis*; tech. rep.; Intergovernmental Panel on Climate Change, 2013.
- (22) Andreae, M.; Gelencser, A. *Atmos. Chem. Phys.* **2006**, *6*, 3131–3148.
- (23) Forster, P.; Ramaswamy, V.; Artaxo, P.; Berntsen, T.; Betts, R.; Fahey, D. W.; Haywood, J.; Lean, J.; Lowe, D. C.; Myhre, G., et al. In *Climate Change 2007. The Physical Science Basis*, 2007.
- (24) Pósfai, M.; Buseck, P. R. *Annual Review of Earth and Planetary Sciences* **2010**, *38*, 17–43.
- (25) Moosmüller, H.; Chakrabarty, R.; Arnott, W. *Journal of Quantitative Spectroscopy and Radiative Transfer* **2009**, *110*, 844–878.

CHAPTER 2

CAVITY RINGDOWN AND PHASE-SHIFT CAVITY RINGDOWN SPECTROSCOPY

2.1 Introduction

The cavity enhanced spectroscopies are a family of techniques used to measure extinction (scattering + absorption) that employ high-finesse optical cavities to achieve exquisitely low detection limits. The most well-known of these methods is probably cavity ringdown spectroscopy (CRDS), but other variants exist as well. These include phase-shift cavity ringdown spectroscopy (PS-CRDS), broadband cavity enhanced spectroscopy (BBCES, discussed in chapter 3), evanescent-wave CRDS, and noise-immune cavity enhanced optical heterodyne molecular spectroscopy (NICE-OHMS). [1] These techniques have a wide range of applications in numerous fields, having been used, for example, to detect atmospheric trace gases [2, 3] to obtain high resolution spectra of gas-phase molecules, [4, 5] and even to create optical frequency standards. [6] This chapter will discuss the development of CRDS and PS-CRDS with the ultimate goal of measuring extinction by aerosols. The construction, gas-phase validation of the instruments, and difficulties therein, will be presented.

2.1.1 Cavity Ringdown Spectroscopy

Cavity ringdown spectroscopy was first developed in the 1980s to accurately measure the reflectivity of very highly reflective mirrors, and has seen a growth in applications since then. [7] It has been well described in numerous reviews and several books. [1, 8–11] The

basic technique is to couple light into a high-finesse optical cavity constructed of two highly reflective mirrors ($R > 99.99\%$). Light that couples into the main cavity mode will undergo constructive interference and a build-up of intensity will occur; when the light is quickly switched off, its intensity (I) will decay exponentially over time (t), with a specific time constant, τ .

$$I(t) = I_0 \exp\left(\frac{-t}{\tau}\right) \quad (2.1)$$

More specifically, τ depends on the mirror reflectivity (R), the cavity length (l), the absorption and/or scattering (extinction) due to species inside the cavity (b_{ext}), and the speed of light (c).

$$\tau = \frac{1}{c(1 - R + b_{ext}l)} \quad (2.2)$$

Importantly, equation 2.2 assumes the refractive index of the medium in the cavity is 1 and any additional optical losses other than those due to R and b_{ext} are negligible. Then, if the empty-cavity ringdown time (τ_0) is known, extinction (i.e. b_{ext}) can be solved for directly, conveniently with no calibration of the CRDS.

$$b_{ext} = \frac{1}{c} \left(\frac{1}{\tau} - \frac{1}{\tau_0} \right) \quad (2.3)$$

The primary advantage of CRDS is that it provides an effective path length on the order of kilometers for a typical CRD cell, and allows easily achievable detection limits of $1 \times 10^{-8} \text{ cm}^{-1}$ ($< 1 \text{ Mm}^{-1}$) and demonstrated detection limits as low as $4.4 \times 10^{-12} \text{ cm}^{-1}$. [12] However, other advantages include its calibration-free nature (assuming τ_0 is known) and its insensitivity to intensity fluctuations of the light source. A disadvantage of CRDS is that it is necessary to use a light source with a fall time $\ll \tau$. For typical values of $R = 99.995\%$ and $l = 1 \text{ m}$, $\tau_0 = 66 \text{ } \mu\text{s}$, thereby generally necessitating the use of lasers, whether pulsed or

continuous wave (CW) diode lasers diode lasers with a fast fall time. This severely limits the wavelength coverage of CRDS and can also add to the price of the instrument.

2.1.2 Phase-shift Cavity Ringdown Spectroscopy

Phase-shift cavity ringdown spectroscopy is a variant of CRDS that allows for the use of much slower, and often cheaper, light sources. In PS-CRDS, a sinusoidally modulated CW light source (e.g. an LED, lamp, or diode laser) is coupled into the cavity. The cavity is analogous to a capacitor in an electronic circuit in that it introduces a phase shift (ϕ) into the sine wave that is related to the time constant of the cavity via the angular modulation frequency (ω).

$$\tan(\phi) = -\omega\tau \quad (2.4)$$

Using this to calculate extinction, equation 2.3 then becomes:

$$b_{ext} = \frac{w}{c} \left(\frac{1}{\tan(\phi)} - \frac{1}{\tan(\phi_0)} \right) \quad (2.5)$$

Therefore, the phase difference between light exiting the extinction-free cavity (ϕ_0) and the wave exiting the sample-laden cavity (ϕ) can be measured to determine the extinction in the cavity. In practice, it is also necessary to measure the zero-phase offset, which is primarily introduced by the electronics and is often measured by removing the mirrors from the cavity. Like CRD, this allows for a calibration-free measurement and is insensitive to intensity fluctuations. Further, it has the added advantage of allowing CW light sources and much slower detector to be used.

2.2 Materials and Methods

Initially, the goal of this work was to develop an incoherent PS-CRDS using a Hg-Xe arc lamp. A motorized filter wheel would have eventually controlled the measurement wavelength while various sets of CRD mirrors would have been used to match the wavelength selected. After development on this project, it was determined that problems measuring the zero-phase offset (i.e. the phase with no cavity present, not to be confused with the extinction-free phase, ϕ_0) caused significant accuracy errors with this setup and other forms of CES, including CRDS, were pursued instead.

2.2.1 Phase-shift cavity ringdown spectrometer

Figure 2.1 shows a generalized block diagram of the PS-CRDS. In the initial arrangement, the PS-CRDS was illuminated with a 100W Hg-Xe arc lamp (Optical Building Blocks). The output from the lamp's internal parabolic reflector was focused with a $f/2$ aspheric lens (Edmunds Optics) through an optical chopper (Thorlabs) to modulate the light at the desired frequency. The modulated light was captured with a second, identical lens to collimate the beam and send it through a bandpass filter (Semrock, Inc.) and heat absorbing glass (Thorlabs), both housed in a motorized filter wheel. The filtered beam was turned with two mirrors into a second set of lenses used to re-collimate the slightly divergent beam. The re-collimated beam was coupled in the PS-CRDS cell by aligning the beam on the central axis of the PS-CRDS cell.

The PS-CRDS cell consisted of a custom made 2-3/4 inch conflat (CF) nipple that was 0.5 m in length (Kurt J. Lesker Company) with two 3/4 inch tubes welded on at 45° to the main channel (welding performed by the UGA Instrument Shop). Commercial, purgeable, CRD mirror mounts were mated to the CF flanges on either end of the nipple (CRD-optics, Inc.), each of which held a 6 m radius of curvature, 2 cm diameter commercial CRD mirror

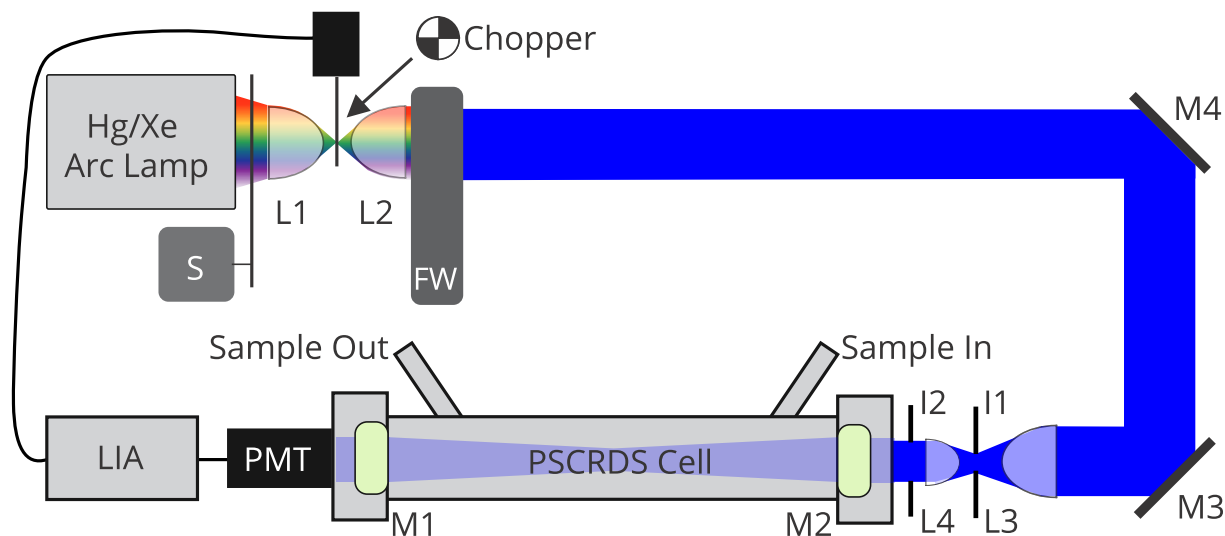


Figure 2.1: Block diagram of the phase shift cavity ringdown used in this work. The cavity was 0.5 m in length; the diagram is not to scale. L = lens, FW = filter wheel, S = shutter, M = mirror, I = iris, PMT = photomultiplier tube, LIA = lock-in amplifier; M1 + M2 are low-loss CRD mirrors.

(CRD-optics, Inc.) that was continually purged with dry nitrogen. A PMT collected light exiting the rear of the cavity (Hamamatsu Photonics, K.K.). The PMT signal was digitized using a lock-in amplifier (Stanford Research Systems SR830), the phase of which was zeroed to the chopper phase. All of the data shown herein were obtained with mirrors centered at 440 nm or 540 nm; further specifications for the mirrors are available in Table 3.1.

An alternate iteration of this instrument replaced the lamp, chopper, and filter wheel with an electronically modulated diode laser operating at 406 nm (Coherent OBIS). The setup remained the same, although the lenses became irrelevant and were removed and a 405 nm laser line filter (Thorlabs) was placed on the PMT to block stray light.

2.2.2 Cavity Ringdown Spectroscopy

Figure 2.2 shows a CAD model and block diagram of the CRD instrument developed in this work. The CRD instrument was constructed using a commercially available 30-mm cage mounting system (Thorlabs) for stability and to interface it with other instruments. The CRD consists of a diode laser (Coherent OBIS), two turning mirrors (M3 and M4), a 12.5 mm diameter stainless steel CRD cell (UGA Instrument Shop), and an avalanche photodiode (Thorlabs). A Faraday isolator (Thorlabs) protects the laser from back reflections. Because very little power is needed for CRD, a 90:10 beamsplitter (Thorlabs) is placed in the laser beam to send 90% of it to a photoacoustic spectrometer (see chapter 6). More details of the CRD system and information about the data acquisition process for the CRD can be found in section 6.1. The data presented here are for a 662 nm CRD, which used 0.5 m radius of curvature, 25.4 mm diameter mirrors (FiveNine Optics) with $R = 99.9985\%$ at 662 nm. Alternate versions were created, including a 440 nm diode-laser version and 532 nm Nd:YAG version; a pre-existing 355 nm Nd:YAG version was also used at times.

2.2.3 Gas-phase Validations

Both ozone and nitrogen dioxide were used to validate the CES instruments. For ozone measurements, silica gel was baked at $>100^\circ\text{C}$ for approximately 1 hour while under vacuum to remove contaminants. After baking and pumping, the silica gel trap was submerged in a dewar containing a slurry of solid CO_2 and isopropanol to cool the trap to approximately -70°C . A commercial corona-discharge ozone generator (Pacific Ozone Technologies) was connected to the trap and used to generate ozone with ultra high purity oxygen ($> 99.999\%$, Airgas). This ozone was trapped for approximately 20 minutes. After trapping, a deep violet color can be observed on the silica gel, which is ozone itself and indicates successful trapping. The trap was then moved to the instrumental setup and a carrier gas of nitrogen was used

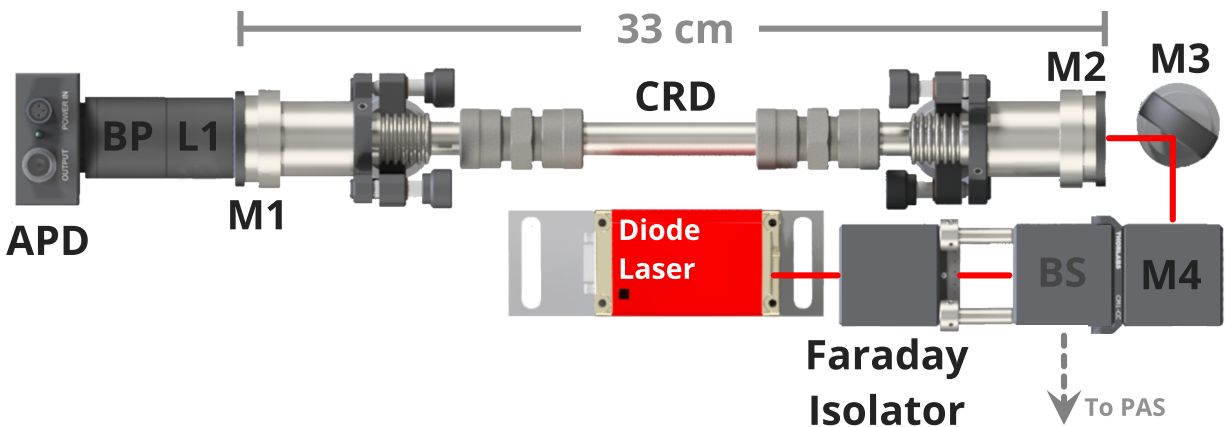


Figure 2.2: Model of the cavity ringdown spectrometer developed in this work. The cavity is 0.3 m in length; all portions of the model are drawn to the scale suggested by the 33 cm scale bar. L = lens, BS = 90:10 beamsplitter, M = mirror, APD = avalanche photodiode, BP = bandpass filter; M1 + M2 are low-loss CRD mirrors.

to remove ozone from the trap and carry it to the instrument in various dilutions. A 10 cm pathlength Beer's law absorption cell, consisting of a Hg pen lamp, a photodiode with a 254 nm bandpass filter, and a voltage readout, was used to measure the ozone concentration for comparison to literature cross sections.[13]

A standard mixture of nitrogen dioxide was also used to validate the CES instruments. A mixture of 10.29 ppm ($\pm 5\%$) NO_2 in N_2 (with trace O_2 for stability) was purchased from Airgas, Inc. The mixture was then diluted with nitrogen boil off from the headspace of a liquid nitrogen tank (Airgas, Inc.). The flow rate of NO_2 was controlled by a rotameter (Omega Engineering, 250 SCCM full scale, accuracy = $\pm 5\%$ full scale) and the N_2 flow rate was controlled by a needle valve and measured with a commercial flow meter (TSI, Inc., accuracy = 2%).

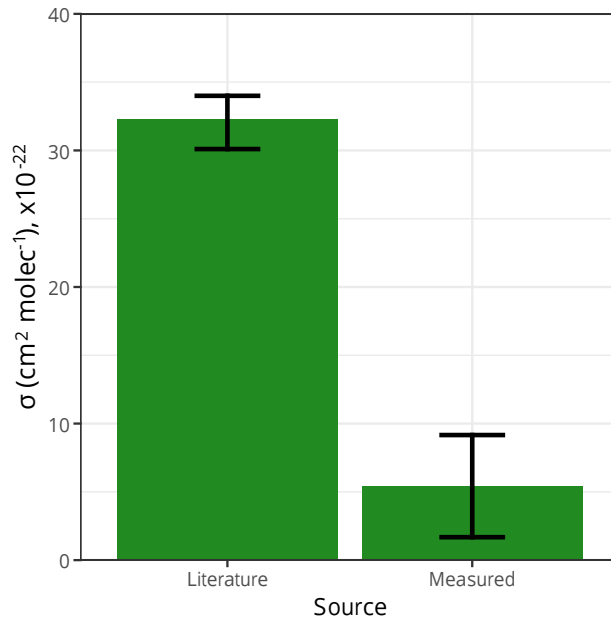


Figure 2.3: Ozone cross section measured with the PS-CRDS at 546 nm. The bar for the measured values is the average of two replicates, while the value for the literature values is the mean of the literature spectrum taken over the FWHM range of the PS-CRDS’s bandpass filter; the error bars indicates the range for each data set. Literature values taken from Voigt et al. [13]

2.3 Results and Discussion

Although signal was obtained with the lamp-based PS-CRDS, there were numerous difficulties introduced by using the lamp. Primarily, the divergent nature of the light source made it very difficult to couple into the cavity, and significant amounts of light were lost in the process of focusing and collimating the beam, presumably hurting the signal-to-noise ratio. Further, the incoherent nature of the beam probably excited multiple cavity modes and led to multi-exponential decays. After several months of woefully inaccurate data (Figure 2.3), a decision was made to replace the lamp with a 406 nm diode laser.

Unfortunately, the diode laser did little to help the accuracy of the PS-CRDS. Figure 2.4 shows typical measurements by the PS-CRDS, specifically of absorption by NO_2 . Identical

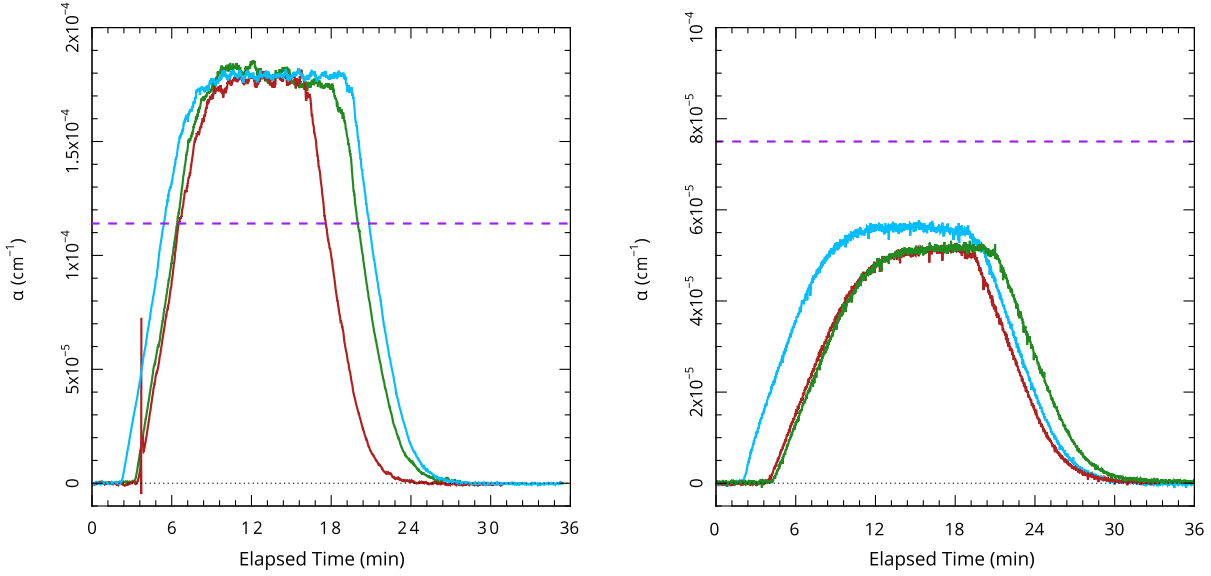


Figure 2.4: Absorption of NO_2 measured by PS-CRDS over three replicates on two sequential days. The instrument was stable on any given day, but not accurate, as evidenced by comparing to the known absorption represented by the dashed purple lines. On Day 1 (left panel), the PS-CRDS measured roughly 50% higher than expected but the very next day it measured 30% lower than expected (right panel). The dotted black lines represents 0 absorption.

concentrations of NO_2 were measured over three consecutive runs per day using the instrument. Although it consistently reported the same value for the absorption on any given day, it was inconsistent from day-to-day and the accuracy was significantly off in general. For example, the measured value was lower than expected by 50% on Day 1 (left panel) and high by 30% the very next day (right panel). Ultimately, this was attributed to errors in measuring the zero phase offset, and future studies moved toward CRDS and broadband cavity enhanced spectroscopy.

The results obtained with CRDS were much improved compared to PS-CRDS. Figure 2.5 shows the absorption cross section of NO_2 measured with the CRDS. When plotted with the measured absorption on the y-axis and the number density of NO_2 , N_{NO_2} , on the x-axis, the

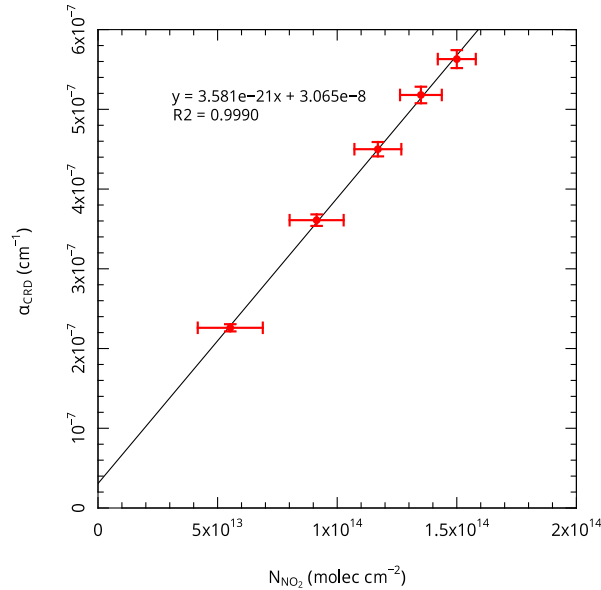


Figure 2.5: Retrieval of the NO_2 absorption cross section at 662 nm via CRDS. The value of $3.581 \times 10^{-21} \text{ cm}^2 \text{ molec}^{-1}$ is within 1% of the literature value of $3.61 \times 10^{-21} \text{ cm}^2 \text{ molec}^{-1}$ from Burrows et al. [14]

slope of the line of best fit represents the absorption cross section at 662 nm averaged over all values of N , according to $b_{ext} = N\sigma$. The value of $3.581 \times 10^{-21} \text{ cm}^2 \text{ molec}^{-1}$ is within 1% of the literature value of $3.61 \text{ cm}^2 \text{ molec}^{-1}$ from Burrows et al. [14] The non-zero offset can be attributed to systematic errors introduced by the rotameter used to control the NO_2 flow rate, and is within the accuracy of the rotameter.

2.4 Conclusion

Two types of cavity enhanced spectrometers were discussed here: (1) a phase-shift cavity ringdown spectrometer and (2) a cavity ringdown spectrometer. After this project, several conclusions were drawn:

- Although PS-CRDS has been proven elsewhere, difficulties in measuring the zero offset phase and the relative bulk of the necessary equipment make PS-CRDS impractical for the purposes of this project.
- CRDS provides a much more robust and compact instrument that can be used for many portions of this project.
- CRDS and PS-CRDS both lack wavelength coverage. As a result, the next portion of this project was concerned with developing a wavelength-resolved cavity enhanced instrument: a broadband cavity enhanced spectrometer.

References

- (1) Vallance, C. *New Journal of Chemistry* **2005**, *29*, 867.
- (2) Fuchs, H.; Dube, W. P.; Lerner, B. M.; Wagner, N. L.; Williams, E. J.; Brown, S. S. *Environmental Science & Technology* **2009**, *43*, 7831–7836.
- (3) Crosson, E. *Applied Physics B* **2008**, *92*, 403–408.
- (4) Newman, S. M.; Lane, I. C.; Orr-Ewing, A. J.; Newnham, D. A.; Ballard, J. *The Journal of Chemical Physics* **1999**, *110*, 10749–10757.
- (5) Hodges, J. T.; Layer, H. P.; Miller, W. W.; Scace, G. E. *Review of Scientific Instruments* **2004**, *75*, 849–863.
- (6) Dinesan, H.; Fasci, E.; d’Addio, A.; Castrillo, A.; Gianfrani, L. *Optics Express* **2015**, *23*, 1757–1766.
- (7) Anderson, D. Z. Reflectometer based on optical cavity decay time., US Patent 4,571,085, Feb. 1986.
- (8) Brown, S. S. *Chemical Reviews* **2003**, *103*, 5219–5238.
- (9) Busch, K.; Busch, M., *Cavity-ringdown Spectroscopy: An Ultratrace-absorption Measurement Technique*; ACS symposium series v. 720; American Chemical Society: 1999.
- (10) Berden, G.; Engeln, R., *Cavity Ring-Down Spectroscopy: Techniques and Applications*; Wiley: 2009.
- (11) *Cavity-Enhanced Spectroscopy and Sensing*; Gagliardi, G., Looock, H.-P., Eds.; Springer Berlin Heidelberg: 2014.
- (12) Huang, H.; Lehmann, K. K. *Applied Optics* **Mar. 2010**, *49*, 1378.
- (13) Voigt, S.; Orphal, J.; Bogumil, K.; Burrows, J. *Journal of Photochemistry and Photobiology A: Chemistry* **2001**, *143*, 1–9.

- (14) Burrows, J.; Dehn, A.; Deters, B.; Himmelmann, S.; Richter, A.; Voigt, S.; Orphal, J.
Journal of Quantitative Spectroscopy and Radiative Transfer **1998**, *60*, 1025–1031.

CHAPTER 3

A FOUR-CHANNEL, UV-VISIBLE BROADBAND CAVITY ENHANCED SPECTROMETER FOR AMBIENT AEROSOL EXTINCTION

3.1 Introduction

Determining the net heating or cooling effects of aerosols on climate, requires accurate measurements of light scattering and absorption by aerosols, termed extinction when summed. Although aerosol extinction is well known to have an exponential wavelength dependence with the greatest extinction toward the UV, the spectral shape varies based on the specific physio-chemical properties of individual aerosols. Typical methods of determining aerosol extinction involve measuring scattering and/or absorption separately, and include the *in-situ* methods of nephelometry, photoacoustic spectroscopy (PAS), and albedometry, and filter-based methods like particle-soot absorption photometry (PSAP), aethalometry, and multiangle absorption photometry (MAAP) [1, 2]. Many of these instruments are available commercially, but are limited to several discrete wavelengths in the UV-visible spectrum. Typically, two or more of these methods are combined to deduce total extinction and calculate the ratio of scattered light to total extinction (i.e. the single scattering albedo, SSA) for climate models. However, due to the potential artifacts induced by filter-based instruments and the limited wavelength availability of all these instruments—notably at UV wavelengths—we posit these methods may not provide true atmospheric SSAs.

Recently, broadband cavity enhanced spectroscopy has gained popularity as a method for measuring total extinction. BBCES has been applied to measurements of trace gas absorption, Rayleigh scattering, and extinction in laboratory aerosols. [3–8] Although others have proposed the idea of measuring ambient aerosol absorption by comparing BBCES and nephelometer measurements, ambient aerosol measurements by BBCES have been sparse to date and have made no attempt to separate aerosol absorption and scattering. [9]

BBCES has been described and reviewed elsewhere, but will be discussed briefly here [10, 11]. Having arisen from cavity ringdown spectroscopy, BBCES uses an optical cavity/sample cell bound on either end by highly reflective mirrors ($R \approx 99.99\%$). In BBCES, light—often from an incoherent, broadband source like an LED—is coupled into the cavity. Intensity builds up inside the optical cavity, and is readily possible to achieve effective path length on the order of kilometers. The integrated intensity of light transmitted through the back mirror is detected with a suitable detector, such as a spectrophotometer. The combination of a broadband light source and wavelength-resolved detector provides the opportunity to simultaneously collect cavity enhanced data over a range of wavelengths, although in practice the bandwidth is limited by the reflective region of the cavity mirrors. As a result, most measurements have to date been limited to several up to tens of nanometers in single regions of the UV-visible spectrum. [6, 7]

Here, we present an improved instrument based on four separate optical cavities arranged in parallel. This novel configuration provides four spectral windows between 360 and 690 nm, which we argue is enough to allow accurate fitting of the smooth, mostly featureless aerosol extinction spectrum and interpolate an entire UV-visible spectrum. Further, three of these windows directly overlap with the acquisition wavelengths for several common commercial instruments. We first validate the instrument by measuring absorption in a calibrated gas mixture of NO_2 , and then use the instrument to measure ambient aerosol extinction and compare the data to those from a commercial nephelometer and a UV (355 nm) cavity

ringdown spectrometer (CRDS). We further show the ability to estimate absorption due to ambient aerosols by comparing nephelometer and BBCES data.

3.2 Experimental

3.2.1 Instrument Description

We have developed a four-channel incoherent broadband cavity enhanced spectrometer, in which incoherent, broadband light from four LEDs is coupled into four separate optical cavities. A diagram of the instrument is shown in Figure 3.1, and detailed specifications are provided in Table 3.1. Each cavity consists of a custom-made stainless steel tube 50 cm long and 38 cm in diameter with 1.75 cm diameter sample inlets/outlets welded at 45 degrees to the main channel. The tube is bound on either end by a 2 cm diameter, 6 m radius of curvature cavity ringdown mirror (CRD Optics, Inc.) held in a purgeable precision mirror mount (CRD Optics, Inc.).

The light source for each cell is a separate high-power light emitting diode (LED) that is matched to the mirror reflectivity and mounted on an aluminum heatsink. The LEDs are powered by a single constant current power supply (Leaptronix LPP-3025T) at the manufacturers' recommended maximum operating current for each LED. The light is focused into the cavity with a 25.4 mm $f/1$ plano-convex lens (Thorlabs, Inc.). Light exiting the cavity is bandpass filtered and collected with a 25 mm $f/1.25$ aspheric condenser lens (Thorlabs, Inc.) into a custom-made fiber optic cable (Gulf Photonics, Inc.) with four separate 200 μm , 0.22 numerical aperture cores combined into a single SMA connector on one end.

A benchtop spectrophotometer (Ocean Optics QE65000) is connected to the common end of the fiber optic as a detector. Data were acquired from the spectrophotometer using the SpectraSuite software package supplied with the instrument. The wavelength axis of the spectrophotometer was calibrated according to the SpectraSuite user manual using

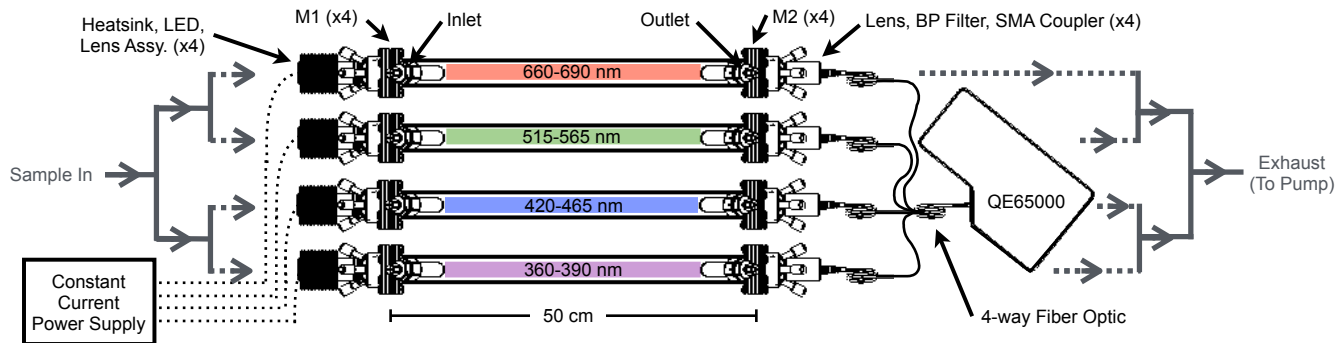


Figure 3.1: Diagram of the BBCES. Four BBCES channels are combined in parallel with a quad-furcated fiber optic cable into a benchtop spectrophotometer. Grey arrows represent the sample flow; dashed arrows connect to the inlets and outlets but are broken here for clarity. A separate flow of filtered N_2 is directed over each mirror to maintain cleanliness (not shown). BBCES components drawn to scale.

emission lines from a Hg pen lamp (UVP, LLC) and, for the red channel, the $b^1\Sigma_g^+(\nu' = 1) - X^3\Sigma_g^-(\nu'' = 0)$ transition of O_2 at 690 nm. Because the calibration is heavily weighted toward shorter wavelengths, an offset of 0.5–1.5 nm is typically observed in the red channel; therefore, spectral features are manually aligned during NO_2 measurement for the red channel. All BBCES data were acquired with a 2 second detector integration time and 16 averages to yield a sampling time of 32 seconds; a boxcar filter with a width of 5 nm was applied to spectra when measuring mirror reflectivity and ambient aerosol extinction.

3.2.2 BBCES Data Analysis

During an extinction measurement, the intensity transmitted through a blank gas, typically N_2 or HEPA filtered air, is measured and termed I_0 . This is then compared to the intensity

Table 3.1: BBCES Optical Components

Cell	λ_{center}^* (nm)	R^* (%)	Filter	LED	LED Output* (mW)	Eff. Range (nm)
UV	365	99.97	FF01-377/50-25 [†] FF01-424/SP-25 [†]	LZ1-10UV00-0000*	1000	360–390
Blue	440	99.995	FF01-442/46-25 [†]	H2A1-435**	380	420–460
Green	540	99.9985	FF01-540/50-25 [†]	LZ1-10G100*	200 lm	515–565
Red	690	99.995	FGL-665 [‡]	H2A1-690**	60	660–725 (690) [◊]

* Manufacturer’s specifications

[†] Semrock, Inc.; [‡] Thorlabs, Inc.

* LED Engin, Inc.; ** Roithner Lasertechnik, GmbH

◊ Limited to 690 nm by water vapor interference.

measured after filling the cavity with a sample (I). Assuming the mirror reflectivity is accurately known, the wavelength-resolved extinction (b_{ext}) can be determined thusly:

$$b_{ext}(\lambda) = \left(\frac{1 - R(\lambda)}{d} \right) \left(\frac{I_0(\lambda) - I(\lambda)}{I(\lambda)} \right) \quad (3.1)$$

Here, d is the distance between the cavity mirrors and R is the mirror reflectivity. R is determined by measuring a known extinction, such as a Rayleigh scattering in gases [6, 7]. In determining R , we first fill the cavities with He (ultra high purity grade, Airgas, Inc.), which has a Rayleigh scattering cross section below our detection limit, to obtain I_0 . CO₂ (instrument grade, Airgas, Inc.) is used to obtain I . A fit to the Rayleigh scattering cross sections presented by Snee and Ubachs for CO₂ and the fit to Shardanand and Rao provided by Washenfelder et al. for He are used to solve for R in Equation 3.1 [6, 12, 13].

$$\sigma_{He} = 1.336 \times 10^{-17} \lambda^{-4.1287} \quad (3.2)$$

$$\sigma_{CO_2} = 2.389 \times 10^{-15} \lambda^{-4.1343} \quad (3.3)$$

To maintain mirror cleanliness, a purge flow of N₂ is directed over each cavity mirror at 25 sccm (standard cubic centimeters per minute) during all measurements except Rayleigh scattering. This necessitates adjusting the final extinction by the factor R_L , defined as the ratio of the total cell length, d , to the occupied sample length:

$$b_{ext}(\lambda) = R_L \left(\frac{1 - R(\lambda)}{d} + b_{ext}m(\lambda) \right) \left(\frac{I_0(\lambda) - I(\lambda)}{I(\lambda)} \right) \quad (3.4)$$

Note that $b_{ext,m}$ is also added to account for Rayleigh scattering by the matrix gas, here assumed to be b_{ext,N_2} for NO₂ measurements and $b_{ext,air}$ for ambient measurements[6, 14].

Figure 3.2 shows typical raw transmission spectra and reflectivity curves for the instrument. The peak mirror reflectivities are significantly lower than those quoted by the manufacturer (see Table 3.1). This results from the excitation of higher-order cavity modes by the passively coupled LEDs, which lowers the effective reflectivity. Thus, the reflectivity curves presented in Figure 3.2 represent the weighted average reflectivity for all excited modes, as has been previously noted by others. [10] Further, despite the manufacturer’s specified center wavelength of 690 nm for the red mirrors, we discard data above 690 nm during measurements to avoid interference from water vapor. Although weak, absorption bands due to water vapor are present from ≈ 690 –750 nm, and when residual water vapor adsorbs on the cavity mirrors these weak overtones cause a large and erratic decrease in mirror reflectivity.

3.2.3 Validation with NO₂

The instrument’s functionality and linearity were verified by measuring absorption in dilutions of a standard NO₂ mixture (Airgas, Inc.). A 10.29 ppm ($\pm 5\%$) mixture of NO₂ in N₂ was diluted with a separate flow of N₂ to various concentrations. The diluted gas stream was delivered to the instrument in PTFE tubing at a flow of approximately 2000 sccm and split in parallel to each of the four cavities. I_0 was obtained using N₂ as the blank gas.

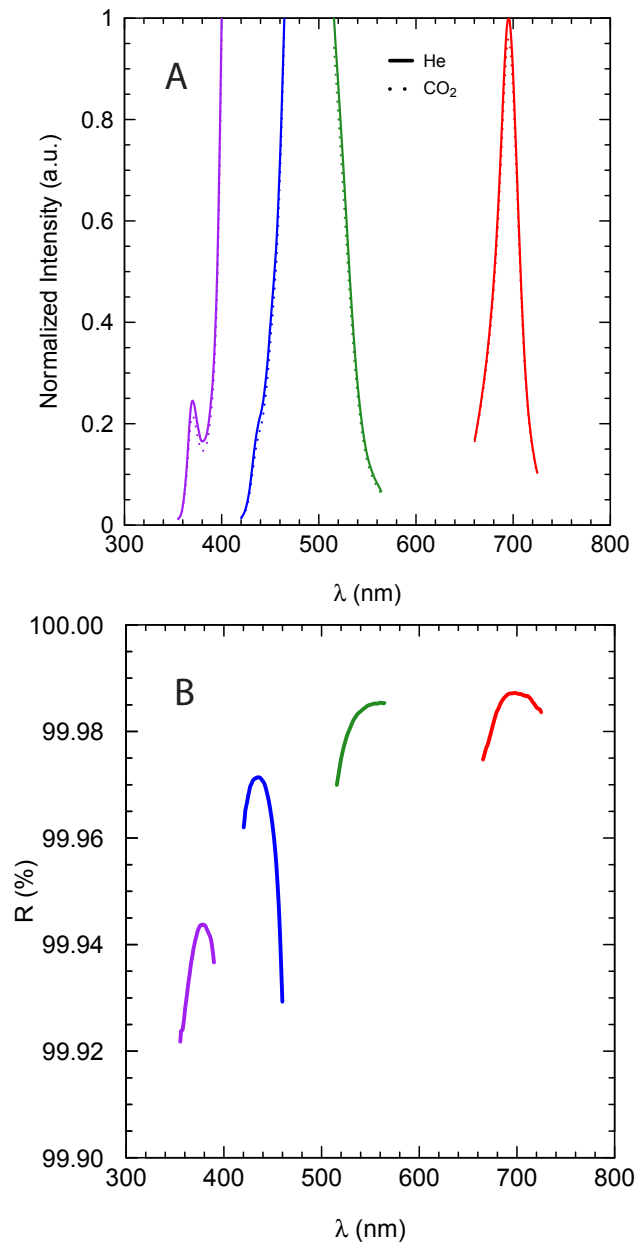


Figure 3.2: Typical raw intensity spectra (normalized to 1) for He and CO₂ (A) and the resulting reflectivity curves (B).

3.2.4 Cavity Ringdown Spectroscopy

Cavity ringdown spectroscopy was used as an equivalent measurement of total extinction to independently validate ambient BBCES measurements. The CRDS instrument described by Toole and co-workers was used [15]. Measurements were made using pulsed 355 nm light from a Nd:YAG laser operating at 10 Hz. The light is spatially filtered before entering the cavity to match the TEM₀₀ cavity mode. A photomultiplier tube (PMT) detects the ringdown events, which are digitized with a digital oscilloscope and recorded with a custom computer program. A total of 320 ringdown decays were averaged for each measurement of τ and τ_0 to provide a sampling time of 32 seconds. A purge flow of 40 sccm was maintained over each mirror.

3.2.5 Nephelometry

During ambient measurements, a TSI 3563 three wavelength integrating nephelometer was used to obtain measurements of aerosol scattering cross sections. The nephelometer uses a halogen lamp and three 40 nm bandpass filters to measure scattering at 450, 550, and 700 nm. Prior to measurements, the nephelometer was calibrated according to the manufacturer's protocol using CO₂ and air. Aerosols were delivered to the instrument in conductive silicone tubing at a rate of 9 liters per minute. The averaging time was set to 60 seconds, and a zero background of HEPA filtered air was taken automatically by the instrument every 1000 seconds.

3.2.6 Ambient Measurements

Ambient aerosols were collected at the University of Georgia in Athens, GA (33.95°N, 83.37°W) during September and October 2014 under a variety of weather and particulate matter conditions. Aerosols were drawn through conductive silicone tubing into a Nafion

dryer (Perma Pure, LLC) where they were dehumidified to a dew point of approximately 0°C (\approx 25% RH) with a sheath flow of N₂ before being delivered to the instruments. For BBCES and CRDS measurements, samples were drawn through the instrument at a total flow of 1500 sccm. Measurements of I_0 and τ_0 were performed by placing a HEPA filter (TSI, Inc.) after the dryer, and were taken between each measurement of I or τ for average spectra, or each hour during time series data.

3.3 Results and Discussion

3.3.1 Validation with NO₂

Figure 3.3 shows the results of the NO₂ measurements that tested the instrument’s ability to measure extinction and respond linearly over a range of concentrations. Figure 3.3A compares the spectrum measured by BBCES to the literature spectra. The higher resolution literature spectra of Vandaele [16] and Bogumil et al. [17] were convoluted to the resolution of the BBCES using a Gaussian filter. The blue, green, and red cells exhibit average percent errors of 9, 3, and 8 %, respectively, compared to the work by Vandaele [16] (who measured wavelengths $>$ 384 nm), while the UV cell is within 1 % of the spectra of Bogumil et al. [17]. Likewise, measurements by the blue and green cells fall within 10% of the spectra by Bogumil et al. [17], although the measurements in the red are about 15% low compared to this source. However, we note that agreement between literature spectra deteriorates in the red region of the spectrum. Aside from this, the differences in percent error between cells are compounded error attributable to uncertainties in the purge flow volume, slight differences in R_i between cells, and variability in reflectivity measurements. Within this error, we conclude proper response of the BBCES to NO₂ absorption, and further note the instrument’s ability to accurately measure absorption over at least 3 orders of magnitude.

Table 3.2: Results of Linear Regression with NO₂

Cell	σ_{lit}^* $\times 10^{-20}$	σ_{lit}^\dagger $\times 10^{-20}$	σ_{meas} $\times 10^{-20}$	R^2
UV (365 nm)	59.7	–	55.1	0.9980
Blue (440 nm)	51.2	47.3	51.9	0.9972
Green (540 nm)	10.2	9.41	8.71	0.9987
Red (675 nm)	1.05	0.976	0.933	0.9982

All cross sections are in units of cm²molec⁻¹.

*Bogumil et al. (2003) [17]

†Vandaele et al. (2002) [16]

To quantitatively validate the instrument’s performance, NO₂ absorption was measured at several concentrations. The absorption cross section, σ , was then determined according to $b_{ext}(\lambda) = N\sigma(\lambda)$, where N is the number density of NO₂. The measured extinction was plotted against concentration for each channel (at 365, 440, 540, and 675 nm). A linear regression, shown in Figure 3.3B, was performed to determine an average absorption cross section for each wavelength. All BBCES channels respond linearly to NO₂ concentration throughout the tested range of 0.5 to 5.2 ppm, with correlation coefficients > 0.997 for each cell. Individual correlation coefficients are shown in Table 3.2 along with the calculated absorption cross sections for the center wavelength of each cavity. The average cross sections measured with the BBCES instrument agree within 10% of the literature values. This error is comparable to the agreement between the two literature sources ($\approx 8\%$).

3.3.2 Instrument Stability

Allan deviation provides a measure of an instrument’s stability and ultimate detection limit, and has been widely used in characterizing cavity enhanced instruments [18–20]. It was performed here by monitoring the intensity changes overnight in cavities filled with N₂. The

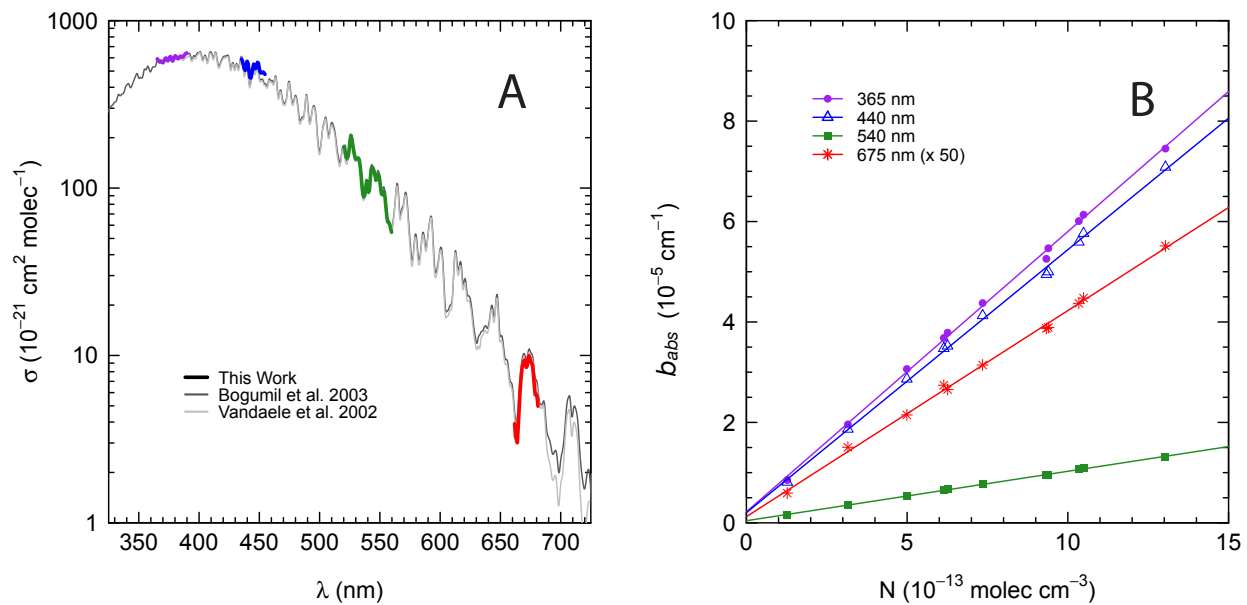


Figure 3.3: Measured NO₂ absorption spectrum (A) and a linear fit of BBCES-measured absorption to known NO₂ number density. The colored lines in (A) represent the BBCES data, while the grey and black lines are from literature sources. The slopes in (B) represent the average absorption cross sections measured over a range of concentrations. See Table 3.2 for fit parameters.

intensity was monitored at 365, 440, 540, and 675 nm. The typical Allan deviation plot presented in Figure 3.4 indicates an ultimate detection limit of approximately 10^{-9} cm^{-1} for each cell. The averaging time of tens of seconds where the Allan deviation reaches a minimum and begins to increase indicates the time at which instrument drift begins to dominate over white noise. It is relatively short compared to similar instruments, and likely limits the ultimate detection limit. [4, 7, 21, 22]. However, we make no effort to actively stabilize the LED temperatures. Thus, the drift likely results from changes in the LED temperatures, which affect both the net intensity and the wavelength dependence of the LED output. To address this in future measurements, the instrument will make use of thermoelectric coolers incorporated in the heatsink assembly to actively cool the LEDs to a constant temperature. Although the detection limit could likely be improved by active LED cooling, it is well below typical levels for ambient aerosol extinction of 10^{-7} cm^{-1} typical for Athens, GA. Similarly, the 1σ detection limit calculated from the standard deviation of the same N_2 measurements, which provides a more accurate measure of an instruments practical (rather than ideal) detection limit, is $3.5 \times 10^{-8} \text{ cm}^{-1}$, well below ambient aerosol extinction.

3.3.3 Ambient Aerosol Extinction and Scattering

A comparison between the UV aerosol extinction measured over several hours by BBCES and CRDS is shown in Figure 3.5. The average agreement between BBCES and CRDS is 5%, attributable to differences in particle loss between the two instruments and uncertainties in dilutions by the purge flows. We use this as a validation that the BBCES responds as expected to changes in aerosol extinction. The instrument's time response was tested further at other wavelengths by comparing the extinction measured by BBCES to scattering measured by a nephelometer over the course of several hours. Figure 3.6 shows that the instruments track well with each other, displaying the same general trend in the magnitude of extinction/scattering and responding to spikes at the same time. The scattering coefficient

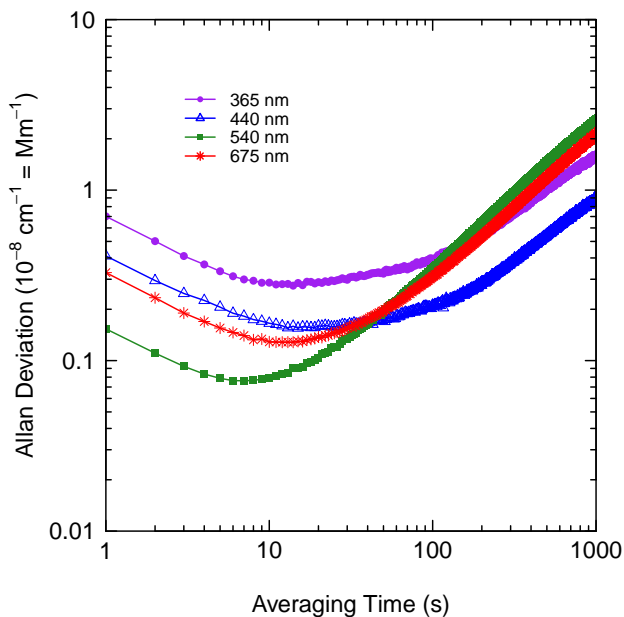


Figure 3.4: Typical Allan deviation plot for each cell calculated from N_2 .

is slightly lower than the extinction coefficient, as expected. Because the BBCES channels overlap with the nephelometer acquisition wavelengths, the single scattering albedo could be calculated for the blue, green, and red channels at each time point in Figure 3.6 by dividing scattering by extinction. We observe the smallest SSA (largest absorption) for the blue channel, followed by the green; the red channel fluctuates near 1. Combined, this suggests a wavelength-dependent absorption that is strongest toward UV wavelengths, agreeing with current models of aerosol extinction. The discrepancies in the blue channel beginning just before 14:30 result from a sudden drift in I_0 , and the measured extinction (and the corresponding SSA) returns to a more normal value after I_0 was re-measured.

The most unique and novel feature of the instrument presented here is its wide wavelength coverage. It provides the ability to retrieve a full UV-visible extinction spectrum. To do this, a power law was fit to BBCES data via non-linear least squares according to $b_{ext} = \beta\lambda^{-\hat{a}}$, yielding the Ångström extinction exponent (\hat{a}) and extinction curve. [23]

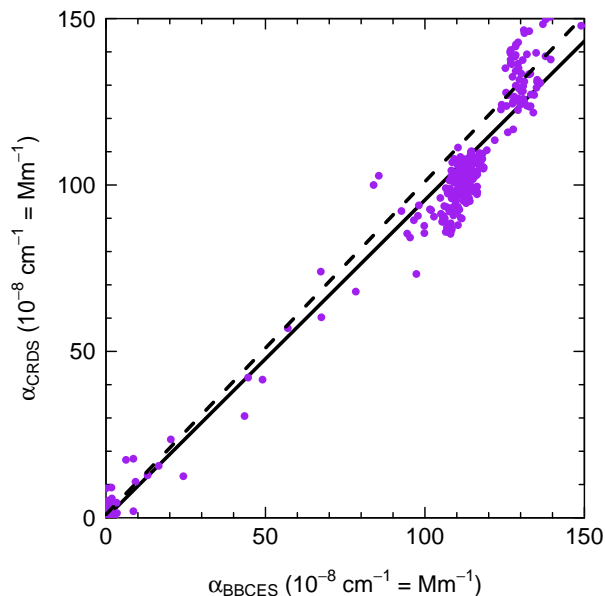


Figure 3.5: Linear regression comparing ambient aerosol extinction measured simultaneously by BBCES (365 nm) and CRDS (355 nm) over several hours. The dotted line represents a 1:1 relationship; the solid line is a fit to the measurements ($y = 0.95x - 2.07 \times 10^{-8}$, $R^2 = 0.9753$).

A similar procedure was performed with nephelometer data to yield the scattering coefficient and curve. The contribution due to absorption was deduced by subtracting the two curves. The results of this analysis are shown in Figure 3.7. Although others have taken this approach using filter based measurements, the results presented here represent the first simultaneous *in-situ* measurements of aerosol scattering and extinction to yield absorption over the entire spectrum.

The SSA measured by the BBCES generally agrees with literature values. SSAs shown in Figure 3.6 measured throughout the day at representative wavelengths provide similar values. This is slightly lower than the average of previous measurements (≈ 0.9), though not outside of the reported range of 0.6–1 [24–27]. Similarly, the extinction spectrum shown in Figure 3.7 agrees with literature and matches CRDS data. The expected exponential

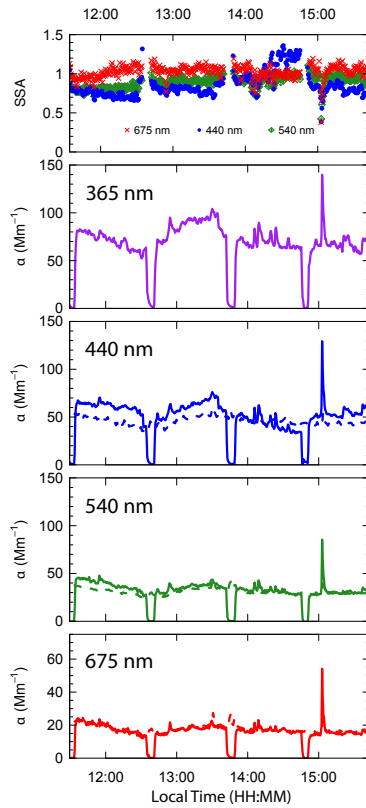


Figure 3.6: Extinction from ambient aerosol measured by BBCES and scattering measured by nephelometry and the retrieved single scattering albedo. BBCES measurements are at 365, 440, 540, and 675 nm; nephelometer measurements are at 450, 550, and 700 nm, integrated over the 40 nm width of the nephelometer's bandpass filter.

wavelength dependence to aerosol extinction is seen for both the overall spectrum and each cell’s respective spectrum, and the greatest difference between scattering and extinction is observed at short wavelengths. The SSA we measured by this method ranges from 0.8 at 450 nm (the lowest nephelometer wavelength) to 1 at 700 nm. SSAs extrapolated in the UV are 0.7–0.8, again in the range of values previously reported for the Southeast (0.65–1). [28] Similarly, The observed wavelength dependence and magnitude of the retrieved absorption spectrum (which peaks at $\approx 1 \times 10^{-7} \text{ cm}^{-1}$ below 400 nm) agrees with previous measurements reported for Athens and Atlanta, GA. [29, 30] However, we note that scattering and extinction measurements are within 1 standard deviation of each other, and the uncertainty on the present absorption measurement is therefore large. Despite this, the retrieved average absorption curve approximates literature values well.

3.4 Major Limitations and Recommendations

This configuration of the BBCES was constructed with pre-existing materials as a proof of concept. It was in some respects a worst-case scenario in terms of signal. Specifically, the radius of curvature of the cavity mirrors must be closely matched to the length of the sample cell for incoherent cavity enhanced spectroscopy to prevent spillover losses of light inside the cavity. [21] Figure 3.8 shows the cell throughput as a function of $1 - L/R$, where L is the cavity length and R is the mirror radius of curvature (R.O.C.), as obtained via a ray-tracing analysis and reprinted here from Keabian et al. [21]. In the original configuration presented here, the BBCES had 6 m R.O.C. mirrors and the cavities were 0.5 m in length, yielding $1 - L/R = 0.92$. Since the data presented here were collected, the mirrors have been replaced with 0.25 m R.O.C. mirrors and the cavities have been shorted to 0.2 m in length, thereby giving $1 - L/R = 0.20$. The corresponding throughput is orders of magnitude better than the previous configuration, and close to the ideal value of L slightly less than R (a value of 0 can only be achieved with a confocal cavity, and is therefore undesirably for most

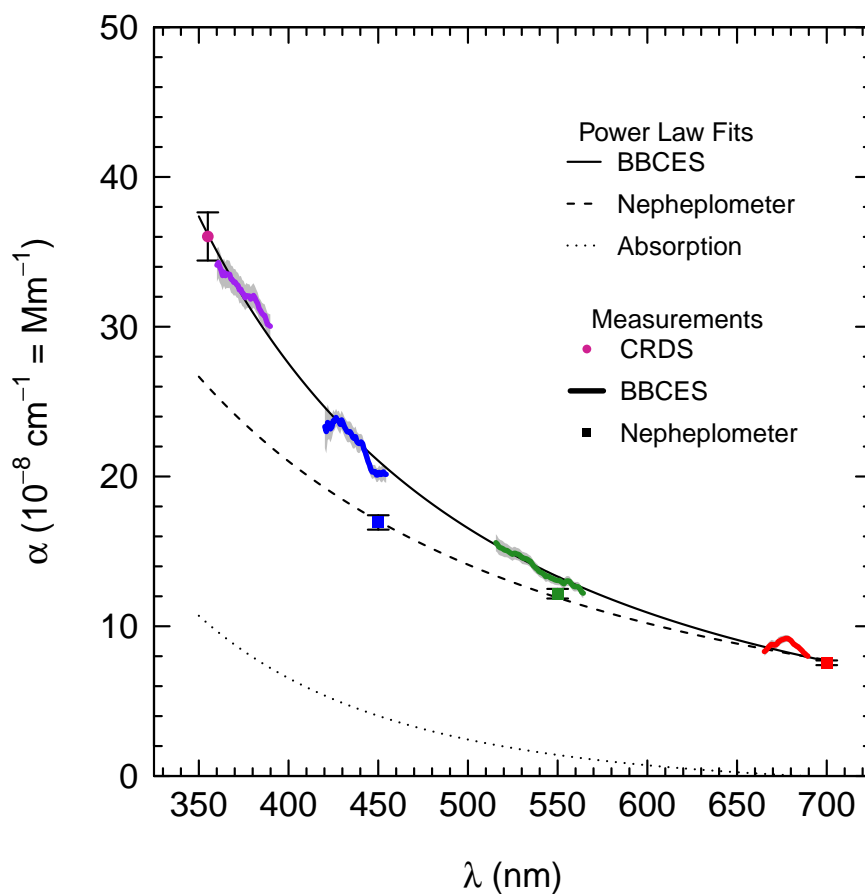


Figure 3.7: Extinction from ambient aerosol measured by BBCES and CRDS, and scattering measured by nephelometry. Values are the mean of 5 subsequent measurements and error bars/shaded regions represent 1 standard error of the mean. Absorption was calculated using the extinction - scattering method.

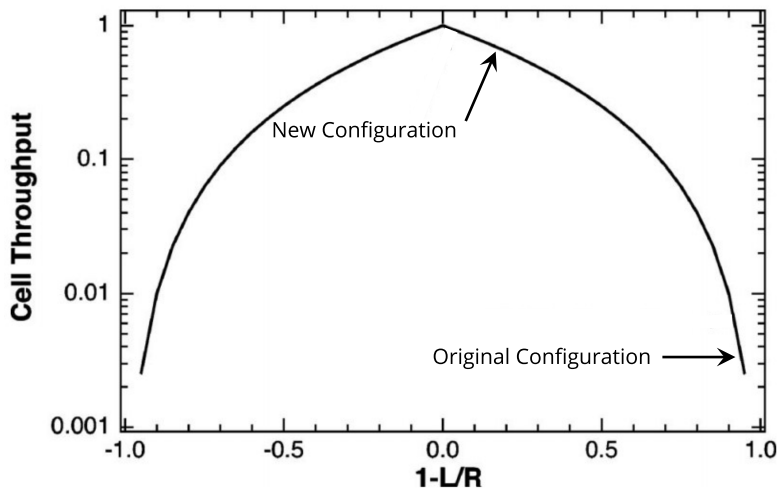


Figure 3.8: BBCES throughput as a function of cavity length and mirror radius of curvature. The original configuration was a worst case scenario for achieving BBCES signal; new mirrors and cavities have largely fixed this issue. Figure reprinted from Keabian et al. [21] with permission from AIP Publishing LLC (but annotated with specifics for this instrument).

circumstances). Preliminary data showed that doing this increased the cell throughput by a factor of 30. Ongoing work with the BBCES in the group has adopted this new configuration with concomitant gains in sensitivity.

3.5 Conclusion

In sum, we have developed a four-channel incoherent broadband cavity enhanced spectrometer with channels in the UV, blue, green, and red regions of the spectrum. The instrument provides windows of coverage throughout the UV-visible spectrum, and is designed to measure ambient aerosol extinction. To that regard, the design uses compact, robust components with low power consumption to enable field deployment. More importantly, the instrument provides an *in-situ* method for measuring aerosol extinction throughout the UV-visible spectrum. Although others have measured aerosol extinction with BBCES over small regions of

the spectrum, the instrument described here makes improvements upon existing methodologies by allowing *in-situ* measurements at throughout the UV-visible spectrum. This novel feature provides overlap with multiple commercial instruments that measure either aerosol scattering or absorption (such as the nephelometer used here), thereby expanding the possibilities of retrieving aerosol optical properties by comparing measurements from multiple instruments. Further, while other broadband measurements have focused primarily on the UV and blue regions of the spectrum where extinction is highest, they have neglected other important wavelengths that are covered by this instrument, such as the representative solar wavelengths near 550 nm used in many models. [31, 32] Finally, the broad spectral coverage provides hundreds of data points throughout the spectrum for determining the Ångströmexponent via a power law fit, a great improvement upon the several wavelengths typically used for such determinations. This not only provides a stronger fit, but also provides visual reassurance that the fit matches the data. We used the instrument to provide the first fully online, simultaneous measurements of aerosol extinction throughout the UV-visible spectrum, and use these measurements to estimate an absorption spectrum. However, we note a large uncertainty in this approach, and future measurements may benefit by combining the instrument with direct absorption techniques such as photoacoustic spectroscopy. Ultimately, measurements such as these will shed light on the ways aerosols directly affect Earth's climate.

References

- (1) Anderson, T. L.; Ogren, J. A. *Aerosol Science and Technology* **1998**, *29*, 57–69.
- (2) Segura, S.; Estelles, V.; Titos, G.; Lyamani, H.; Utrillas, M. P.; Zotter, P.; Prevot, A. S. H.; Mocnik, G.; Alados-Arboledas, L.; Martinez-Lozano, J. A. *Atmospheric Measurement Techniques* **2014**, *7*, 2373–2387.
- (3) Fuchs, H.; Dube, W. P.; Lerner, B. M.; Wagner, N. L.; Williams, E. J.; Brown, S. S. *Environmental Science & Technology* **2009**, *43*, 7831–7836.
- (4) Langridge, J. M.; Ball, S. M.; Shillings, A. J. L.; Jones, R. L. *Review of Scientific Instruments* **2008**, *79*, 123110.
- (5) Thalman, R.; Zarzana, K. J.; Tolbert, M. A.; Volkamer, R. *Journal of Quantitative Spectroscopy and Radiative Transfer* **2014**, *147*, 171–177.
- (6) Washenfelder, R.; Flores, J.; Brock, C.; Brown, S.; Rudich, Y. *Atmospheric Measurement Techniques* **2013**, *6*, 861–877.
- (7) Zhao, W.; Dong, M.; Chen, W.; Gu, X.; Hu, C.; Gao, X.; Huang, W.; Zhang, W. *Analytical Chemistry* **2013**, *85*, 2260–2268.
- (8) Zhao, W.; Xu, X.; Dong, M.; Chen, W.; Gu, X.; Hu, C.; Huang, Y.; Gao, X.; Huang, W.; Zhang, W. *Atmospheric Measurement Techniques* **2014**, *7*, 2551–2566.
- (9) Lack, D. A.; Bahreni, R.; Langridge, J. M.; Gilman, J. B.; Middlebrook, A. M. *Atmospheric Chemistry and Physics* **Mar. 2013**, *13*, 2415–2422.
- (10) Ball, S. M.; Langridge, J. M.; Jones, R. L. *Chemical Physics Letters* **2004**, *398*, 68–74.
- (11) *Cavity-Enhanced Spectroscopy and Sensing*; Gagliardi, G., Loock, H.-P., Eds.; Springer Berlin Heidelberg: 2014.

- (12) Sneep, M.; Ubachs, W. *Journal of Quantitative Spectroscopy and Radiative Transfer* **2005**, *92*, 293–310.
- (13) Shardanand; Rao, A. *NASA Tech. Note* **1977**.
- (14) Bates, D. R. *Planet. Space Sci.* **1984**, *32*, 785–790.
- (15) Toole, J. R.; Renbaum-Wolff, L.; Smith, G. D. *Aerosol Science and Technology* **2013**, *47*, 955–965.
- (16) Vandaele, A. C. *Journal of Geophysical Research* **2002**, *107*, DOI: 10.1029/2001jd000971.
- (17) Bogumil, K.; Orphal, J.; Homann, T.; Voigt, S.; Spietz, P.; Fleischmann, O.; Vogel, A.; Hartmann, M.; Kromminga, H.; Bovensmann, H.; Frerick, J.; Burrows, J. *Journal of Photochemistry and Photobiology A: Chemistry* **2003**, *157*, 167–184.
- (18) Galleani, L.; Tavella, P. *IEEE Transactions on Ultrasonics, Ferroelectrics and Frequency Control* **2009**, *56*, 450–464.
- (19) Huang, H.; Lehmann, K. K. *Applied Optics* **Mar. 2010**, *49*, 1378.
- (20) Kassi, S.; Campargue, A. *The Journal of Chemical Physics* **2012**, *137*, 234201.
- (21) Kebabian, P. L.; Robinson, W. A.; Freedman, A. *Review of Scientific Instruments* **2007**, *78*, 063102.
- (22) Wu, T.; Zhao, W.; Chen, W.; Zhang, W.; Gao, X. *Applied Physics B* **2008**, *94*, 85–94.
- (23) Kokhanovski, A., *Aerosol Optics: light absorption and scattering by particles in the atmosphere*; Springer/Praxis Publishing: Chichester, UK, 2008.
- (24) Mogo, S.; Cachorro, V. E.; Lopez, J. F.; Montilla, E.; Torres, B.; Rodriguez, E.; Benouna, Y.; de Frutos, A. M. *Atmospheric Chemistry and Physics* **2012**, *12*, 5841–5857.
- (25) Lim, S.; Lee, M.; Kim, S.-W.; Yoon, S.-C.; Lee, G.; Lee, Y. J. *Atmospheric Chemistry and Physics* **2014**, *14*, 7781–7793.

- (26) Lambe, A. T.; Cappa, C. D.; Massoli, P.; Onasch, T. B.; Forestieri, S. D.; Martin, A. T.; Cummings, M. J.; Croasdale, D. R.; Brune, W. H.; Worsnop, D. R.; Davidovits, P. *Environmental Science & Technology* **2013**, *47*, 6349–6357.
- (27) Varma, R. M.; Ball, S. M.; Brauers, T.; Dorn, H.-P.; Heitmann, U.; Jones, R. L.; Platt, U.; Pöhler, D.; Ruth, A. A.; Shillings, A. J. L.; Thieser, J.; Wahner, A.; Venables, D. S. *Atmospheric Measurement Techniques* **2013**, *6*, 3115–3130.
- (28) Corr, C. A.; Krotkov, N.; Madronich, S.; Slusser, J. R.; Holben, B.; Gao, W.; Flynn, J.; Lefer, B.; Kreidenweis, S. M. *Atmospheric Chemistry and Physics* **2009**, *9*, 5813–5827.
- (29) Wiegand, J. R.; Mathews, L. D.; Smith, G. D. *Analytical Chemistry* **2014**, *86*, 6049–6056.
- (30) Zhang, X.; Lin, Y.-H.; Surratt, J. D.; Zotter, P.; Prevot, A. S. H.; Weber, R. J. *Geophysical Research Letters* **2011**, *38*, DOI: 10.1029/2011g1049385.
- (31) Alexander, D. T.; Crozier, P. A.; Anderson, J. R. *Science* **2008**, *321*, 833–836.
- (32) Saleh, R.; Robinson, E. S.; Tkacik, D. S.; Ahern, A. T.; Liu, S.; Aiken, A. C.; Sullivan, R. C.; Presto, A. A.; Dubey, M. K.; Yokelson, R. J.; Donahue, N. M.; Robinson, A. L. *Nature Geoscience* **2014**, *7*, 647–650.

CHAPTER 4

A “HYBRID” LASER-LAMP UV-VISIBLE PHOTOACOUSTIC SPECTROMETER

4.1 Introduction

Absorption of light by soot aerosols, often called black carbon (BC), is the second-largest contributor to global warming after CO₂, with an estimated warming affect about 33% that of CO₂'s. [1] It absorbs light strongly throughout the UV-visible spectrum and originates from high temperature combustion of biomass and diesel fuel. Other light-absorbing, carbonaceous aerosols are produced by lower temperature combustion of biomass, and these are usually termed brown carbon (C_{Br}). C_{Br} tends to absorb light primarily in the UV and violet portions of the spectrum, with little to no absorption in the red and near-IR. These two groups of aerosol are the two primary groups of light-absorbing, carbonaceous aerosols. They are in large part defined by the wavelength-dependence of their absorption spectra. That dependence is assumed to follow a power law relationship and is represented by the absorption Ångström exponent (abbreviated AÅE and represented as \mathring{a}):

$$b(\lambda) = \beta\lambda^{-\mathring{a}} \quad (4.1)$$

where b is the absorption (typically in Mm⁻¹), λ is wavelength, and β is a scaling term. BC is typically assumed to have an AÅE of 1.0, while C_{Br} has an AÅE $\gg 1$ (e.g. 2-9). [2, 3] Again, C_{Br} is not a strict definition of aerosol source or composition, but rather a description

of the absorption spectrum. As such, C_{Br} may include sources other than combustion, such as biogenic secondary organic aerosols and primary biogenic aerosols. [1, 4] C_{Br} 's propensity to absorb UV light likely means it is a significant climate forcing agent that is inherently difficult to study optically due to a lack of UV light sources. Measurement of the BC and C_{Br} AAEs is necessary to understand the effects of aerosols on Earth's climate.

Photoacoustic (PA) spectroscopy is a sensitive absorption spectroscopy technique that has been extensively developed for application to gases. [5] It has also become an important technique for directly measuring absorption in aerosols because it is insensitive to scattering. [6–10] Typical photoacoustic instruments employ narrowband, coherent sources such as diode lasers and thus have limited spectral coverage. The need to understand absorbers with broad spectral coverage has driven development of instruments using supercontinuum sources and tunable lasers. [11, 12] These methods notably omit the UV portion of the solar spectrum where aerosol absorption is highest. Further, they are typically large and bulky, which prohibits transport of the instruments for field deployment. One group used a pulsed Nd:YAG to construct a four-cell photoacoustic spectrometer capable of UV-visible measurements at 266, 355, 532, and 1064 nm. [13] Again, the physical bulk of the light source and high power requirements make deploying this instrument in the field very impractical, and the fact that four cells are used requires four separate calibrations and could lead to errors in measuring the AAE. Further, such high-powered, pulsed light sources are likely to vaporize particles and lead to artifacts in the absorption measurements. At the time this instrument was constructed, all *ambient* PAS measurements had been limited to a maximum of 4 wavelengths.

In an attempt to address these issues, Wiegand et al. (2014) used a Hg arc lamp that was bandpass filtered at 8 wavelengths from 300–700 nm via a motorized filter wheel. [14] They measured discrete points of ambient aerosol absorption and retrieved full UV-visible spectra by interpolation between the points via a power law fit. However, this technique was

limited by especially poor sensitivity in the red and violet regions of the spectrum where Hg emission is weak, which in turn significantly limited the instrument's detection limits and—especially in the red—potentially affected the quality of the retrieved spectrum by exerting leverage on the fit. Compounding this, the signal from particulate matter is near or below the instrument's detection limit when ambient concentrations are low. I expanded upon this work by adding two diode lasers to the instrument. This new iteration provides spectral coverage at 8 wavelengths from 300–662 nm with enhanced detection limits in the violet and red regions of the spectrum. Because of the enhanced sensitivity, the instrument is capable of making measurements at UV and the two laser wavelengths even under low particle concentrations. The construction and calibration of the instrument will be discussed, along with its application to ambient aerosol measurements and the limitations associated with the instrument.

4.2 Materials and Methods

4.2.1 Instrument Description

The photoacoustic instrument presented in Wiegand et al. [15] was built upon to create the instrument detailed here. Figure 4.1 shows a diagram of the instrument. The output from a 100 W Hg-Xe arc lamp is focused using a $f/0.8$ lens (40 mm focal length) through a 30-slot optical chopper (Thorlabs). After being modulated by the chopper, the light is collected with a lens identical to the first to re-collimate the beam. The beam is passed through a bandpass filter (Semrock) in series with either a UV short pass filter (Thorlabs) or a 400–700 nm bandpass filter (Thorlabs), dependent on the wavelength, that removes UV and/or IR light that is outside the blocking regions of the bandpass filters. The main bandpass filters have a FWHM of approximately 10 nm, and are chosen to match the Hg emission lines of the lamp where intensity is greatest. Six bandpass filters are held in a motorized filter wheel

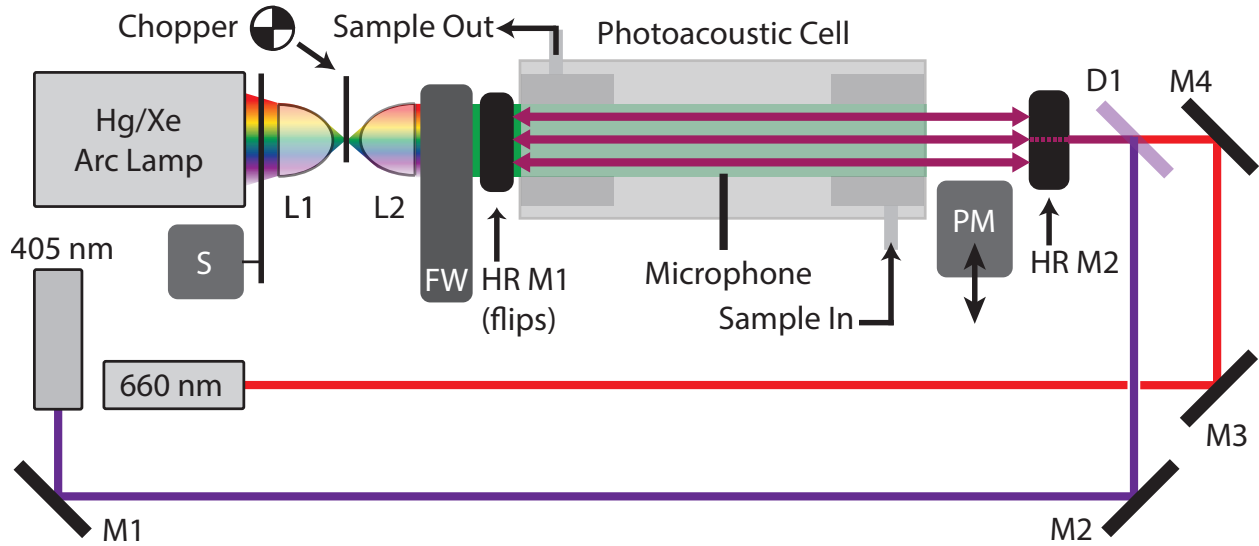


Figure 4.1: Block diagram of the lamp PAS. An arc lamp, chopper, and filter wheel illuminate the cell from the front, while a two lasers enter through the rear of the cell to expand the wavelength coverage and enhance the sensitivity of the PAS. HRM1 is a mirror mounted on a motorized mount for automatic removal when the lamp is used and automatic placement when lasers are used. L = lens; S = shutter; FW = filter wheel; HRM = high-reflectivity cylindrical mirror; PM = power meter; D = dichroic mirror; M = mirror.

(Thorlabs) to allow automated measurements at each wavelength. More details about the filters used in the instrument can be found in Wiegand et al. [15].

After filtering, the light enters the PAS cell via a 25.4 mm diameter quartz window with a broadband antireflective coating. The PAS cell is based on the design of Lack et al. [10] and consists of a custom-machined aluminum resonator that is 150 mm long and 25 mm in diameter, with $\lambda/4$ acoustic filters on either end. An opto-acoustic microphone (Opto-Acoustics 4110) is held at the center point of the PAS cell and used to acquire the PAS signal. The amplified microphone signal is digitized with a USB data acquisition card (National Instruments USB 6210). The light, which is modulated by the chopper at the resonant frequency of the cell, produces a sine wave on the microphone, the magnitude of

which is extracted with a fast-Fourier transform (FFT) performed with a custom LabVIEW program.

The hybrid PAS also contains two diode lasers (Coherent OBIS) operating at 406 and 662 nm. These lasers were added to improve detection limits at two wavelengths where signal was especially weak with the lamp. Prior to measurement, a motorized shutter on the lamp closes to block the lamp beam. Meanwhile, the lasers are made co-linear with a dichroic mirror (Thorlabs). The combined beams approach the PAS cell from the rear, where they pass through a highly reflective ($R > 99\%$) cylindrical mirror via a 2 mm hole drilled in the center (custom coated, Eksma Optics). The lasers pass through the center hole and enter the PAS cell from the rear. An additional cylindrical mirror (identical, but with no central aperture) is held on a custom-built, motorized linear translation stage (controlled by the LabVIEW program via an Arduino) moves into place between the front of the PAS cell and the filter wheel to create a multipass cell that enhances the laser signals by a factor of roughly 30 [16]. The rear mirror is held in a 6-axis, rotatable kinematic mount (Thorlabs) to enable alignment of the multipass cell. The lasers are modulated around the resonant frequency of the cell (-1 Hz and +1 Hz) via the USB DAQ card. The microphone signal then contains the convoluted waveform from the lasers modulated at slightly different frequencies, which are deconvolved using the FFT to allow simultaneous acquisition of both laser wavelengths. After a laser measurement is complete the motorized mirror moves out of the way, the lamp shutter re-opens, and the lamp-based measurements can again be acquired.

4.2.2 Calibration

The hybrid PAS was calibrated with NO_2 , as described in Wiegand et al. [15]. A standard 10.29 ($\pm 5\%$) mixture of NO_2 in N_2 (with O_2 added for stability) was diluted with N_2 to various concentrations. The power-normalized PAS signals from all wavelength where NO_2 does not photodissociate ($\lambda > 420\text{ nm}$) are recorded and plotted against the absorption

calculated from the product of the concentration and absorption cross section to acquire a calibration constant. The power at each wavelength was measured with a thermal power meter (Thorlabs) at the rear of the cell.

4.2.3 Measurement of Multipass Enhancement

The addition of the lasers presents a difficulty for calibration because their powers cannot be directly measured without affecting the multipass cell. To measure it, a strong absorber was introduced to the PAS and measured with a single-pass laser measurement and a multipass measurement. The ratio, $s_{multi}(\lambda)/s_{single}(\lambda)$ represents the enhancement factor for each wavelength and is used to multiply the measured output power of the laser to determine the effective laser power inside the PAS cell. Then, the laser-based measurements can be power-normalized in the same way as the lamp-based measurements so that the same calibration factor can be applied (important at 406 nm where NO_2 photodissociates).

The absorber chosen for this procedure was chlorophyll because it has strong absorption peaks in the violet and the red where the lasers operate. Chlorophyll was extracted in ethanol from baby spinach leaves according to well known methods. Spinach leaves were shredded by hand and placed in a beaker of ethanol (Fisher Scientific). The mixture was sonicated for 5 minutes and the liquid extract poured off. A 3 mL aliquot of this stock extract was filtered through a 0.45 μm syringe filter before dilution to 25 mL with butanol (Sigma-Aldrich), which was chosen due to its relatively high viscosity. The extract was then nebulized using a concentric nebulizer (Meinard) into a flow of nitrogen. The aerosols were delivered to the PAS and measured as described above to determine the multipass enhancement factor. The stock solution was stored in a dark freezer when not in use.

4.2.4 Ambient Aerosol Measurements

Ambient aerosols were collected from the Chemistry Building on the campus of the University of Georgia in Athens, GA (33.948875 N, -83.374428 W) during December 2014 and January 2015. Aerosols were collected into 1/4 inch conductive silicone tubing at a flow rate of 300 SCCM, dried to a dew point of approximately 0° C (25% RH) with a Nafion membrane diffusion dryer (Perma-Pure, Inc.), and delivered to the PA instrument. For background measurements, a HEPA filter (TSI, Inc.) was placed between the Nafion dryer and the cell. The flow was maintained by pulling on the outlet of the cell with a micro diaphragm pump (KNF Neuberger, Inc.).

4.3 Results and Discussion

4.3.1 Calibration and Enhancements

Figure 4.2 shows the calibration curve for the hybrid PAS. When the various wavelengths are normalized to power, they all fall on the same calibration line. This has been observed for other PASs, but an important distinction here is that the 662 nm laser data fall on the same line as well, which indicates proper measurement of the multipass enhancements. The solid line in Figure 4.2 shows the fit to all wavelengths, which yields a best-fit line of $y = 6.6 \times 10^{-4}(\text{V Mm W}^{-1})x - 2 \times 10^{-3}(\text{V W}^{-1})$. Alternatively, a fit to only the red 662 nm points gives a slope of $y = 3.9 \times 10^{-4}(\text{V Mm W}^{-1})x - 4.4 \times 10^{-7}(\text{V W}^{-1})$. Although at first glance this presents a difference of roughly 40%, it is important to note that the fit to the laser data only is based on three points of very low absorption ($<10 \text{ Mm}^{-1}$); with that in mind, the fact that it provides close to the same answer as points spanning two orders of magnitude is encouraging. This calibration highlights an important benefit of using a single PAS cell for all wavelengths instead of a cell for each wavelength as others (e.g. [17]) have chosen to do: It allows for a single calibration constant to be used for all wavelengths.

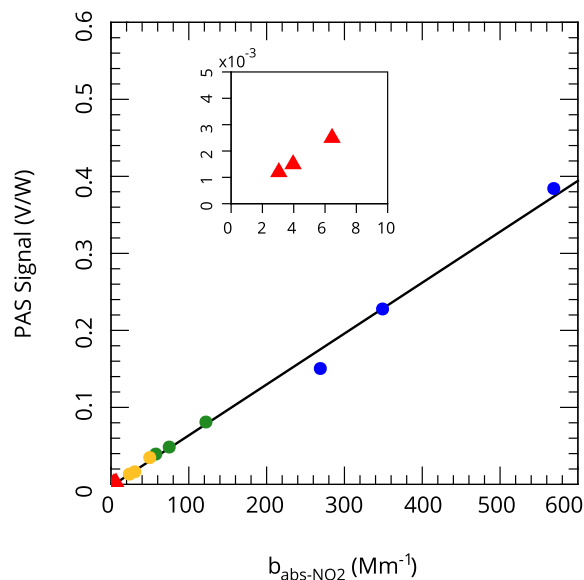


Figure 4.2: Calibration curve for the hybrid PAS. When the wavelengths are normalized to power, they all fall on the same line, regardless if the source is a lamp (circles) or laser (triangles). This allows calibration of shorter wavelengths where NO_2 photodissociates by the same method. Blue = 436 nm, green = 546 nm, yellow = 578 nm, and red = 662nm (laser). The solid line is a fit to all points ($y = 6.6 \times 10^4 x - 2 \times 10^{-3}$); the inset shows a zoomed view of the laser-derived points.

Otherwise, measurements in the UV would be nearly impossible due to a lack of suitable calibrants (both common calibrants, NO_2 and O_3 , photodissociate in the UV). Further, the fact that the laser data also lies on the same line indicates the enhancement measurement with chlorophyll is adequate.

Further supporting the accuracy of the enhancement measurement is Figure 4.3, which shows the spectrum of aerosolized chlorophyll extract in butanol. A solid grey line is the bulk spectrum of the extract acquired with a commercial UV-visible spectrophotometer (Agilent Cary). The points acquired with both the lamp and the lasers reproduce the shape of the bulk spectrum fairly well, which again indicates the enhancement measurement by chlorophyll is suitable. Although the shape is not perfect, it is unlikely the bulk spectrum and aerosol

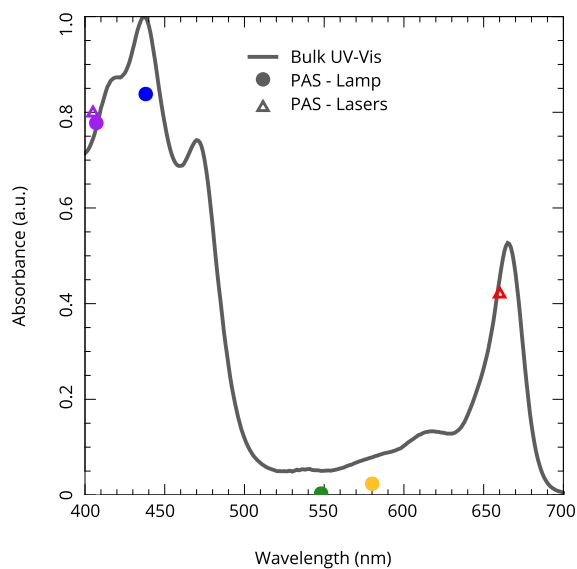


Figure 4.3: Chlorophyll spectrum from the hybrid PAS. Chlorophyll is used to retrieve the effective enhancement of the 406 and 662 nm wavelengths. The fact that this method makes the spectrum acquired with both lasers and the lamp match the bulk spectrum relatively well suggests the enhancement measurements is accurate.

spectrum would match perfectly. Also evident is the fact that the absorption measured with the lamp at 405 nm agrees well with the absorption measured by the laser at 406 nm. The 406 nm laser point takes into account the enhancement measurement, while the 405 nm lamp point is independent of that; again, this indicates that the chlorophyll method is accurately capturing the multipass enhancement.

4.3.2 Ambient Aerosols

An early application of the hybrid PAS was to measure ambient aerosols in Athens, GA. Figure 4.4 shows the spectrum acquired with the hybrid PAS. The spectrum shows lamp-based data at 301, 375, 405, 436, 546, and 578 nm and laser-based data at 406 nm and 662 nm. The wide wavelength coverage allows for easy retrieval of the A \ddot{A} E through a non-linear

least squares fit of Equation 4.1 to the data. The solid line shows a fit to all the data, and the dashed line shows a fit to just the visible points and demonstrates the importance of the UV-spectral coverage provided by the lamp.

Contrasting the benefit of wide spectral coverage are the inherent noise limitations of the lamp. The incoherent nature of the lamp leads to high background signals (which limits the signal-to-background ratio). Further, the large heat output by the lamp leads to an increase in the resonant frequency of the cell upon exposure to light, which introduces drift into the instrument that becomes significant when measuring low absorption levels. Many of the lamp wavelengths are relatively low power compared to what could be achieved with a laser, and the incoherent nature of the light again limits any ability to construct a multipass arrangement. Combined with the short averaging times necessitated by continually switching wavelengths, this led to large error bars and relatively high detection limits with the lamp, which is evident when comparing the lamp based data to the laser-based data (specifically 662 nm) in Figure 4.4. There is also significant scatter in the lamp data, which could result from the drifts in the resonant frequency described above or may result from drifts in the sample composition as the filter wheel cycles through each of the 6 lamp wavelengths, each of which requires about 30 seconds to measure. Despite this scatter, the wide wavelength coverage serves to “average” fluctuations between wavelengths to provide accurate values upon interpolation.

4.4 Summary & Conclusions

The hybrid PAS presented here was based on the work of Wiegand et al. [14]. It was meant to enhance the sensitivity of the instrument by adding two lasers to the instrument. These lasers were operated in a multipass arrangement that enhanced their sensitivity by roughly a factor of 30. Although the instrument provided enhanced wavelength coverage over most existing PASs and aided in retrieving the AÅE, it suffered from several drawbacks. First,

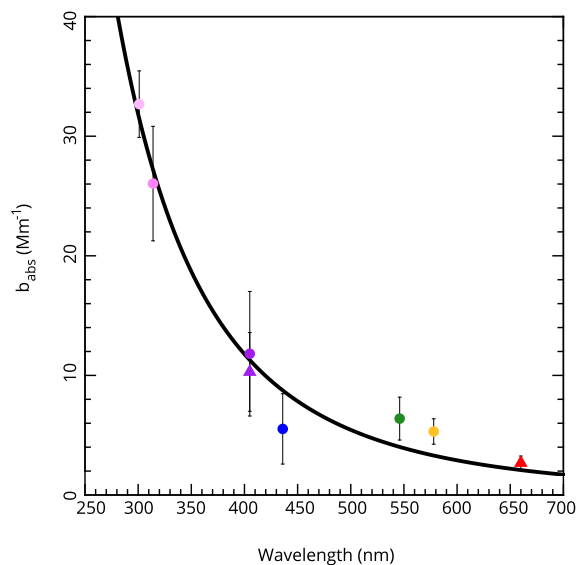


Figure 4.4: Typical ambient spectrum acquired with the hybrid PAS. The solid line is a best-fit to the data using Equation 4.1. Note the much smaller error bars (± 1 SD) on the laser PAS data.

the noise was relatively high compared to what is achievable with a laser PAS. Second, the difficulty presented by reliably measuring the multipass enhancement factors was a practical limitation on a day-to-day basis. Although the chlorophyll method worked for measuring the enhancement for the data presented herein, it was ultimately abandoned for several reasons. First, it was a poor traveler. That is, it required that pressurized nitrogen, a fragile nebulizer, a nebulization flask, a dilution flow, and a light-sensitive solution accompany the PAS wherever it went. Further, the method did not always produce consistent results. Day-to-day measurements could be widely variable and at times did not show agreement with other methods. Finally, the lamp instrument required continual water cooling and “baby-sitting”, and could not be left to run autonomously. Because of these factors, we ultimately decided to pursue expanding wavelength coverage with laser-based PASs that would be based

on the single-cell, multi-wavelength, multipass design and calibration methods developed here. These instruments will be described in chapter 6 and chapter 8 .

The hybrid PAS was also deployed in BC4, a laboratory campaign that took place at Boston College (Boston, MA) in March and April 2015. This campaign focused on understanding the optical properties of soot and absorption in enhancements of coated soot particles. This campaign, and the data from it, are described in chapter 3.

References

- (1) Moosmüller, H.; Chakrabarty, R.; Arnott, W. *Journal of Quantitative Spectroscopy and Radiative Transfer* **2009**, *110*, 844–878.
- (2) Bond, T. C. et al. *Journal of Geophysical Research: Atmospheres* **2013**, *118*, 5380–5552.
- (3) Yang, M.; Howell, S. G.; Zhuang, J.; Huebert, B. J. *Atmospheric Chemistry and Physics* **2009**, *9*, 2035–2050.
- (4) Andreae, M.; Gelencser, A. *Atmos. Chem. Phys.* **2006**, *6*, 3131–3148.
- (5) Miklos, A.; Kung, A. H.; Hess, P. In *Diode Lasers and Applications in Atmospheric Sensing*, ed. by Fried, A., SPIE: 2002.
- (6) Roessler, D.; Faxvog, F. *Applied Optics* **1980**, *19*, 578–581.
- (7) Japar, S. M.; Szkarlat, A. C. *Combustion Science and Technology* **1980**, *24*, 215–219.
- (8) Moosmüller, H.; Arnott, W.; Rogers, C.; Chow, J.; Frazier, C.; Sherman, L.; Dietrich, D. *Journal of Geophysical Research: Atmospheres* **1998**, *103*, 28149–28157.
- (9) Arnott, W. P.; Moosmüller, H.; Rogers, C. F.; Jin, T.; Bruch, R. *Atmospheric Environment* **1999**, *33*, 2845–2852.
- (10) Lack, D. A.; Lovejoy, E. R.; Baynard, T.; Pettersson, A.; Ravishankara, A. R. *Aerosol Science and Technology* **2006**, *40*, 697–708.
- (11) Sharma, N.; Arnold, I. J.; Moosmüller, H.; Arnott, W. P.; Mazzoleni, C. *Atmospheric Measurement Techniques* **2013**, *6*, 3501–3513.
- (12) Haisch, C.; Menzenbach, P.; Bladt, H.; Niessner, R. *Analytical Chemistry* **2012**, *84*, 8941–8945.

- (13) Ajtai, T.; Filep, Á.; Utry, N.; Schnaiter, M.; Linke, C.; Bozóki, Z.; Szabó, G.; Leisner, T. *Journal of Aerosol Science* **2011**, *42*, 859–866.
- (14) Wiegand, J. R.; Mathews, L. D.; Smith, G. D. *Analytical Chemistry* **2014**, *86*, 6049–6056.
- (15) Wiegand, J. R.; Mathews, L. D.; Smith, G. D. *Analytical chemistry* **2014**, *86*, 6049–6056.
- (16) Silver, J. A. *Applied Optics* **2005**, *44*, 6545–6556.
- (17) Lack, D. A.; Richardson, M. S.; Law, D.; Langridge, J. M.; Cappa, C. D.; McLaughlin, R. J.; Murphy, D. M. *Aerosol Science and Technology* **2012**, *46*, 555–568.

CHAPTER 5

UV-VISIBLE ABSORPTION SPECTRUM OF LABORATORY-GENERATED SOOT PARTICLES¹

¹ Fischer, D.A., T. Helgestad, L. Renbaum-Wolff, A. Lambe, S. China, C. Mazzoleni, A. Sedlacek, C. Cappa, A. Freedman, T. Onasch, P. Davidovits, and G.D. Smith. 2018. To be submitted to *Aerosol Science and Technology*.

5.1 Introduction

Soot, often called black carbon (BC), is a carbonaceous material produced from the high-temperature combustion of fossil fuels and biomass. It absorbs light efficiently throughout the UV-visible spectrum. In the atmosphere, this absorption of light by BC aerosols leads to heating of the surrounding air. This contrasts with most other types of particles that only weakly absorb light, if at all, and thus tend to reflect sunlight back toward space and lead to cooling of the atmosphere. Estimates suggest that BC is emitted globally at a rate of 7,500 Gg year⁻¹ and is the second-largest anthropogenic forcing agent behind CO₂. [1, 2] Despite its importance and much effort to understand its role in climate forcing, the parameterization of its interaction with sunlight in global climate models remains a challenge.

The nascent (freshly emitted) BC absorption spectrum can be represented by a power law:

$$b_{abs_{BC}}(\lambda) = \beta\lambda^{-\hat{a}} \quad (5.1)$$

where $b_{abs_{BC}}$ is the absorption due to BC at wavelength λ , β is a scaling factor, and \hat{a} is the absorption Ångström exponent (ÅÅE), a parameter that describes the wavelength-dependence of absorption. For ease of use, this is often referenced to the representative solar wavelength of 550 nm and expressed in terms of mass absorption coefficient (MAC), as in:

$$MAC(\lambda) = MAC_{550} \left(\frac{\lambda}{550\text{nm}} \right)^{-\hat{a}} \quad (5.2)$$

where MAC_{550} is often taken to be 7.5 (± 1.2) m²g⁻¹ based on the review of Bond and Bergstrom [3] and the ÅÅE is assumed to be 1.0. This functional form has the advantage that it provides a simple way to calculate the spectrum for nascent BC without requiring specific knowledge of microphysical parameters such as morphology, refractive index, or

density. However, uncertainties associated with the values of MAC_{550} and $A\AA E$ translate into significant uncertainties on calculations of radiative transfer involving BC particles. [2] These uncertainties can also translate into sizable uncertainties on brown carbon absorption at UV/blue wavelengths inferred from the difference between measured absorption and BC absorption extrapolated using Equation 5.2. [4] What is more, it is not even clear that a power law function with a single value of the $A\AA E$ accurately describes BC absorption over the entire UV-visible spectrum [3, 5], in part because of the dearth of MAC measurements spanning these wavelengths.

This work will present, to the best of our knowledge, the first UV-visible spectrum for laboratory-generated nascent BC. The spectrum was obtained with multiple, independently developed instruments, which provided an opportunity for an intercomparison of measurements. We support the generally accepted literature value of $MAC_{550} = 7.5 \text{ m}^2 \text{ g}^{-1}$, but cannot support a value of 1.0 for $A\AA E_{BC}$. In other words, we find good agreement between the visible measurements presented here and literature values, but find statistically significant deviations at UV wavelengths.

5.2 Materials and Methods

Experiments were conducted during March and April of 2015 at Boston College in Chestnut Hill, Massachusetts as part of a laboratory campaign named “BC4”. The campaign was designed as an in-depth study of the optical, chemical, and morphological characteristics of soot. The optical portions of the experiment involved research groups from academia (University of California Davis, Boston College, and University of Georgia), industry (Aerodyne Research, Billerica, Massachusetts), and government (Brookhaven National Laboratory, Upton, New York). Soot was generated in the laboratory and dispersed to various instruments to measure the optical properties, size, and mass of the particles. A block diagram of the overall experiment is shown in Figure 5.1, and each portion will be described in detail below.

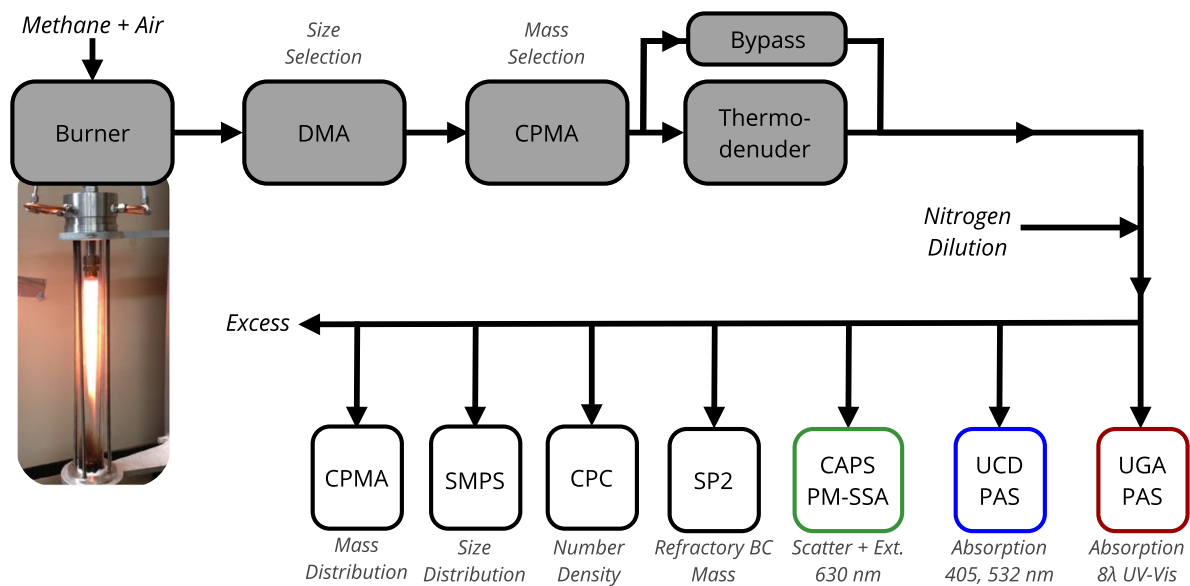


Figure 5.1: Block diagram of the experimental setup for BC4. DMA: differential mobility analyzer, CPMA: centrifugal particle mass analyzer, UGA PAS: Univ. of Georgia photoacoustic spectrophotometer (301, 314, 364, 405, 436, 546, 578, 662 nm), UCD PAS: Univ. of California – Davis cavity ringdown/photoacoustic spectrophotometer (405, 532 nm), CAPS PM_{SSA}: Aerodyne cavity attenuated phase shift single-scattering albedo monitor (630 nm), SP2: single particle soot photometer, CPC: condensation particle counter, SMPS: scanning mobility particle sizer.

5.2.1 Particle Generation

Soot particles were generated by combusting methane in an inverted co-flow diffusion flame burner at Boston College with a sheath flow mixture of O₂ and N₂. The burner was operated at net equivalence ratios of 0.6–0.9 (lean conditions). This burner was designed for an especially stable output and produces soot particles with a low organic carbon to elemental carbon ratio (O:C). Soot particles were eluted from the flame, size selected, mass selected, and diluted with clean, dry nitrogen before delivery to the various instruments via a copper sample line.

5.2.2 Particle Size and Mass Selection

Particles were passed through a static neutralizer to impart a net charge +1 on particles (though some end up with a +2 charge, see below) for size selection by the DMA. Particles were then selected by electric mobility diameter with a differential mobility analyzer (DMA; TSI model 3080) using a sheath-to-sample flow ratio of 5:1 to provide a $\pm 20\%$ width on the selected size distribution. The particles were then selected by mass using a centrifugal particle mass analyzer (CPMA; Cambustion). The distribution of particle masses was measured using a single particle soot photometer (SP2; Droplet Measurement Technologies), from which the fraction of particles containing one or two charges (with particle mass twice that of the singly-charged particles) was determined. The fraction of doubly-charged particles ranged from 0% to 19%. The effective per-particle-mass was calculated as the average of the masses of the singly- and doubly-charged particles weighted by the respective measured fractions. A second CPMA provided an additional measure of the mass distribution, and a scanning mobility particle sizer (SMPS, TSI 3936) provided a measure of the size distribution. The particle concentration was measured using a condensation particle counter (CPC; TSI), and

the particle mass concentration was calculated from the product of this value and the effective per-particle mass.

5.2.3 Optical Instrumentation

Three different instruments were used to measure the absorption, scattering, and extinction by suspended aerosol particles: the CAPS PM_{SSA} simultaneously measures aerosol extinction based on cavity attenuated phase shift spectroscopy (CAPS) and aerosol scattering based on integrating nephelometry, which is calibrated from the extinction measurement. [6] Aerosol absorption is calculated from the difference in the extinction and scattering measurements. The instrument can operate at a variety of wavelengths limited by the availability of appropriate high-reflectivity mirrors and LEDs; the model used in the present study operates at 630 nm. The UCD PAS/CRD system consists of two PAS instruments (405 and 532 nm) equipped with a multipass mirror set for increased sensitivity to measure absorption and cavity ringdown (CRD) instruments to measure extinction, also at 405 nm and 532 nm. [7, 8] The UGA lamp/laser PAS is similar to the lamp-only PAS described previously [9], but automated, moveable mirrors have been added on either end of the PAS cell to make possible a laser multipass arrangement in conjunction with the lamp (Figure 4.1). Thus, the instrument sequentially measures absorption at six narrow wavelength bands using dichroic filters to select light from the mercury arc lamp (301, 314, 364, 436, 546, and 578 nm), and then the multipass mirrors are moved into position and absorption at 405 nm and 662 nm is measured simultaneously using diode lasers with the multipass arrangement. Both the UCD PAS and the UGA PAS are calibrated using known concentrations of NO_2 .

5.3 Results and Discussion

5.3.1 Instrument Intercomparison

The co-location of the two PAS instruments and the CAPS PM_{SSA} instrument provided us with an opportunity to compare the performance of each. Both the UCD PAS and the UGA PAS employ a 405 (± 1) nm laser, so it is straightforward to compare the instruments at this wavelength (Figure 5.2A). Comparison at 532 nm is accomplished by deriving an interpolated value at 532 nm from the UGA data using a power law function fit to the spectrum (Figure 5.2B). The UCD and UGA data are compared to the CAPS PM_{SSA} 630 nm data by extrapolating (for the UCD PAS) or interpolating (for the UGA PAS) with a power law function (Figure 5.2C). The data were compared by performing a linear regression with each of the pairs. The linear fits were forced through zero due to the scatter in the data. Although this assumes there is no systematic offset between the instruments, it provides higher correlation coefficients than those obtained by not forcing through 0. This suggests any offsets obtained by floating the intercept may not be statistically meaningful due to the relatively scattered nature of the data.

As the Figure 5.2 demonstrates, the instruments in general exhibit very good correlation. Correlation coefficients (R^2) are > 0.98 for all wavelengths/instruments compared and > 0.99 for all but one. Slopes are within 10% for all but one comparison, which is the UCD vs. UGA 405 nm comparison with a slope of 1.15. Although this agreement is not perfect, it is good considering most of these comparisons are done with interpolated and/or extrapolated data. Curiously, the only direct comparison, at 405 nm, is the worst. This could be due to a systematic error in the UGA multipass cell power determination, a systematic error in the calibration of the UCD PAS, or a combination of both. Further, it may be a demonstration of the “averaging” power of using values interpolated from a fit to 8 wavelengths rather than a single wavelength; while the fit tends to smooth out scatter between wavelengths in the

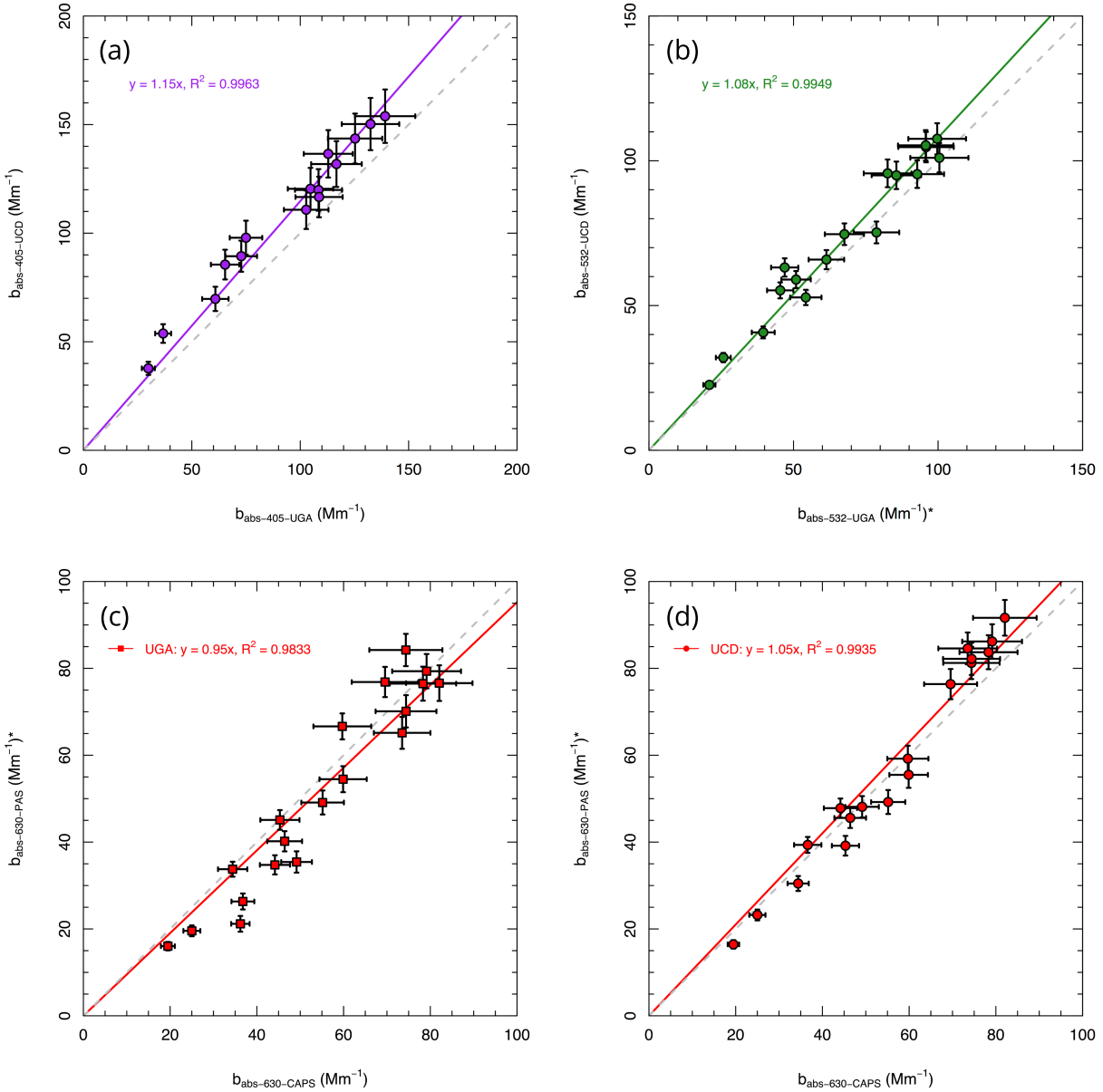


Figure 5.2: Comparison of soot absorption measurements at BC4. Linear least-squares fits (solid and dot-dash lines) of soot absorption measurements. (a) UCD PAS 405 nm vs. UGA PAS 405 nm measurements, (b) UCD PAS 532 nm vs. UGA PAS 532 nm (interpolated using a power law fit to all eight wavelengths), (c) UGA PAS 630 nm (extrapolated using power law fit to 405/532 nm data) and, (d) UCD PAS 630 nm (interpolated using power law fit to all eight wavelengths) vs. CAPS PM_{SSA} 630 nm. Dashed [grey] lines represent 1:1 correlation. Uncertainty bars represent 68% confidence intervals. Asterisks in axis titles denote interpolated data.

UGA PAS, this scatter has not been removed in the 405 nm comparison because the two measurements were compared directly.

5.3.2 Black Carbon MAC & AÅE

The mass absorption cross section (MAC) is a measure of particle absorption normalized to mass concentration, and is commonly used to relate aerosol mass to its effect on radiative transfer in models.

$$MAC = \frac{b_{abs}}{M} \quad (5.3)$$

Here, b_{abs} is the absorption (in Mm^{-1}) and M is the aerosol mass concentration (in $\mu g m^{-3}$). There is a long history of black carbon and soot MAC measurements that has been reviewed and summarized by Bond and Bergstrom [3]. In their review, they recommend a value of $7.5 (\pm 1.2) m^2 g^{-1}$ for the MAC_{550} of BC based on an assessment of 17 studies. The widespread use of this MAC_{550} value for both estimating the radiative forcing of soot particles as well as for testing and benchmarking computational approaches has warranted continued study to reduce the uncertainty on it. In this work, the concurrent measurement of the particle mass with the CPMA allowed us to calculate the MAC values from the slopes of measured absorption plotted against particle mass concentration, as shown in Figure 5.3. Table 5.1 lists the MAC values and the associated uncertainties as well as the R^2 values from each of the linear fits in Figure 5.3. The uncertainties were estimated by propagating the uncertainties on the regressions from Figure 5.3 (represented as the 68% confidence limits from the fit) and the estimated uncertainties for the UCD PAS (8% for 405 nm and 5% for 532 nm), UGA PAS (10% at all wavelengths), CAPS PMSSA (5%), CPMA (2%), and CPC (5%) instruments. The CPMA uncertainty of $\pm 2\%$, was derived from a “challenge” using polystyrene latex spheres (PSLs) of three different diameters in which the limiting source of uncertainty was

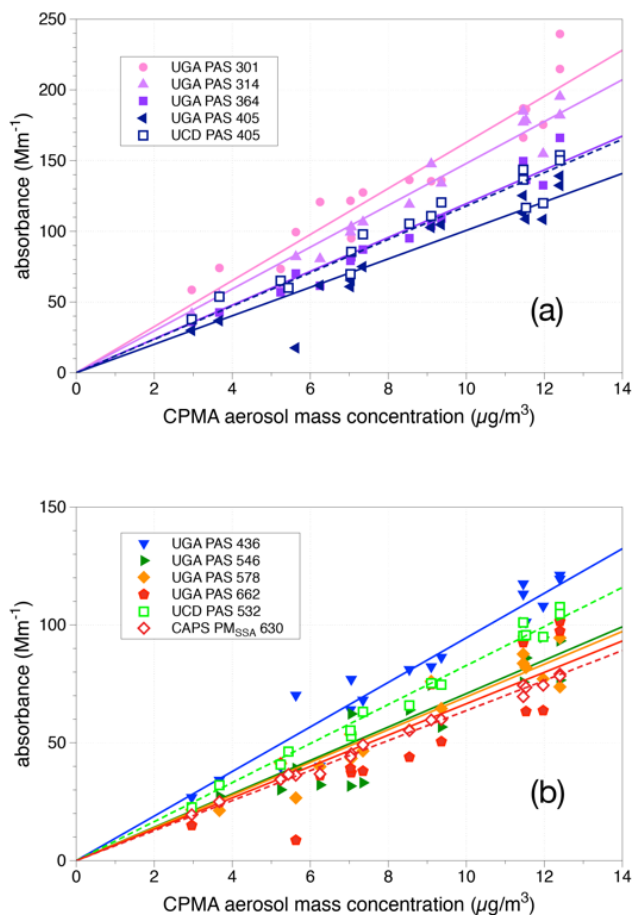


Figure 5.3: Nascent soot mass absorption cross sections measured by the three instruments, UGA PAS, UCD PAS, and CAPS PM_{SSA} as a function of mass concentration as measured with the CPMA and CPC. Slopes yield the mass absorption cross sections at each wavelength (listed in Table 5.2). (a) UV wavelengths, (b) visible wavelengths.

the density of the PSLs. The CPC number density uncertainty was estimated as $\pm 5\%$ in line with previous studies in which CPCs have been compared to CRD measurements of particle extinction [10] or an electrometer [11].

Table 5.2 provides a review of the values measured or derived from studies made on suspended (i.e. not captured on filters), laboratory-generated combustion particles conducted since Bond & Bergstrom’s 2006 review along with their recommendation and the results

Table 5.1: Compilation of mass absorption cross sections (MACs) measured in this work. Uncertainties represent 68% confidence intervals

Instrument	Wavelength (nm)	MAC m^2g^{-1}	Uncertainty m^2g^{-1}	R^2
UGA PAS	301	16.3	1.9	0.90
UGA PAS	314	14.8	1.7	0.96
UGA PAS	364	12.0	1.4	0.96
UGA PAS	405	10.1	1.2	0.88
UGA PAS	436	9.50	1.1	0.93
UGA PAS	546	7.10	0.9	0.83
UGA PAS	578	6.90	0.8	0.91
UGA PAS	662	6.70	0.9	0.76
UCD PAS	406	11.8	1.2	0.92
UCD PAS	532	8.30	0.6	0.98
CAPS PM_{SSA}	630	6.40	0.1	0.99

from the present study. The average of these more recent studies (not including the present study) is $7.4 \text{ m}^2 \text{ g}^{-1}$, which substantiates the recommended value of $7.5 \text{ m}^2 \text{ g}^{-1}$. However, the standard deviation of these measurements ($1.0 \text{ m}^2 \text{ g}^{-1}$) reflects a range of values that is not much smaller than the spread of earlier values reviewed by Bond and Bergstrom. The value from the present study, $7.54 (\pm 0.43) \text{ m}^2 \text{ g}^{-1}$, derived by fitting the data from all three instruments at 10 different wavelengths, provides further validation of the recommended MAC_{550} value. What is more, the careful consideration of the sources of uncertainty for both the absorption and particle mass measurements and the use of three different instruments for making absorption measurements offer a high degree of confidence in this value.

Figure 5.4 shows the MACs plotted against wavelength. The solid black line represents the best fit to a power law, which yields $A\ddot{A}E_{BC} = 1.21$ and $MAC_{550} = 7.54 \text{ m}^2 \text{ g}^{-1}$. The uncertainties include only instrument uncertainties (PAS or CAPS PM_{SSA}) and that of the regression from Figure 5.2 and do not include the CPMA or CPC uncertainties. We did this because the shape of the spectrum is not affected by the particle mass or number density

measurements since all three instruments measured absorption on the same aerosol sample. With our numbers, Equation 5.2 becomes:

$$MAC(\lambda) = 7.54(\pm 0.43) \text{ m}^2\text{g}^{-1} \left(\frac{\lambda}{550 \text{ nm}} \right)^{-1.21(\pm 0.08)} \quad (5.4)$$

where the uncertainty on the AÅE (± 0.08) is determined from the 68% confidence interval from the non-linear regression. The uncertainty on the pre-factor, which is equal to the MAC at 550 nm, includes the same uncertainties as well as the uncertainties from the CPMA ($\pm 2\%$) and the CPC ($\pm 5\%$) since those affect the magnitude of the mass absorption cross section.

For reference, the grey dashed line in Figure 5.4 represents the MAC spectrum using the commonly assumed values of $7.5 \text{ m}^2\text{g}^{-1}$ at $\lambda = 550 \text{ nm}$ and $A\ddot{A}E = 1.0$. Despite the close agreement between the two power law functions at wavelengths $> 500 \text{ nm}$, the shapes of the curves are clearly different. In fact, we can say with statistical significance ($p < 0.05$) that the AÅE of 1.21 (± 0.08) is greater than 1.0. Thus, to the extent that a power law is used to describe the absorption spectrum of black carbon particles throughout the UV-visible spectrum, the use of $A\ddot{A}E = 1.0$ underestimates absorption at the UV wavelengths. We point out, however, that a value of $A\ddot{A}E = 1.0$ does describe the visible part of the spectrum well.

Table 5.2 also lists values of the AÅE derived from the same set of studies, all of which were calculated using measurements at visible wavelengths except for that of Ajtai et al. [21]. The AÅEs range from 1.03 to 1.48, and this wide range can have important consequences for extrapolating MAC values back to the UV; for example, the MAC calculated at 300 nm ranges from 14.0 to 18.4 m^2g^{-1} (assuming $MAC_{550} = 7.5 \text{ m}^2\text{g}^{-1}$), a 31% difference depending on whether a value of 1.03 or 1.48 is used. This uncertainty translates into uncertainties in radiative transfer calculations, estimation of brown carbon contribution to

Table 5.2: Literature Review of MAC_{550} and AÅE for laboratory-generated soot since the review of Bond and Bergstrom [3].

Reference	MAC_{550} m^2g^{-1}	AÅE	Source	Notes
This Work (combined)	$7.54 (\pm 0.43)'$	$1.21 (\pm 0.08)$	Methane Flame	10λ , 2 PAS + 1 CAPS
This Work (UCD)	7.93 (fit to UCD)	1.30	methane flame	UCD PAS (405+532nm)
This Work (UGA-vis)	7.45	0.95	methane flame	UGA PAS (6 λ , vis only)
Yu et al. [12]	$7.16 (\pm 1.3)^*$	—	high-T, high-P combustion	PAS (532nm)
Saliba et al. [13]	7.45^*	—	cookstove, european white birch bark	PAX (532nm)
You et al. [14]	$7.89 (\pm 0.25)^\ddagger$	$1.03 (\pm 0.09)$	Cab-O-Jet pigment	PAS (550–840nm)
Radney and Zangmeister [15]	$5.2 (\pm 1.4)^\ddagger$	$1.2 (\pm 0.04)$	ethylene flame	PAS (500–840nm)
Olson et al. [16]	$6.50 (\pm 0.86, SE)^{*,*}$	—	kerosene soot	7 λ aethalometer w/ PAX correction
Olson et al. [16]	$7.78 (\pm 0.07, SE)^{*,*}$	—	diesel soot	7 λ aethalometer w/ PAX correction
Wei et al. [17]	$9.0 (\pm 2.7)^{*,\dagger}$	—	kerosene soot	$b_{ext} - b_{scat}$ (532nm)
Coderre et al. [18]	$6.5 (\pm 0.5)^\clubsuit$	1.05	methane flame	diffuse light line-of-sight attenuation (450–750nm)
Cross et al. [19]	$7.94 (\pm 1.7)^{*,\dagger}$	1.48 (+0.53/-0.64)	ethylene flame	PASS-3 (405, 532, 781nm)
Cross et al. [19]	$7.19 (\pm 0.5)^{*,\dagger}$	—	ethylene flame	PTI (532nm)
Cross et al. [19]	$8.40 (\pm 0.4)^{*,\dagger}$	—	ethylene flame	PAS (532nm)
Ajtai et al. [20]	—	$1.24 (\pm 0.08)$	mini-CAST burner with propane	PAS (266, 255, 532, & 1064nm)
Bond and Bergstrom [3]	$7.5 (\pm 1.2)^\dagger$	1.0	—	literature review

*Scaled to 550 nm using a power law function

' 68% confidence interval

‡ 2 standard deviations

† 1 standard deviation

* standard error

♣ 95% confidence interval

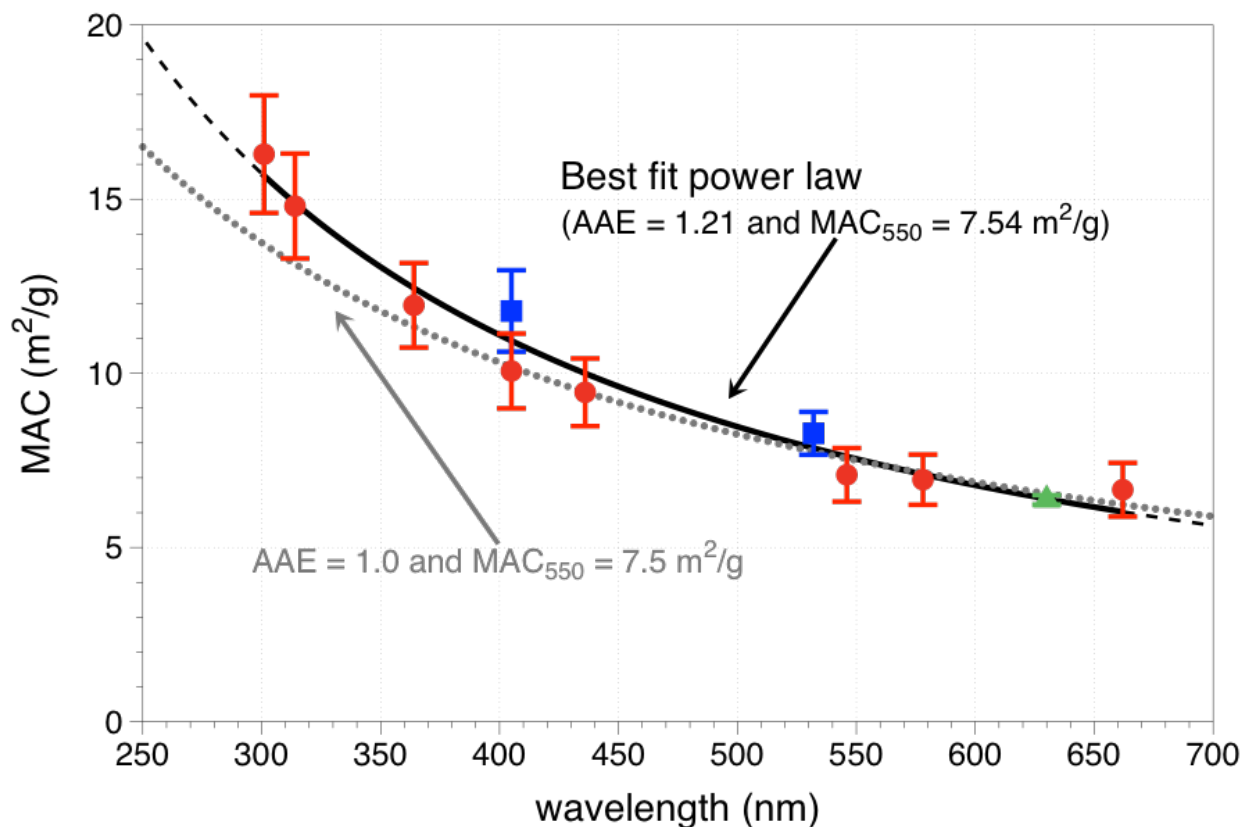


Figure 5.4: UV-visible mass absorption spectrum measured for nascent soot particles using the UGA PAS ([red] circles), UCD PAS ([blue] squares), and CAPS PM_{SSA} ([green] triangle). The solid curve is the best fit power law function to all data with the dashed extensions representing extrapolation of that function beyond wavelengths measured. The dotted curve represents a power law function using the commonly assumed values for the AAE and MAC_{550} . The largest discrepancies between the two functions appear at UV wavelengths. Uncertainty bars include respective instrument uncertainties and 68% confidence intervals on the linear fits used to derive MAC values Figure 5.3.

absorption, and UV solar fluxes with implications for gas-phase photochemistry. The $\text{A}\ddot{\text{A}}\text{E}$ from the present work of 1.21 (± 0.08) falls in the middle of the range of values in Table 5.2, most of which were derived from measurements at visible wavelengths. If we exclude our UV wavelengths and just use the visible ($\lambda = 405$ nm) measurements, the fit also yields a value of $\text{A}\ddot{\text{A}}\text{E} = 1.21$ but with a larger uncertainty (± 0.16), and thus we conclude that the visible $\text{A}\ddot{\text{A}}\text{E}$ is not statistically different than the commonly assumed value of 1.0. If we further limit our dataset to just the UGA visible ($\lambda \geq 405$ nm) data, since they were collected over a wide spectral range with a single instrument, we obtain a value of 0.95 (± 0.22). Again, we conclude that it is not statistically different than 1.0. So, considering the published $\text{A}\ddot{\text{A}}\text{E}$ values in Table 5.2, the recommendation of Bond and Bergstrom [3], and the visible $\text{A}\ddot{\text{A}}\text{E}$ values from the present work, we conclude that for the purposes of representing the MAC of BC in the visible region of the spectrum, a power law function with $MAC_{550} = 7.5 \text{ m}^2 \text{ g}^{-1}$ and $\text{A}\ddot{\text{A}}\text{E} = 1.0$ is sufficient. We caution, however, that this parameterization does not appear to hold at UV wavelengths and its use would result in an underestimation of BC absorption there (see Sections 3.2 and 3.3).

Although a single power law fits the data decently throughout the UV-visible spectrum and the BC absorption spectrum is commonly assumed to have the functional form of a power law, there is no physical reason the particles from our flame must do so. In fact, if brown carbon were present as a coating on the BC particles it could lead to a spectrum with a dual power law form. In the data from all three instruments, instrument-to-instrument scatter masks any wavelength dependence to the $\text{A}\ddot{\text{A}}\text{E}$. However, because the UGA UV-vis PAS is a single cell PAS, any systematic errors in the absorption measurement will not affect the measured $\text{A}\ddot{\text{A}}\text{E}$. Figure 5.5A shows the $\text{A}\ddot{\text{A}}\text{E}$ obtained only with the UGA PAS. Distinct $\text{A}\ddot{\text{A}}\text{E}$ s for the UV and visible portions of the spectrum can be observed. The $\text{A}\ddot{\text{A}}\text{E}$ of the visible portion of the spectrum is 0.95, close to the literature value of 1.0 for BC. The $\text{A}\ddot{\text{A}}\text{E}$ for the UV portion of the spectrum is slightly larger at 1.58. This would be consistent with a

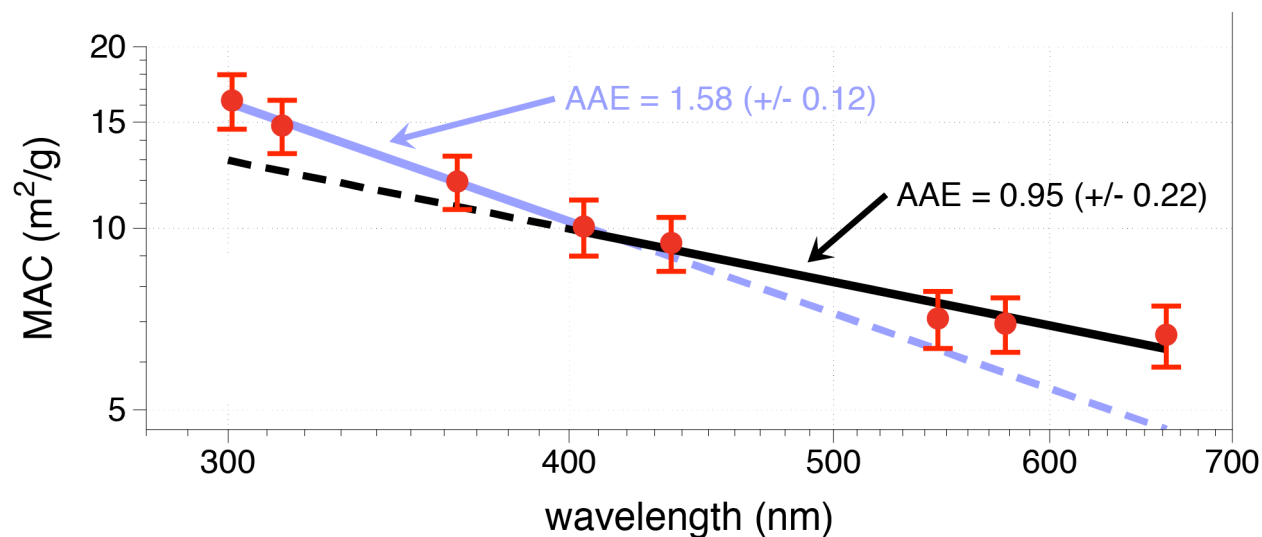


Figure 5.5: Mass absorption cross section (MAC) measured with the UGA PAS with power law fits to just the UV data ($\lambda \leq 405$ nm) (grey [purple] solid line and just the visible data ($\lambda \geq 405$ nm) (black solid line). Uncertainty bars represent propagation of instrument uncertainty (10%) and the 68% confidence intervals on the linear fits used to derive MAC values (Figure 3). Plotted in log-log fashion, the slopes of the lines are the negative of the absorption Ångström exponents (AAEs), which are statistically different (uncertainties are 68% confidence intervals on the power law fits). Dashed lines are extrapolations of the fits.

high-MAC organic or brown carbon coating on the particles that would increase absorption in the UV but not the visible. This is an area that warrants future study, and could benefit from being paired with non-optical techniques that could support the presence of an organic coating (e.g. aerosol mass spectrometry and electron microscopy).

5.4 Conclusions

The value of MAC_{550} agrees favorably with the best-accepted literature value of $7.5 (\pm 1.2)$ $\text{m}^2 \text{g}^{-1}$, which is based on an assessment of 17 studies, and also agrees with the more recent studies reviewed here. However, the commonly assumed value of 1.0 for AAE_{BC} seems to differ from our measured value of 1.21. We are able to say with statistical certainty that the

AÅE measured using the three instruments used here differs significantly from the commonly assumed value of 1.0. However, this difference is primarily in the UV, where comparable measurements are lacking. We note that when systematic instrument-to-instrument errors are removed by looking only at the UGA PAS data, the spectrum is better fit by a dual power law with an AÅE of approximately 1 for the BC-only portion of the spectrum (longer wavelengths) and an AÅE of 1.58 for the brown-carbon influenced portions of the spectrum (UV and blue wavelengths). This could be a result of high-MAC brown carbon coatings that originate in the flame and have not yet been observed with visible techniques, or could simply be due to the fact that adding more fit parameters will inevitably provide a better fit. Thus, this finding is preliminary and should be explored further in conjunction with techniques capable of measuring the brown carbon content of the particles. At present, we can conclusively say the value of $7.5 \text{ m}^2 \text{ g}^{-1}$ is suitable for use as MAC_{550} for BC; further, an AÅE 1.0 is likely suitable for the visible portion of the spectrum, but probably underestimates UV absorption, and the UV absorption spectrum of BC should be studied further moving forward.

5.5 Acknowledgements

This work was conducted as part of the “BC4” laboratory campaign at Boston College in Chestnut Hill, Massachusetts during March and April 2015. It was conducted in collaboration with Taylor Helgestad¹, Lindsay Renbaum-Wolff^{2,3}, Andy T. Lambe^{2,3}, Arthur J. Sedlacek⁴, Chris Cappa¹, Andrew Freedman³, Tim B. Onasch³, Paul Davidovits², Geoffrey D. Smith⁵.

¹ Department of Civil and Environmental Engineering, University of California, Davis, California 95616, USA ² Department of Chemistry, Boston College, Boston, Massachusetts 02467, USA ³ Aerodyne Research, Inc. Billerica, Massachusetts 01821, USA ⁴ Environmental and Climate Sciences Department, Brookhaven National Laboratory, Upton, NY, USA ⁵ Department of Chemistry, University of Georgia, Athens, Georgia 30602, USA

References

- (1) Jacobson, M. Z. *Nature* **2001**, *409*, 695–697.
- (2) Bond, T. C. et al. *Journal of Geophysical Research: Atmospheres* **2013**, *118*, 5380–5552.
- (3) Bond, T. C.; Bergstrom, R. W. *Aerosol Science and Technology* **2006**, *40*, 27–67.
- (4) Lack, D. A.; Langridge, J. M. *Atmospheric Chemistry and Physics* **2013**, *13*, 10535–10543.
- (5) Bergstrom, R. W.; Pilewskie, P.; Russell, P. B.; Redemann, J.; Bond, T. C.; Quinn, P. K.; Sierau, B. *Atmospheric Chemistry and Physics* **2007**, *7*, 5937–5943.
- (6) Onasch, T. B.; Massoli, P.; Keabian, P. L.; Hills, F. B.; Bacon, F. W.; Freedman, A. *Aerosol Science and Technology* **2015**, *49*, 267–279.
- (7) Langridge, J. M.; Richardson, M. S.; Lack, D.; Law, D.; Murphy, D. M. *Aerosol Science and Technology* **2011**, *45*, 1305–1318.
- (8) Lack, D. A.; Richardson, M. S.; Law, D.; Langridge, J. M.; Cappa, C. D.; McLaughlin, R. J.; Murphy, D. M. *Aerosol Science and Technology* **2012**, *46*, 555–568.
- (9) Wiegand, J. R.; Mathews, L. D.; Smith, G. D. *Analytical Chemistry* **2014**, *86*, 6049–6056.
- (10) Toole, J. R.; Renbaum-Wolff, L.; Smith, G. D. *Aerosol Science and Technology* **2013**, *47*, 955–965.
- (11) Liu, B. Y.; Pui, D. Y. *Journal of Colloid and Interface Science* **1974**, *47*, 155–171.
- (12) Yu, Z.; Assif, J.; Magoon, G.; Keabian, P.; Brown, W.; Rundgren, W.; Peck, J.; Miakel-Lye, R.; Liscinsky, D.; True, B. *Aerosol Science and Technology* **2017**, *51*, 1438–1447.

- (13) Saliba, G.; Subramanian, R.; Saleh, R.; Ahern, A. T.; Lipsky, E. M.; Tasoglou, A.; Sullivan, R. C.; Bhandari, J.; Mazzoleni, C.; Robinson, A. L. *Aerosol Science and Technology* **2016**, *50*, 1264–1276.
- (14) You, R.; Radney, J. G.; Zachariah, M. R.; Zangmeister, C. D. *Environmental Science & Technology* **2016**, *50*, 7982–7990.
- (15) Radney, J. G.; Zangmeister, C. D. *Analytical Chemistry* **2015**, *87*, 7356–7363.
- (16) Olson, M. R.; Garcia, M. V.; Robinson, M. A.; Rooy, P. V.; Dietenberger, M. A.; Bergin, M.; Schauer, J. J. *Journal of Geophysical Research: Atmospheres* **2015**, *120*, 6682–6697.
- (17) Wei, Y.; Ma, L.; Cao, T.; Zhang, Q.; Wu, J.; Buseck, P. R.; Thompson, J. E. *Analytical Chemistry* **2013**, *85*, 9181–9188.
- (18) Coderre, A. R.; Thomson, K. A.; Snelling, D. R.; Johnson, M. R. *Applied Physics B* **2011**, *104*, 175–188.
- (19) Cross, E. S. et al. *Aerosol Science and Technology* **2010**, *44*, 592–611.
- (20) Ajtai, T.; Filep, Á.; Schnaiter, M.; Linke, C.; Vragel, M.; Bozóki, Z.; Szabó, G.; Leisner, T. *Journal of Aerosol Science* **2010**, *41*, 1020–1029.
- (21) Ajtai, T.; Filep, Á.; Utry, N.; Schnaiter, M.; Linke, C.; Bozóki, Z.; Szabó, G.; Leisner, T. *Journal of Aerosol Science* **2011**, *42*, 859–866.

CHAPTER 6

MULTIPAS-IV: A PORTABLE, FOUR-WAVELENGTH, SINGLE-CELL PHOTOACOUSTIC SPECTROMETER FOR AMBIENT AEROSOL ABSORPTION¹

¹ Fischer, D.A and G.D. Smith. 2017. *Aerosol Science and Technology*. DOI: 10.1080/02786826.2017.1413231. Reprinted here according to the usage guidelines of the publisher, Taylor & Francis.

6.1 Introduction

Atmospheric aerosols directly affect Earth’s climate by scattering and absorbing solar radiation, thereby altering the radiative balance of the Earth. Uncertainties on aerosol effects are among the largest for making predictions of Earth’s future climate, and aerosol optical properties have thus become an area of intense research in recent years [1]. Absorbing aerosols consist primarily of carbonaceous aerosols and mineral dust. Two species compose light absorbing carbonaceous aerosols: black carbon (BC), which results from combustion of fossil fuels, biofuels, and biomass and absorbs light relatively evenly throughout the UV-visible spectrum, [2] and brown carbon (C_{Br}), which results from incomplete combustion, smoldering biomass, and secondary and biogenic sources and absorbs primarily at ultraviolet and blue wavelengths [3, 4].

Aerosol absorption has historically been a difficult quantity to measure, and [5] provide an extensive review of measurement techniques. Many methods involve collecting aerosols on a filter, extracting the collected particulate matter, and measuring the UV-visible spectrum of the soluble fraction with a spectrophotometer. These methods are still widely employed with great utility but suffer from well-known artifacts associated with filter collection and extraction, most notably that the optical properties are measured in solution and not of suspended aerosol. Other filter-based methods involve collecting aerosols on a filter and measuring changes in the transmission through the filter in real-time and are employed by instruments such as the aethalometer and the particle soot/absorption photometer (PSAP). These methods are well known to suffer from artifacts related to the filter, including filter-loading and multiple scattering effects that can lead to a higher perceived absorption compared to in-situ measurements [6–8]. The multiangle absorption photometer (MAAP) corrects for multiple scattering by measuring direct and diffuse backscattering by the filter [9], though it still can suffer from filter loading effects.

The so-called "subtraction method" does not rely on a filter but instead calculates the absorption from the difference of extinction and scattering by suspended particles. [10] However, at large single scattering albedo (SSA) values when extinction is dominated by scattering, typical of many ambient aerosols, even a modest 3% error in the SSA can translate to a large error (60%) in absorption calculated from the difference. [11] Typically, the least error-prone methods for measuring aerosol absorption are photothermal methods in which light absorbed by particles creates a thermal/pressure wave, which is detected with a microphone (photoacoustic spectroscopy) or an interferometer (optical homodyne interferometry). [12–14] Because these methods measure absorption by suspended particles directly, they avoid filter-based artifacts and potentially large uncertainties possible with the subtraction method. Of the photothermal methods, photoacoustic spectroscopy (PAS) has been most widely applied, likely due to the relative simplicity of the equipment, the feasibility of creating compact, portable instruments, and the availability of commercial instruments. PAS, in rudimentary form, was first described by Alexander Graham Bell but was not widely applied until the mid- to late-twentieth century due to a lack of technology to make the technique viable. [15, 16] In 1977, [17] made the first reported PAS measurements of aerosol absorption, and since then it has seen increasing application in aerosol science due to its insensitivity to scattering, which makes it well suited for measuring aerosol absorption.

The first portable PAS instruments for measuring aerosol absorption at wavelengths in the visible (532 and 685 nm) by Moosmüller et al. [13] and near-IR (802 nm) by Petzold and Niessner [18] were developed in the 1990s with detection limits reaching $< 1 \text{ Mm}^{-1}$. In 2006, Arnott et al. [19] reported the first PAS measurements of aerosol absorption aloft, while in the same year Lack et al. [20] demonstrated enhanced sensitivity by employing a multi-pass laser (532 nm) alignment with a limit of detection of 0.08 Mm^{-1} . Lewis et al. [21] later combined two lasers (405 and 870 nm) in a single photoacoustic cell providing spectral coverage while simplifying operation by requiring calibration at only one wavelength. That

instrument evolved into a three-wavelength (405, 532, 781 nm) version commercialized as the PASS-3 (Droplet Measurement Technologies; Boulder, CO). Ajtai et al. [22, 23] expanded spectral coverage by using the fundamental (1064 nm) and three higher-order harmonics (266, 355, 532 nm) of a Nd:YAG laser with four separate cells. Lack et al. [24] deployed three of their multipass instruments (404, 532, 659 nm) on an aircraft with detection limits of 0.5–1.5 Mm^{-1} , and Cappa and co-workers continue to use similar instruments (405 and 532 nm) to make a variety of laboratory- and field-based measurements (e.g. [25]). Recently, Haisch et al. [26] has used a tunable optical parametric oscillator and Sharma et al. [27] and Radney and Zangmeister [28] have employed supercontinuum lasers to measure aerosol absorption in the laboratory at wavelengths throughout the visible and near-IR regions of the spectrum; these can take on the order of several-to-tens of minutes to collect a spectrum and are not yet portable. In 2014, our group developed a Hg lamp-based instrument able to measure absorption at eight narrow wavelength bands from 301 nm to 687 nm [29], though it, like the supercontinuum-based instruments, has a low duty cycle and is not field deployable.

Here, we describe a photoacoustic instrument for measuring aerosol absorption at four wavelengths (406, 532, 662, and 785 nm) contained in a single acoustic resonator, which we call the MultiPAS-IV. The instrument employs a multipass design to increase sensitivity, which is based on the design of Lack et al. [24, 30] but differs in that it is the first such implementation with a single set of mirrors for four wavelengths in a single photoacoustic cell. This design affords us the advantage of a single calibration applicable to all wavelengths, just like other multi-wavelength, single-cell instruments, thus reducing errors in measuring the wavelength dependence of the absorption. In that sense, it is similar to the PASS-3 instrument and the three-wavelength (445, 532, 660 nm) PAS of Linke et al. [31]; however, we show how the ability to measure at blue, green, red, and near-IR wavelengths allows us to measure the wavelength dependence (i.e. absorption Ångström exponent) of the BC component ($A\text{ÅE}_{BC}$) and subsequently the contribution by C_{Br} and the $A\text{ÅE}_{C_{Br}}$, as well.

Consequently, it is not necessary to assume particle mixing state or the BC spectral shape (e.g. AÅE) as is commonly done. We demonstrate how the small size, weight, and power requirements coupled with the sub-Mm⁻¹ detection limits of the instrument make it uniquely capable of making such measurements with ambient aerosols even under relatively clean conditions.

6.2 Materials and Methods

6.2.1 Instrument Description

The photoacoustic instrument described herein is designed to measure absorption by aerosols at four wavelengths in the visible and near-IR region of the spectrum. It employs four lasers coupled into a single acoustic resonator. The acoustic signals for each wavelength are measured simultaneously, and one of the lasers is split to a cavity ringdown (CRD) spectrometer for calibration of the PAS and as a simultaneous measure of extinction during aerosol sampling. The system is compact, low power (< 400 W), lightweight (34 kilograms), and is mounted in a standard Pelican case (63 cm x 50 cm x 37 cm) for easy transport.

6.2.2 Operating Principles

Both PAS and CRD have been thoroughly described elsewhere, including detailed accounts of their applications to aerosols. [5, 16, 30, 32–34], so they will be described only briefly here. In PAS, signal is generated only by absorbed light. When a sample absorbs light modulated at an acoustic frequency (typically 1-2 kHz) it will induce a pressure wave detectable with a microphone. The intensity of the microphone signal is then directly proportional to the absorption by the sample. Typically, the modulation frequency is chosen to match a resonant frequency of the sample cell, thereby achieving resonant amplification.

For CRD, we use a wide-bandwidth (1 nm) diode laser to excite many longitudinal modes of a high-finesse optical cavity consisting of two highly reflective mirrors ($R = 99.9985\%$). When light couples into the cavity, an intensity build up is observed, and when the laser is quickly switched off the light decays exponentially with a decay constant, τ , on the order of tens of microseconds. This time constant provides a direct measurement of the extinction coefficient, α_{ext} , if the baseline (aerosol-free) ringdown time, τ_0 , is known:

$$\alpha_{ext} = \frac{R_l}{c} \left(\frac{1}{\tau} - \frac{1}{\tau_0} \right) \quad (6.1)$$

Here, R_l is the ratio of the total mirror-to-mirror cavity length to the occupied sample cell length and accounts for purge volumes protecting each of the mirrors, and c is the speed of light.

6.2.3 Acousto-opto-mechanical System

The general opto-mechanical system for the MultiPAS-IV is shown in Figure 6.1. It employs four diode lasers (Coherent OBIS) that emit at 406, 532, 662, and 780/785 nm with powers of 80 mW (532 nm) and 100 mW (406, 662, 780/785 nm). We note that when the 785 nm laser was repaired partway through the project, the laser diode was replaced resulting in a shift to a wavelength of 780 nm; thus we list this laser as “780/785 nm.” All data presented in this work were collected with the 785 nm laser except for the nigrosin experiments (6.4), which employed the 780 nm laser. The beams from each of the four lasers pass through Faraday isolators to minimize back reflections into the lasers and then to a series of dichroic mirrors (Semrock) to make them co-linear. Once combined, the beams are turned with a mirror into a multipass cell consisting of two custom-coated cylindrical mirrors with reflectivity $>99\%$ at each of the PAS wavelengths (25.4 mm diameter, $f = 50$ mm, Eksma/Altos Photonics). The front mirror contains a 2 mm central aperture to allow entry of the laser

beams and is held in a rotatable mount to allow alignment of the cylindrical mirrors with respect to each other until a dense multipass pattern is produced [35]. Theoretically, as many as 200 passes are possible with such an arrangement, though in practice we just measure the effective power enhancements at each wavelength, which are functions of the window transmission and mirror reflectivity, and are 30x, 40x, 56x, 40x for 406, 532, 662, and 785 nm, respectively.

The custom-machined, aluminum PAS sample cell is placed between the multipass mirrors such that the beam pattern is transmitted through the acoustic resonator inside the cell and the custom AR-coated windows (Evaporated Coatings, Inc.) with reflectivity $> 99.5\%$ on either end of the cell. The resonator is 150 mm long and 25 mm in diameter with $\lambda/4$ acoustic filters on either end to reduce noise from the windows; its design has been described elsewhere [24, 30]. An optoacoustic microphone (Optimic 4110) is placed at the center point of the resonator for transduction of the signal. The resonant frequency of the cell, typically 1370 Hz for air at room temperature, is determined by monitoring the microphone signal as the modulation frequency of one of the lasers is scanned. The quality factor, Q , of the resonant mode is 30, as determined from the full width at half maximum of the frequency scan [30] (see Figure A.1).

The small amount of light passing through the rear multipass mirror is turned and focused onto a photodiode (Thorlabs PDA100A) with a 50 mm focal length concave mirror (Thorlabs CM508-050-E02) for continuous monitoring of effective laser power within the cell. Most of the PAS optics are mounted in a cage system to minimize thermal drift and avoid misalignments. Particle losses through the PAS cell are measured to be $< 5\%$ while there are no NO_2 losses within measurement uncertainty.

The CRD operates only at 662 nm. A 90:10 beamsplitter (Thorlabs BSX10) is used in place of a dichroic mirror such that 10% of the 662 nm beam is sent to the CRD cell, which consists of two highly reflective mirrors ($R=99.9985\%$, FiveNine Optics) 25.4 mm in diameter

and with a focal length of 0.5 m. The mirrors are held in custom-machined mounts that are in turn held in standard kinematic mirror mounts (Thorlabs KM100). Light exiting the rear of the cavity passes through a bandpass filter and is focused onto an avalanche photodiode (APD, Thorlabs APD410A) for detection. The sample enters and exits the cavity through 1/4" stainless steel tubing connected to the cell at 45 degrees; a purge of 50 standard cubic centimeters (SCCM) of nitrogen (Airgas) is maintained over each mirror to avoid deposition of particles.

6.2.4 Electronics and Data Acquisition

For simultaneous acquisition of signal at all four wavelengths, the lasers are digitally modulated near the resonant frequency of the cell with square waves at four separate frequencies generated by a microcontroller (32 bit 180 MHz ARM Cortex-M4/Teensy 3.6, PJRC.com). These frequencies are spaced by 2 Hz to eliminate interference when they are deconvolved. A 24-bit USB sound card (ICUSBAUDIOMH, Startech.com) sampling at 44 kHz digitizes the signal collected by the microphone. A custom LabVIEW program is used to process the signal and perform a fast Fourier transform (FFT) to deconvolute the four laser signals. An identical sound card is used to digitize the photodiode signal, and a FFT is similarly performed to monitor the effective power at each wavelength.

For CRD, the APD signal is sent to an oscilloscope (PicoScope 2000A), which acquires the decays and stores them in an on-board buffer before sending a block of waveforms to LabVIEW. Once in LabVIEW, the decays are co-added and fit to an exponential function using the discrete Fourier transform method [36–38].

6.2.5 Calibration

The PAS is calibrated using NO₂ gas (1-5 ppm in N₂) with the CRD measuring the absolute absorbance at 662 nm. A regression of the PAS signal against the CRD absorption gives

the PAS cell's calibration coefficient. Because the same laser is used for both the CRD and PAS, any uncertainties in the laser wavelength and/or NO₂ absorption cross-section are irrelevant. An example calibration plot is shown in Figure A.2A demonstrating the validity of this approach with close agreement between measurements of NO₂ absorption at 532, 662, and 780 nm. We also note that this approach is similar to the calibration procedure for other PAS instruments, including the PASS-3 in which NO₂ or kerosene soot is used to calibrate the cell at 532 nm and this calibration is used for the other wavelengths (405 and 781 nm). To apply the same calibration coefficient to each channel, though, the relative powers of each of the lasers must be known. Thus, the photodiode behind the PAS is used to measure the effective power in the cell and is calibrated to a thermal power meter (Thorlabs S310C) by removing the PAS cell from the optical setup and measuring the power and photodiode signal of a single pass. The laser power is varied electronically, and the regression slope of the photodiode signal vs. the laser power provides the photodiode calibration factor at each wavelength. Nigrosin aerosol was generated using a constant output atomizer (TSI 3076) with an aqueous solution of nigrosin (Sigma Aldrich CAS# 8005-03-6); particles were dried by passing them through two diffusion driers in series.

6.2.6 Ambient Sampling

Ambient sampling was conducted from the Chemistry Building on the campus of University of Georgia in Athens, GA (33.948869, -83.374632) during March 2017. Athens may be considered a clean sub-urban site in terms of air quality with few local sources of aerosols during early spring aside from traffic. As such, the aerosols may be considered well-aged, "background" aerosols.

6.2.7 PAS and CRD

For PAS and CRD measurements, air was drawn through a Nafion membrane dryer (PermaPure) with a N₂ (Airgas) sheath flow and dried to < 10% relative humidity. Aerosols were carried through a short length of 1/4" conductive silicone tubing (TSI, Inc.) to an automated valve (N-Research). The valve was controlled by the LabVIEW program and alternately allowed aerosol-laden air to pass for 24 minutes and then HEPA-filtered air for five minutes. This filtered measurement included contributions from any gas-phase absorbers, such as NO₂, which were then subtracted from the aerosol measurements. In a polluted environment in which the concentrations of such species are large, rapidly changing concentrations over the sampling period could skew aerosol absorption measurements, though we point out that most other PAS instruments are affected by the same issue. An additional minute was used to measure the resonant frequency of the cell by scanning the 406 nm modulation frequency and then to automatically adjust the frequency of all lasers accordingly. Since the resonant frequency of the cell is a function of temperature (2 Hz per °C), this frequent adjustment accounted for any temperature drift that may have occurred over the previous 30 minutes. Three fans mounted to the case provided exchange of air but otherwise there was no active temperature regulation. After exiting the PAS cell, the sample flowed through a small length of grounded copper tubing to the CRD cell and then to a critical orifice (200 micrometer hole diameter, Lenox Laser) and diaphragm pump (KNF Neuberger, Inc.) that sets the total flow rate (330 SCCM). Flows larger than 400 SCCM were found to increase acoustic noise substantially, presumably from turbulent flow. Data were saved by the LabVIEW program.

Aethalometer

An AE33 7-wavelength, dual-spot aethalometer with Teflon-coated glass fiber filter tape was used for aethalometer measurements (Magee Scientific). Air was drawn through a silica-

gel diffusion dryer ($RH < 10\%$) and delivered to the aethalometer via the 1/4" conductive tubing provided by the manufacturer. The aethalometer's built in pump was used to provide flow at the factory-default flow rate, and all other default settings were likewise used for the aethalometer. Specifically, it was set to report data every 60 seconds with a 5-minute rolling average. Data were logged directly to the aethalometer and retrieved after sampling for post-processing. A multiple-scattering correction factor of 1.57 [8] was applied internally by the aethalometer.

Scanning Mobility Particle Sizer

Particle size distributions were collected every five minutes by using a scanning mobility particle sizing spectrometer (SMPS; TSI 3080 electrostatic classifier and TSI 3553 condensation particle counter). A 0.0457 cm impactor was used on the electrostatic classifier with a sample flow rate of 300 SCCM and a sheath flow rate of 3000 SCCM.

6.3 Instrument Performance

6.3.1 Detection Limits

Allan deviation [39] provides a measure of an instrument's long-term stability and has been widely used to provide the detection limits for instruments. We conducted an overlapping Allan deviation analysis (Figure 6.2a) by flowing dry nitrogen gas through the PAS cell for approximately 11 hours while recording the microphone signal. The microphone signal was normalized to the photodiode signal but was otherwise uncorrected for changes in the background (e.g., from drifts in the resonant frequency). The inflection point in the Allan deviation curve when plotted on a log-log scale represents the averaging time for which drift dominates over random noise as the primary source of error. The instrument was found to be stable to at least 1000 seconds for all channels, which indicates that drift will only limit

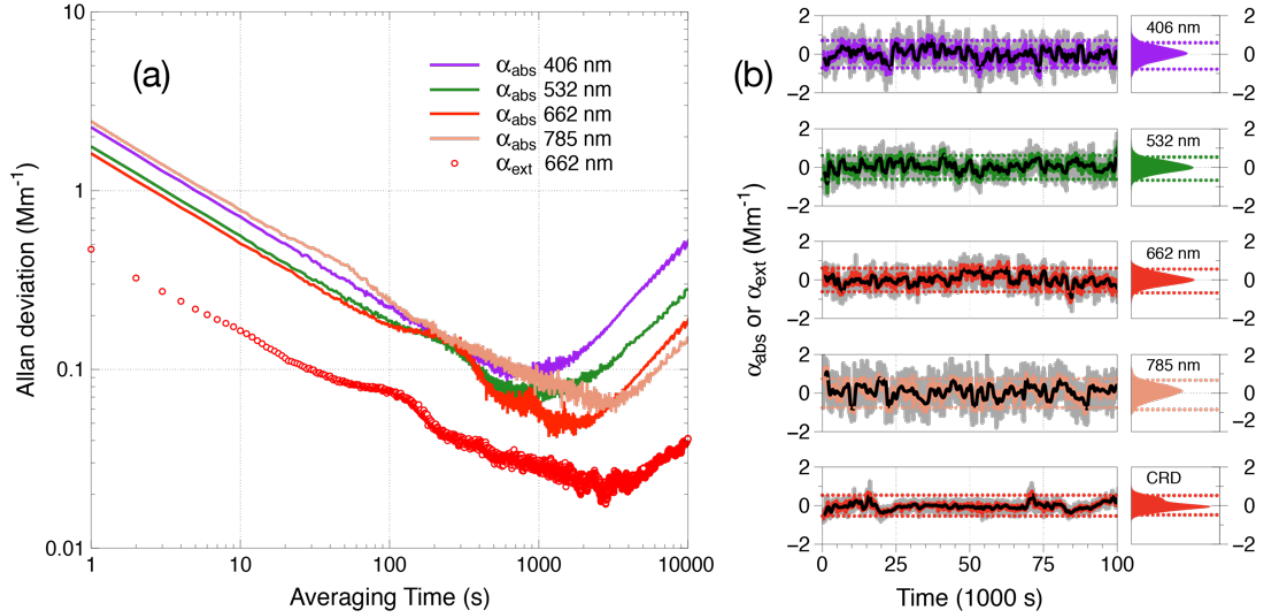


Figure 6.2: (a) Allan deviation plot of absorption (PAS, solid lines) and extinction (CRD, open circles) data collected with nitrogen gas. (b) Time series and histograms of same data with re-zeroing every 30 min to simulate standard operation of the instruments (30 s average: dark grey lines, 2 min average: light grey (colored) lines, 10 min average: black lines). Dotted lines indicate ± 2 standard deviations of the 2-min average data

the ability to achieve the ultimate detection limit after this time unless the instrument is re-zeroed. In making ambient measurements, we re-zero every 30 minutes (1800 seconds), and thus drift does not significantly degrade the detection limits. The longer stability of the red and near-IR channels is likely due to the fact that those two channels are closer to the exact resonant frequency of the cell (± 1 Hz) than the blue and green channels (± 3 Hz) and are therefore likely less influenced by small changes in the resonant frequency and/or quality factor, Q , of the cell. The ultimate detection limits (2σ) observed from Allan deviation range from 0.1 Mm^{-1} at 662 nm to 0.2 Mm^{-1} at 406 nm.

Allan deviation provides a best-case scenario for the detection limit, and the standard deviation may provide a more accurate indicator of the practical detection limit. We therefore performed an alternate analysis on the nitrogen data in which they were corrected for baseline

drift by averaging two-minute “background” blocks once every thirty minutes. The two background measurements from either side of each 28-minute “sample” period were averaged and subtracted from the sample period data, a method similar to that used by Nakayama et al. Nakayama et al. [40]. The standard deviations then provide a measure of the instrument’s practical detection limit, here limited by the two-minute average of the background data. The background-subtracted time series are shown in Figure 6.2b together with histograms of the data. Based on the standard deviation of that data, we calculate two-minute method detection limits (2σ) of 0.71, 0.62, 0.61, and 0.75 0.4 Mm^{-1} for the 406, 532, 662, and 785 nm PAS wavelengths, respectively, and 0.54 Mm^{-1} for the 662 nm CRD. These limits are sufficient to measure absorption and extinction of ambient aerosol under all but the cleanest of conditions (see Figure 6.3, for example).

The detection limits for the MultiPAS-IV compare favorably to those reported for other PAS instruments. For example, Nakayama et al. report 10-minute average, 2σ detection limits for the PASS-3 of 1.0 (405 nm), 1.9 (532 nm), 0.4 Mm^{-1} (781 nm) [40], and Linke et al. [31] recently reported 2σ limits of 3.7 (445 nm), 4.4 (532 nm), and 0.4 Mm^{-1} (660 nm) for their 3-wavelength, single cell PAS, as well. The instruments of Lack and co-workers, upon which the MultiPAS-IV was based, exhibit much lower 2σ detection limits than it does: 0.16 0.4 Mm^{-1} (532 nm, 60 second average) [30] and 0.2 (404 nm), 0.15 (532 nm), and 0.4 Mm^{-1} (659 nm) for 1 second averages [24]. Some of the higher sensitivity could be attributed to the higher multipass mirror reflectivity possible in those cells since they are designed for single wavelengths whereas the MultiPAS-IV uses a single set of mirrors for all four wavelengths thereby compromising some performance to achieve single-cell spectral coverage. A more extensive comparison of the detection limits of recent aerosol PAS instruments is given in Table A.1 in Appendix A.

6.3.2 Validation with Nigrosin Particles and a 7-Wavelength Aethalometer

To test the accuracy of the instrument, we measured the absorption of size-selected nigrosin particles. Nigrosin is a strongly absorbing substance comprised of organic dyes and is convenient for use here because it is water-soluble making it possible to aerosolize and forms spherical particles after drying [30]. It has also been used by others to validate PAS [28–30], extinction-scattering [41], and photothermal interferometric [14] instruments. Furthermore, its complex refractive index has been measured recently over the range 300 – 800 nm [42] making it possible to calculate absorption cross sections using Mie theory. Thus, it is possible for us to compare absorption cross sections measured with the MultiPAS-IV to calculated values. To do so, we measured the absorption by particles that had been atomized, dried after passing through two diffusion driers ($\text{RH} < 5\%$), and size selected using a differential mobility analyzer (DMA). We then calculated the absorption cross section as the ratio of the measured absorption and the particle number density as measured with a condensation particle counter (CPC).

In 6.4 we show the measured and calculated absorption cross sections for four particle diameters, 500, 550, 600, and 650 nm. No corrections for doubly-charged particles transmitted by the DMA are necessary since an impactor with a nominal 50% cutpoint of 900 nm was used; additionally, very few particles that large are produced by the atomizer, the output of which was centered at approximately 100 nm. The error bars represent the precision of the CPC measurements added in quadrature to the precision of the PAS signal and the estimated PAS calibration uncertainty (7.6%). The Mie theory calculations were made using the refractive index values reported by Bluvshstein et al. [42] and by assuming that the geometric standard deviation of the particle sizes transmitted by the DMA was 1.05 (though the calculations are fairly insensitive to this value). The good agreement ($< 2\%$ root-mean-square-deviation) confirms the accuracy of the measurements made with the PAS, especially

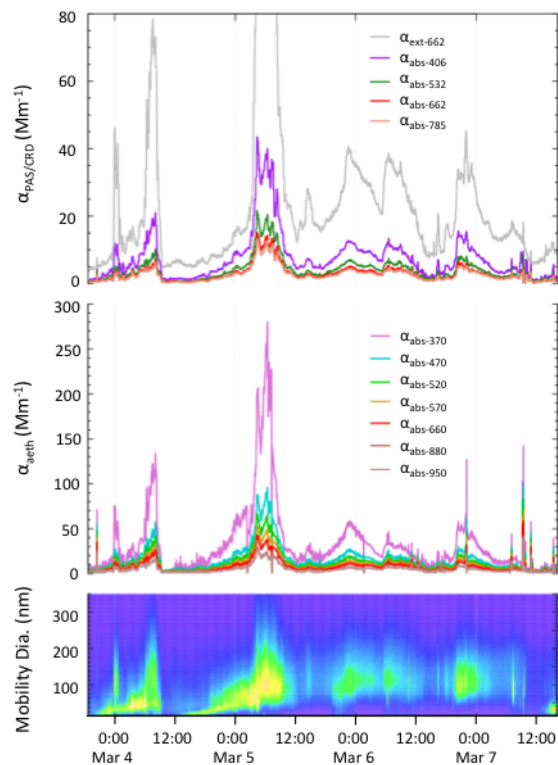


Figure 6.3: Time series of (a) absorption and extinction from the MultiPAS-IV, (b) absorption from the 7-wavelength aethalometer, and (c) size distribution data from the SMPS (grey (color) scale represents particle number density). The PAS/CRD curves represent 10-min rolling averages of 1-s data; each aethalometer curve represents a 10-min rolling average of 1-min data.

considering that uncertainties associated with the DMA and the refractive indices of nigrosin are not included. Additionally, it further validates the proposal put forth by Bluvshstein et al. [42] to use nigrosin particles for PAS calibration; using all four wavelengths, we obtain a calibration constant with nigrosin that is within 1% of the one we obtained using NO_2 (see Figure A.2A). What is more, this nigrosin test confirms the validity of using the calibration obtained with NO_2 at 662 nm for other wavelengths and for particles.

As a further test of the instrument performance, we measured ambient aerosols in Athens, Georgia that had been dried to less than 10% relative humidity using both the MultiPAS-IV and a commercial 7-wavelength aethalometer (Figure 6.3). Over the three-day period, the instruments tracked each other well even though absorption was observed to range by approximately two orders of magnitude. This correlation is better demonstrated in Figure A.3 in which the aethalometer absorption is plotted vs. MultiPAS-IV absorption at the nearest (or interpolated) wavelength with R^2 values ranging from 0.86 to 0.91. Such correlation demonstrates the ability of the MultiPAS-IV to make measurements of aerosol absorption under ambient conditions autonomously. Furthermore, this comparison shows that absorption by trace gas species, such as NO_2 , did not contribute significantly to the PAS measurements since the aethalometer is not susceptible to such interference. Upon closer inspection of Figures 6.3 and A.3, though, it is apparent that the aethalometer systematically overestimates the absorption. Given the good performance of the MultiPAS-IV with nigrosin, this discrepancy is most likely the result of well-known artifacts of filter-based instruments due to multiple scattering effects (see discussion A).

6.3.3 Measuring the Black Carbon AAE of Ambient Aerosols

One of the goals in building the MultiPAS-IV instrument was to allow real-time measurement of aerosol absorption throughout the visible spectrum such that the value of the black carbon absorption Ångström exponent (AAE_{BC}) could be determined and used to derive the C_{Br} contribution. By measuring the absorption at all four wavelengths in the same photoacoustic cell, many potential systematic errors associated with using separate PAS instruments that could affect the spectral shape can be minimized; for example, the cell calibration constant will be the same for all wavelengths and will not factor into calculations of the AAE . Here, we take two approaches to measuring AAE_{BC} : in the first, which we term the “two-wavelength

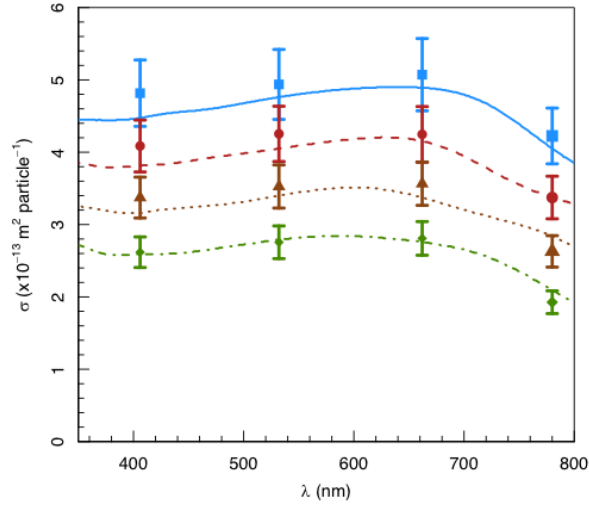


Figure 6.4: Nigrosin aerosol absorption cross sections measured with the MultiPAS-IV for four different selected mobility diameters (500 nm: green diamonds, 550 nm: brown triangles, 660 nm: red circles, 650 nm: blue squares). Curves are Mie theory calculations using the refractive index data of Bluvshstein et al. [42].

approach,” we calculate $\mathring{A}E_{BC}$ from the following equation using the absorption measured at a pair of wavelengths, $\lambda_1 = 662$ nm and $\lambda_2 = 785$ nm:

$$\mathring{A}E_{BC} = \frac{\ln \left[\frac{\alpha_{abs,\lambda_1}}{\alpha_{abs,\lambda_2}} \right]}{\ln \left[\frac{\lambda_2}{\lambda_1} \right]} \quad (6.2)$$

where $\alpha_{abs,\lambda}$ is the absorption at wavelength λ . This approach is equivalent to assuming that all absorption at these two wavelengths is attributed to BC alone.

In the second approach, the “three-wavelength approach,” we use the absorption measured at 532 nm, 662 nm, and 785 nm and perform a non-linear least squares fit to the following equation to derive $\mathring{A}E_{BC}$:

$$\alpha_{abs,\lambda} = \beta \lambda^{-\mathring{A}E_{BC}} \quad (6.3)$$

where β is a scaling factor. This approach has the benefit that it derives $\mathring{A}E_{BC}$ based on three wavelengths instead of two and over a wider spectral range, though it is equivalent to assuming that there is no C_{Br} contribution at any of the three wavelengths. We note that this assumption may not be valid, especially at 532 nm. In both approaches, any data points that do not satisfy the condition $\alpha_{abs,406} > \alpha_{abs,532} > \alpha_{abs,662} > \alpha_{abs,785} > 0 \text{ Mm}^{-1}$ are discarded, which is equivalent to requiring the overall AAE to be greater than zero. This criterion results in 23% of the points being omitted, almost all of which were at low absorption (92% with $\alpha_{abs,785} < 2 \text{ Mm}^{-1}$).

In the two-wavelength approach, we find that the median value of $\mathring{A}E_{BC}$ is 0.70 (± 0.38) with an interquartile range (IQR, 25th percentile to 75th percentile) of 0.41 - 1.10 (see Figure 6.5a). The error bars represent the uncertainty on the ratio of absorption at 662 nm and 785 nm propagated through Equation 6.2; the largest source of error originates from the power meter used to calibrate the photodiode (5%) at each wavelength. The median $\mathring{A}E_{BC}$ value is low compared to the commonly assumed value of 1.0 [43], but it is still within the range of possible values especially considering that the particles may be coated [44–46]. What is more, Wang et al. [47] found that 60% of $\mathring{A}E$ values calculated from the 675 / 880 nm pair from the worldwide Aerosol Robotic Network (AERONET) were < 1 . By way of comparison, the $\mathring{A}E_{BC}$ values calculated from the aethalometer measurements are 0.73 using the 880nm / 950 nm pair and 1.40 using the 660 nm / 880 nm pair (see Figure A.4). The value of $\mathring{A}E_{BC}$ can also be seen in Figure 6.5a to vary quite a bit, which is

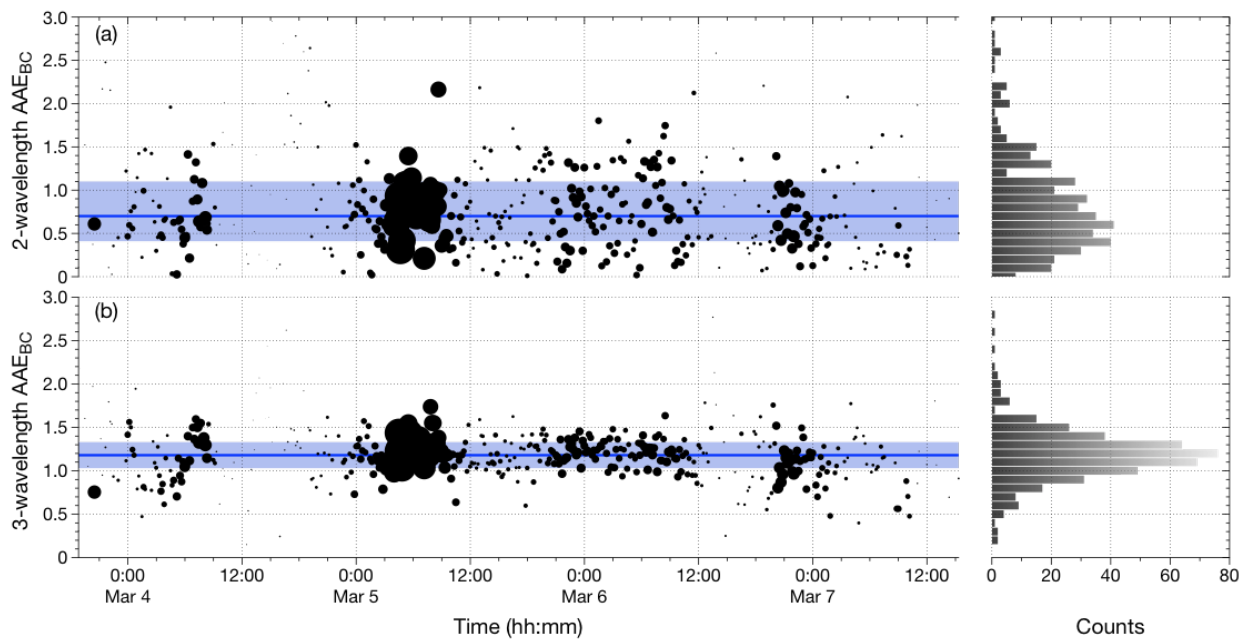


Figure 6.5: Time series and histogram of AAE_{BC} values calculated using the absorbance values at: (a) 662 nm and 785 nm or (b) 532 nm, 662 nm, and 785 nm. Points are sized in relation to the magnitude of absorption at 785 nm. The median values of AAE_{BC} (0.70 and 1.18, respectively) are represented by the blue lines, and the interquartile ranges are represented by the light blue shaded regions.

probably more indicative of the high degree of sensitivity of $\mathring{A}E_{BC}$ to small changes in absorbance values than of true changes in the value of $\mathring{A}E_{BC}$. For example, the absorbance at 662 nm relative to that at 785 nm only needs to change by 5% to cause the $\mathring{A}E_{BC}$ to increase from 0.70 to 1.0.

With the three-wavelength approach, the median $\mathring{A}E_{BC}$ is 1.18 (IQR = 1.03 - 1.33) (Figure 6.5b). We do not report an uncertainty on this value because propagation of uncertainty through the non-linear least squares power law fit to the three measured absorption values at each time point is not straightforward. However, the much smaller spread in values compared to the two-wavelength approach suggests that the inclusion of a third measurement (at 532 nm) improves the quality of the spectral fit, though it does so at the expense of assuming that all absorption at 532 nm is attributed to BC. Such an assumption is probably not warranted since numerous studies have found that C_{Br} can also absorb at this wavelength; for example, offline measurements of solvent-extracted (i.e. not BC) particulate matter demonstrate absorption to at least 600 nm [3, 48–50]. Likewise, some laboratory-generated C_{Br} have been found to absorb at 532 nm and beyond (e.g. Shapiro et al. [51] and Romonosky et al. [52]). For this reason, the $\mathring{A}E_{BC}$ values derived with this approach probably represent an upper limit, and the true value of $\mathring{A}E_{BC}$ probably lies somewhere between 0.70 and 1.18 as measured with the two approaches.

While a smaller degree of scatter would be desirable, we point out that this is the first PAS instrument to measure $\mathring{A}E_{BC}$ at low ambient absorbance values. To put this into context, 36% of the samples had a 785 nm absorbance of less than 2 Mm^{-1} , which is equivalent to a BC loading of less than $0.4 \mu\text{g m}^{-3}$ (assuming a mass absorption cross section of $5.25 \text{ m}^2 \text{ g}^{-1}$). With such small absorbance and the high degree of sensitivity of $\mathring{A}E_{BC}$ to the relative absorption at 662 nm and 785 nm, it is not surprising that such a spread is observed. Interestingly, the median calculated $\mathring{A}E_{BC}$ values and variances are independent of the magnitude of 785 nm absorption when it is greater than 2 Mm^{-1} (Figure A.5), indicating

that our ability to measure $\mathring{A}E_{BC}$ is not limited by the magnitude of absorption above this value.

6.3.4 Measuring Brown Carbon Absorption of Ambient Aerosols

At UV and near-UV wavelengths, aerosol absorption likely comprises contributions from both BC and C_{Br} components. The ability to measure $\mathring{A}E_{BC}$ in real time with the two-wavelength approach allows us to also estimate the C_{Br} contribution at 406 nm and 532 nm:

$$\alpha_{C_{Br},\lambda} = \alpha_{abs,\lambda} - \alpha_{BC,\lambda} - \alpha_{abs,785} \left(\frac{\lambda}{785} \right)^{-\mathring{A}E_{BC}} \quad (6.4)$$

where $\alpha_{C_{Br},\lambda}$ is the calculated absorption attributed to C_{Br} at wavelength (406 nm or 532 nm). With this approach, we do not assume a value of $\mathring{A}E_{BC}$ to extrapolate the BC contribution to 406 nm and 532 nm from longer wavelengths. Instead, we use the value of $\mathring{A}E_{BC}$ measured with the PAS at each time point (from Equation 6.2), which gives us a direct measure of the wavelength dependence of the BC aerosol absorption. This approach would not be possible without having the two wavelengths (red and near-IR) that can be attributed solely to BC, and as such this instrument is the only aerosol PAS that we are aware of that can measure $\mathring{A}E_{BC}$ of suspended aerosols. Importantly, then, this value includes any effects of coatings or morphology [45], which could confound the attribution of C_{Br} absorption if not accounted for correctly, as Lack and Langridge have demonstrated [45]. Using this value, we can derive a more representative estimate of the C_{Br} absorption at shorter wavelengths. We point out that this approach assumes that the $\mathring{A}E_{BC}$ is independent of wavelength, a commonly-made assumption [43].

Figure 6.6a shows the derived C_{Br} absorption time series at both 406 nm and 532 nm calculated using Equation 6.4. The C_{Br} absorption is seen to vary greatly, but it generally

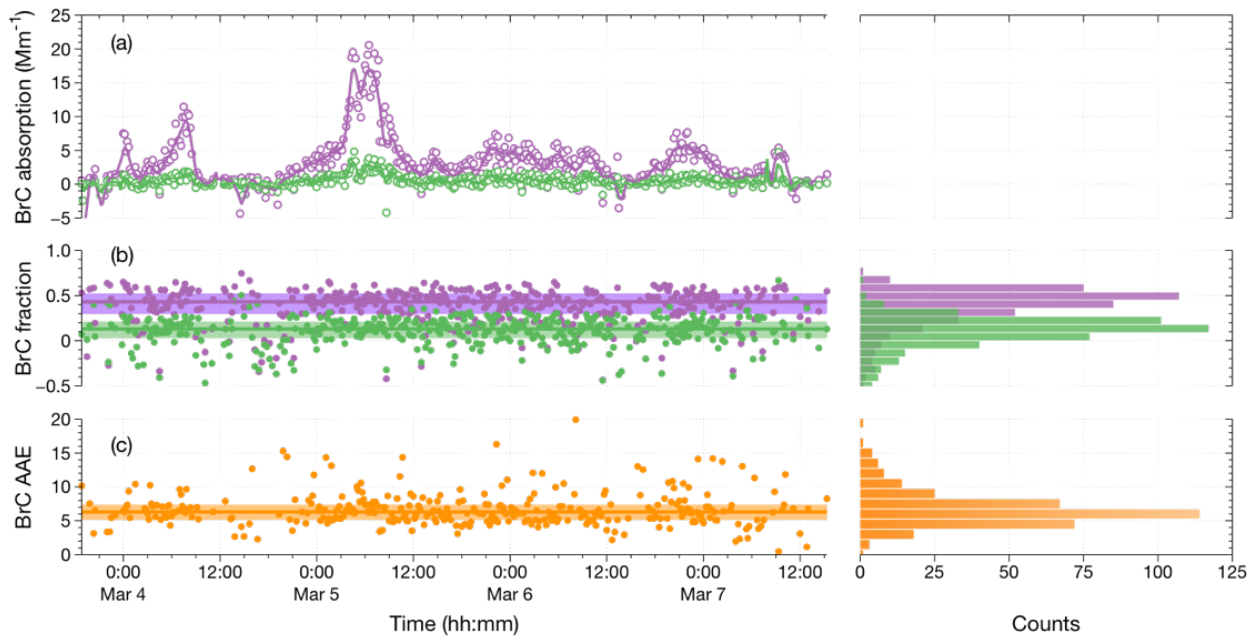


Figure 6.6: C_{Br} as calculated using the two-wavelength approach to calculating \hat{AAE}_{BC} . (a): Time series of calculated C_{Br} absorption at 406 nm (purple open circles) and 532 nm (green open circles); (b): time series and histograms of fraction of absorption due to C_{Br} at 406 nm (purple closed circles) and 532 nm (green closed circles); (c): time series and histogram of C_{Br} \hat{AAE} (orange circles). Horizontal lines represent median values while shaded regions represent interquartile ranges.

correlates with the overall absorption time series (Figure 6.3). The percentage absorption due to C_{Br} at both wavelengths is shown in Figure 6.6b, and despite the considerable variability they remain fairly constant about the median values of 43% (IQR = 30% - 52%) for 406 nm and 13% (IQR = 3% - 21%) for 532 nm. The scatter observed is a function of both the small absorbance being measured and the scatter in the calculated $A\hat{A}E_{BC}$ values (Figure 6.5a) used to calculate the C_{Br} absorption. However, the calculated C_{Br} percentages are more or less the same across the range of absorbance measured, especially when $\alpha_{abs,785} > 2 \text{ Mm}^{-1}$ (see Figure A.5). It is apparent that there is no significant trend in the C_{Br} percentages with time suggesting that the relative contributions of C_{Br} and BC in the aerosols did not change much over the study.

It is also possible to derive C_{Br} absorption using the $A\hat{A}E_{BC}$ calculated with the three-wavelength (532 nm / 662 nm / 785 nm) approach (Figure A.6). In this case, Equation 6.4 is modified slightly to extrapolate the BC component from the average of the absorption measured at 662 nm and 785 nm:

$$\alpha_{C_{Br},\lambda} = \alpha_{abs,\lambda} - \frac{(\alpha_{abs,662} + \alpha_{abs,785})}{2} \left(\frac{\lambda}{723.5} \right)^{-A\hat{A}E_{BC}} \quad (6.5)$$

Taking advantage of having two wavelengths at which the absorption is dominated by BC. The larger $A\hat{A}E_{BC}$ values (median = 1.18, IQR = 1.03 - 1.33) with this approach result in smaller C_{Br} absorption with a median C_{Br} absorption at 406 nm of 26% (IQR = 20% - 31%). Of course, since the 532 nm absorption is assumed to originate solely from the BC with this approach, there is on average no C_{Br} absorption at this wavelength. Alternatively, we can assume $A\hat{A}E_{BC} = 1.0$, as is commonly done when no concurrent measurements of the BC wavelength dependence are available, and use Equation 6.5 to derive the C_{Br} contributions at 406 nm (33%, IQR = 27% - 36%) and 532 nm (6%, IQR = 2% - 10%) (Figure A.6).

6.3.5 Measuring the AAE of Brown Carbon in Ambient Aerosols

The ability to calculate the C_{Br} contribution to aerosol absorption at both 406 nm and 532 nm using the two-wavelength approach to calculate the AAE_{BC} also makes it possible to calculate the $AAE_{C_{Br}}$ using Equation 6.2 (with AAE_{BC} replaced by $AAE_{C_{Br}}$). We point out that this capability is unique to this PAS with its four wavelengths, two in the red/near-IR for determining AAE_{BC} and two in the blue/green for determining $AAE_{C_{Br}}$. The time series of the $AAE_{C_{Br}}$ is shown in Figure 6.6c in which only the time points for which C_{Br} absorption is greater than 0 Mm^{-1} for both 406 nm and 532 nm have been used; this includes 79% of the time points. The median $AAE_{C_{Br}}$ is $6.3 (\pm 0.9)$ (IQR = 5.1 - 7.4) with no apparent trend with time over the course of the study. Here, the uncertainty on $AAE_{C_{Br}}$ is propagated from the uncertainty on AAE_{BC} (used to derive the C_{Br} contribution), for which the largest source of error originates from the power meter used to calibrate the photodiode. The corresponding uncertainty on AAE_{BC} is ± 0.38 , though interestingly, its impact on $AAE_{C_{Br}}$ is mitigated by the fact that it propagates in the same direction for both the 406 nm and 532 nm C_{Br} calculations; thus, the uncertainty partially cancels.

The $AAE_{C_{Br}}$ values measured in this study are similar to $AAEs$ we measured for water- (6.1 ± 0.7) and methanol-soluble (6.7 ± 1.1) filter-collected samples in Athens, Georgia [53] as well as values reported by others. For example, Weber and co-workers report $AAEs$ of 6–8 and 4–6 for water- and methanol soluble particulate matter, respectively, collected in Atlanta, Georgia [48, 54], 6.82 ± 2.63 (water-soluble) and 4.54 ± 3.07 (methanol-soluble) in the Central U.S. [46], and 7.28 ± 0.24 (water-soluble) and 7.10 ± 0.45 (methanol-soluble) in Beijing, China [55]. Likewise, Hoffer et al. [56] measured average water-soluble $AAEs$ of 6.4 and 6.8 for daytime and nighttime samples in Brazil, respectively, and Kim et al. [57] measured average $AAEs$ of 7.23 ± 1.58 (water-soluble) and 5.05 ± 0.67 (methanol-soluble) in Seoul, Korea.

As with the AAE_{BC} values and the 406 nm and 532 nm C_{Br} absorption values, there appears to be no correlation between the $\text{AAE}_{C_{Br}}$ and the magnitude of absorption at 785 nm (see Figure A.6). This observation suggests that the spectral shape of the C_{Br} was not a function of aerosol loading. Furthermore, the spread of $\text{AAE}_{C_{Br}}$ values was relatively independent of absorption demonstrating no improvement for $\alpha_{abs,785}$ values above 2 Mm^{-1} , which indicates that the ability to derive the $\text{AAE}_{C_{Br}}$ values is not limited by the instrument's sensitivity except perhaps at the lowest absorbance values.

6.4 Conclusions and Outlook

We have created a 4-wavelength photoacoustic spectrometer capable of measuring ambient aerosol absorption, which to the best of our knowledge is the first such multi-wavelength, multipass, single-cell PAS. The instrument is compact, robust, and portable, such that it may easily be deployed in field and laboratory campaigns and demonstrates good correlation with a 7-wavelength aethalometer. The instrument makes several improvements upon existing instrumentation, including:

1. making possible the calculation of both AAE_{BC} and $\text{AAE}_{C_{Br}}$ directly from the absorption measurements,
2. employing a single cell for all wavelengths thereby removing cell-to-cell calibration uncertainties and improving the accuracy of AAE calculations,
3. and achieving sub- Mm^{-1} detection limits for four wavelengths spanning the UV-visible spectrum in a portable instrument free from filter artifacts.

We believe this instrument will allow more accurate measurement of the AAE and thereby reduce uncertainty on aerosol absorption and further allow better differentiation between BC and C_{Br} . Future efforts will focus on expanding spectral coverage into the UV to improve this differentiation even more.

References

- (1) Stocker, T.; Qin, D.; Plattner, G.; Tignor, M.; Allen, S.; Boschung, J.; Nauels, A.; Xia, Y.; Bex, V.; Midgley, P. *The Physical Science Basis* **2013**.
- (2) Bond, T. C. et al. *Journal of Geophysical Research: Atmospheres* **2013**, *118*, 5380–5552.
- (3) Kirchstetter, T. W.; Novakov, T.; Hobbs, P. V. *Journal of Geophysical Research: Atmospheres* **2004**, *109*, DOI: 10.1029/2004jd004999.
- (4) Andreae, M.; Gelencser, A. *Atmos. Chem. Phys.* **2006**, *6*, 3131–3148.
- (5) Moosmüller, H.; Chakrabarty, R.; Arnott, W. *Journal of Quantitative Spectroscopy and Radiative Transfer* **2009**, *110*, 844–878.
- (6) Weingartner, E.; Saathoff, H.; Schnaiter, M.; Streit, N.; Bitnar, B.; Baltensperger, U. *Journal of Aerosol Science* **2003**, *34*, 1445–1463.
- (7) Lack, D. A.; Cappa, C. D.; Covert, D. S.; Baynard, T.; Massoli, P.; Sierau, B.; Bates, T. S.; Quinn, P. K.; Lovejoy, E. R.; Ravishankara, A. R. *Aerosol Science and Technology* **2008**, *42*, 1033–1041.
- (8) Drinovec, L.; Močnik, G.; Zotter, P.; Prévôt, A. S. H.; Ruckstuhl, C.; Coz, E.; Rupakheti, M.; Sciare, J.; Müller, T.; Wiedensohler, A.; Hansen, A. D. A. *Atmospheric Measurement Techniques* **2015**, *8*, 1965–1979.
- (9) Petzold, A.; Schönlinner, M. *Journal of Aerosol Science* **2004**, *35*, 421–441.
- (10) Singh, S.; Fiddler, M. N.; Smith, D.; Bililign, S. *Aerosol Science and Technology* **2014**, *48*, 1345–1359.
- (11) Onasch, T. B.; Massoli, P.; Keabian, P. L.; Hills, F. B.; Bacon, F. W.; Freedman, A. *Aerosol Science and Technology* **2015**, *49*, 267–279.

- (12) Lin, H.-B.; Campillo, A. J. *Applied Optics* **1985**, *24*, 422.
- (13) Moosmüller, H.; Arnott, W.; Rogers, C. *Journal of the Air & Waste Management Association* **1997**, *47*, 157–166.
- (14) Sedlacek, A.; Lee, J. *Aerosol Science and Technology* **2007**, *41*, 1089–1101.
- (15) Bell, A. G. *Science* **1881**, *os-2*, 242–253.
- (16) Miklós, A.; Hess, P.; Bozóki, Z. *Review of scientific instruments* **2001**, *72*, 1937–1955.
- (17) Truex, T.; Anderson, J. *Atmospheric Environment (1967)* **1979**, *13*, 507–509.
- (18) Petzold, A.; Niessner, R. *Applied Physics Letters* **1995**, *66*, 1285–1287.
- (19) Arnott, W. P.; Walker, J. W.; Moosmüller, H.; Elleman, R. A.; Jonsson, H. H.; Buzorius, G.; Conant, W. C.; Flagan, R. C.; Seinfeld, J. H. *Journal of Geophysical Research* **2006**, *111*, DOI: 10.1029/2005jd005964.
- (20) Lack, D. A.; Lovejoy, E. R.; Baynard, T.; Pettersson, A.; Ravishankara, A. *Aerosol Science and Technology* **2006**, *40*, 697–708.
- (21) Lewis, K.; Arnott, W. P.; Moosmüller, H.; Wold, C. E. *Journal of Geophysical Research* **2008**, *113*, DOI: 10.1029/2007jd009699.
- (22) Ajtai, T.; Filep, Á.; Schnaiter, M.; Linke, C.; Vragel, M.; Bozóki, Z.; Szabó, G.; Leisner, T. *Journal of Aerosol Science* **2010**, *41*, 1020–1029.
- (23) Ajtai, T.; Filep, Á.; Utry, N.; Schnaiter, M.; Linke, C.; Bozóki, Z.; Szabó, G.; Leisner, T. *Journal of Aerosol Science* **2011**, *42*, 859–866.
- (24) Lack, D. A.; Richardson, M. S.; Law, D.; Langridge, J. M.; Cappa, C. D.; McLaughlin, R. J.; Murphy, D. M. *Aerosol Science and Technology* **2012**, *46*, 555–568.
- (25) Zhang, X.; Kim, H.; Parworth, C. L.; Young, D. E.; Zhang, Q.; Metcalf, A. R.; Cappa, C. D. *Environmental science & technology* **2016**, *50*, 1681–1690.

- (26) Haisch, C.; Menzenbach, P.; Bladt, H.; Niessner, R. *Analytical Chemistry* **2012**, *84*, 8941–8945.
- (27) Sharma, N.; Arnold, I. J.; Moosmüller, H.; Arnott, W. P.; Mazzoleni, C. *Atmospheric Measurement Techniques* **2013**, *6*, 3501–3513.
- (28) Radney, J. G.; Zangmeister, C. D. *Analytical Chemistry* **2015**, *87*, 7356–7363.
- (29) Wiegand, J. R.; Mathews, L. D.; Smith, G. D. *Analytical Chemistry* **2014**, *86*, 6049–6056.
- (30) Lack, D. A.; Lovejoy, E. R.; Baynard, T.; Pettersson, A.; Ravishankara, A. R. *Aerosol Science and Technology* **2006**, *40*, 697–708.
- (31) Linke, C.; Ibrahim, I.; Schleicher, N.; Hitzenberger, R.; Andreae, M. O.; Leisner, T.; Schnaiter, M. *Atmospheric Measurement Techniques* **2016**, *9*, 5331–5346.
- (32) Arnott, W. P.; Moosmüller, H.; Rogers, C. F.; Jin, T.; Bruch, R. *Atmospheric Environment* **1999**, *33*, 2845–2852.
- (33) Brown, S. S. *Chemical Reviews* **2003**, *103*, 5219–5238.
- (34) Berden, G.; Engeln, R., *Cavity Ring-Down Spectroscopy: Techniques and Applications*; Wiley: 2009.
- (35) Silver, J. A. *Applied Optics* **2005**, *44*, 6545–6556.
- (36) Mazurenka, M.; Wada, R.; Shillings, A. J. L.; Butler, T. J. A.; Beames, J. M.; Orr-Ewing, A. J. *Applied Physics B* **2005**, *81*, 135–141.
- (37) Everest, M. A.; Atkinson, D. B. *Review of Scientific Instruments* **2008**, *79*, 023108.
- (38) Bostrom, G.; Atkinson, D.; Rice, A. *Review of Scientific Instruments* **2015**, *86*, 043106.
- (39) Allan, D. *Proceedings of the IEEE* **1966**, *54*, 221–230.
- (40) Nakayama, T.; Suzuki, H.; Kagamitani, S.; Ikeda, Y.; Uchiyama, A.; Matsumi, Y. *Journal of the Meteorological Society of Japan. Ser. II* **2015**, *93*, 285–308.

- (41) Dial, K. D.; Hiemstra, S.; Thompson, J. E. *Analytical Chemistry* **2010**, *82*, 7885–7896.
- (42) Bluvshstein, N.; Flores, J. M.; He, Q.; Segre, E.; Segev, L.; Hong, N.; Donohue, A.; Hilfiker, J. N.; Rudich, Y. *Atmospheric Measurement Techniques* **2017**, *10*, 1203–1213.
- (43) Bond, T. C.; Bergstrom, R. W. *Aerosol Science and Technology* **2006**, *40*, 27–67.
- (44) Gyawali, M.; Arnott, W. P.; Lewis, K.; Moosmüller, H. *Atmospheric Chemistry and Physics* **2009**, *9*, 8007–8015.
- (45) Lack, D. A.; Cappa, C. D. *Atmospheric Chemistry and Physics* **2010**, *10*, 4207–4220.
- (46) Liu, D.; Taylor, J. W.; Young, D. E.; Flynn, M. J.; Coe, H.; Allan, J. D. *Geophysical Research Letters* **2015**, *42*, 613–619.
- (47) Wang, X.; Heald, C. L.; Sedlacek, A. J.; de Sá, S. S.; Martin, S. T.; Alexander, M. L.; Watson, T. B.; Aiken, A. C.; Springston, S. R.; Artaxo, P. *Atmospheric Chemistry and Physics* **2016**, *16*, 12733–12752.
- (48) Hecobian, A.; Zhang, X.; Zheng, M.; Frank, N.; Edgerton, E. S.; Weber, R. J. *Atmospheric Chemistry and Physics* **2010**, *10*, 5965–5977.
- (49) Zhang, X.; Lin, Y.-H.; Surratt, J. D.; Weber, R. J. *Environmental Science & Technology* **2013**, *47*, 3685–3693.
- (50) Phillips, S. M.; Smith, G. D. *Aerosol Science and Technology* **2017**, *51*, 1113–1121.
- (51) Shapiro, E. L.; Szprengiel, J.; Sareen, N.; Jen, C. N.; Giordano, M. R.; McNeill, V. F. *Atmospheric Chemistry and Physics* **2009**, *9*, 2289–2300.
- (52) Romonosky, D. E.; Ali, N. N.; Saiduddin, M. N.; Wu, M.; Lee, H. J. (; Aiona, P. K.; Nizkorodov, S. A. *Atmospheric Environment* **2016**, *130*, 172–179.
- (53) Phillips, S. M.; Smith, G. D. *Aerosol Science and Technology* **2017**, *51*, 1113–1121.

- (54) Liu, J.; Bergin, M.; Guo, H.; King, L.; Kotra, N.; Edgerton, E.; Weber, R. J. *Atmospheric Chemistry and Physics* **2013**, *13*, 12389–12404.
- (55) Cheng, Y.; He, K.-b.; Du, Z.-y.; Engling, G.; Liu, J.-m.; Ma, Y.-l.; Zheng, M.; Weber, R. J. *Atmospheric Environment* **2016**, *127*, 355–364.
- (56) Hoffer, A.; Gelencsér, A.; Guyon, P.; Kiss, G.; Schmid, O.; Frank, G. P.; Artaxo, P.; Andreae, M. O. *Atmospheric Chemistry and Physics* **2006**, *6*, 3563–3570.
- (57) Kim, H.; Kim, J. Y.; Jin, H. C.; Lee, J. Y.; Lee, S. P. *Atmospheric Environment* **2016**, *129*, 234–242.

CHAPTER 7

CAN OZONE BE USED TO CALIBRATE AEROSOL PHOTOACOUSTIC SPECTROMETERS?¹

¹ Fischer, D.A. and G.D. Smith. 2018. To be submitted to *Atmospheric Measurement Techniques*.

7.1 Introduction

Photoacoustic spectroscopy (PAS) has become a popular technique for measuring absorption of light by atmospheric aerosols (e.g. [1–8], among others). It is a desirable method because it has low detection limits, is capable of measuring suspended aerosols, and is insensitive to scattering. However, PAS requires rigorous calibration for accurate absorption measurements, and this calibration becomes more difficult as the complexity of the PAS increases (e.g. with a multipass enhancement cell and/or multiple wavelengths). Although ozone has been used as a calibrant for PAS [9, 10], recent works exploring its validity have contradicted each other. Bluvshstein et al. [11] saw a discrepancy between ozone calibrations and particle-based calibrations, while Davies et al. [12] found ozone to be in agreement with particle-based measurements. Concurrent to these publications, we have been exploring the use of ozone as a PAS calibrant for multipass, multi-wavelength, aerosol photoacoustic spectrometers; our observations will be presented here to add to the discussion on the topic.

The underlying principle of PAS is that light absorbed by the sample is converted to heat via thermal relaxation. When the light is modulated on and off at acoustic frequencies, this produces a pressure wave detectable by a standard microphone. [13] However, for quantitative measurements, this requires that no non-thermal relaxation pathways exist (e.g. photodissociation), as any energy given up non-thermally does not contribute to the PAS signal. Further, for trace gases in a bath gas, the excited analyte molecule must efficiently transfer its energy to the bath gas, and the bath gas must relax more quickly than the modulation frequency of the PAS. For accurate PAS measurements, the sound intensity (volume) measured with the microphone must be calibrated to units of absorption. For consistency, we will refer to this value as the sensitivity factor, m with units of V Mm W^{-1} :

$$m = \frac{s}{b_{abs}} \tag{7.1}$$

where s is the power-normalized PAS signal (i.e. in units of VW^{-1}) and b_{abs} is the corresponding known absorption due to a calibrant (in units of Mm^{-1}). Most commonly, this is either determined by filling the sample cell with a gas of known concentration (N) and absorption cross section (σ) (such that $b_{abs} = N\sigma$) or measuring the absorption with another technique such as cavity ringdown spectroscopy. By using multiple concentrations (or sizes, in the case of aerosols), a linear regression of s vs. b_{abs} can be performed to determine m . Examples of calibrants include aerosol particles such as flame-generated soot [14] and gas-phase absorbers such as ozone [9, 10] or nitrogen dioxide [5, 14, 15]. Although ozone absorbs weakly in the near-UV and violet regions of the spectrum and is difficult to measure there, it has been employed for field calibrations because it can be easily generated using a UV lamp or corona discharge.

As noted above, Bluvshstein et al. [11] conducted a systematic study of calibrants for a multipass photoacoustic spectrometer. They measured light absorbing aerosols, including nigrosin, Suwannee River fulvic acid, and Pahokee peat fulvic acid. They then used an independently measured refractive index and Mie theory to calculate the known absorption for each sample and found generally good agreement between their sensitivity factors; however, when they performed a calibration with ozone, they found a much lower sensitivity factor (by roughly 50%). Alternatively, Davies et al. [12] found their measured nigrosin absorption cross sections agreed well with Mie theory when they calibrated their PAS with ozone prior to nigrosin measurements.

Clearly, there are contradictory results regarding the use of ozone as a calibrant for photoacoustic spectroscopy, and additional inquiry into the subject is warranted. Not discussed in either of the studies is a reason for the observed results. We note that ozone is well-known to photodissociate up to roughly 1120 nm, suggesting that PAS calibrations using ozone may be subject to non-thermal relaxation. This could potentially explain discrepancies between ozone calibrations and other methods. [16] In this communication, we attempt to provide

some insight toward a more thorough understanding of this topic. Specifically, we compare calibrations with (1) NO₂, (2) nigrosin aerosols, and (3) ozone under various conditions. We show agreement between NO₂ and nigrosin, but not ozone. We observed a much lower sensitivity with ozone calibrations. We further show direct evidence for photodissociation of ozone inside the PAS when exposed to a 532 nm continuous wave laser and observed that adding small amounts (<5%) oxygen to the sample line changed the calibration slope significantly to bring it more in line with the other methods. We propose that the latter effects can be explained by a simple kinetic model in which oxygen and nitrogen compete to deactivate “hot” ozone, and that oxygen completes this process more efficiently than nitrogen.

7.2 Materials and Methods

7.2.1 Photoacoustic Spectrometer

The photoacoustic spectrometer used in this study has been previously described elsewhere. [17] Briefly, it is a single-cell, four-wavelength, diode laser PAS. Four diode lasers (406, 532, 662, and 780 nm) are combined into a single beam with dichroic mirrors and turned into a multipass cell consisting of two highly reflective, cylindrical mirrors ($R > 99\%$); the front mirror has a 2 mm entrance hole drilled in the center. [18] The PAS cell itself sits within the multipass cell and follows the design of Lack et al. [9]. A calibrated photodiode behind the rear multipass mirror is used to monitor the power of each laser simultaneously. The system includes a cavity ringdown cell (CRD) operating at 662 nm (from the same 662 nm laser employed by the PAS) for direct calibration of the PAS. The four lasers in the PAS are operated simultaneously at frequencies spaced every 2 Hz around the resonant frequency of the cell. A fast-Fourier transform (FFT) is performed on the microphone signal to deconvolve the signals at each wavelength. The resonant frequency of the PAS is measured by scanning the laser frequency across the resonant peak of the cell and finding the best fit to the

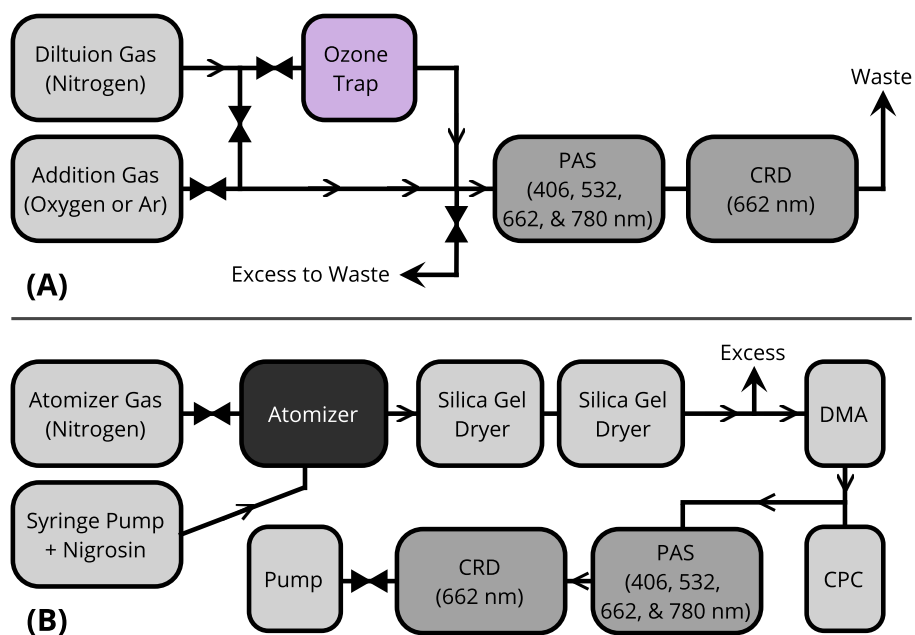


Figure 7.1: Block diagram of the experimental setup. (A) Setup used for O₃ measurements, and (B) setup used for nigrosin measurements. Triangles indicate needle valves or critical orifices; arrows indicate direction of flow. CPC = condensation particle counter; DMA = differential mobility analyzer; CRD = cavity ringdown spectrometer.

frequency sweep data. A frequency sweep was conducted prior to each set of measurements, and anytime the gas type was changed. The lasers can be individually switched from digital modulation (as is used for PAS) to continuous wave mode, which is helpful in conducting photolysis studies. A diagram of the instrument can be found in Figure 6.1 or Fischer and Smith [17].

7.2.2 NO₂ Measurements

Following our typical procedure, as described in Fischer and Smith [17], we calibrated the PAS with nitrogen dioxide. A standard 10.29 ppm ($\pm 5\%$) mixture of NO₂ in N₂ and O₂ for stability (Airgas, Athens, Georgia) was diluted to various concentration into N₂ boil off from a liquid nitrogen dewar (Airgas, Athens, Georgia). A rotameter was used to monitor the flow of NO₂ while the N₂ flow was controlled with a needle valve and monitored with a flow meter (TSI, Shoreview, Minnesota). NO₂ was introduced first to the PAS cell and then transported to the CRD via a short length of copper tubing. The outlet of the CRD was plugged and the gas was directed out of the purge inlets to avoid dead volume in the cell (no purge flow was used for NO₂ measurements). CRD and PAS measurements were conducted simultaneously at 662 nm, and all other laser wavelengths were turned off during NO₂ measurements.

7.2.3 Ozone Measurements

Ozone was generated using a commercial corona discharge ozone generator (Pacific Ozone, Benicia, California). The ozone was trapped on silica gel in a glass trap held in slurry of solid CO₂ and ethanol. Prior to trapping, the silica gel and trap were heated to 100° C while being held under vacuum for at least 1 hour to remove contaminants. As with NO₂, no purge flow was used during O₃ measurements and the sample was introduced to the PAS first and transported to the CRD via a short length of copper tubing. The outlet of

the CRD was plugged and the sample was directed out of the purge flow lines to minimize dead volume inside the cell. Figure 7.1A shows a block diagram of the setup used for ozone measurements. Mass flow controllers were used to control the ratio of oxygen to nitrogen (MKS Instruments).

7.2.4 Nigrosin Measurements

Figure 7.1B shows a block diagram of the setup used for nigrosin measurements. Nigrosin aerosol was generated using a constant output atomizer (TSI 3076) with an aqueous solution of nigrosin (4 g L^{-1} , Sigma Aldrich, CAS# 8005-03-6) and dried using a series of two silica-gel diffusion dryers. The relative humidity was kept below 5% and monitored with an inline relative humidity probe (HMP110, Vaisala Corporation, Helsinki, Finland). Atomized, dried particles were size selected at 500, 500, 600, and 650 nm using an electrostatic classifier (TSI 3080) and differential mobility analyzer with a 10:1 sheath flow to sample flow ratio (DMA, TSI 3085). Monodisperse aerosols were split in parallel to a condensation particle counter (CPC, TSI 3775) and the photoacoustic cell. They were delivered to each instrument using conductive silicone tubing. After particles passed through the PAS, they entered the CRD cell, which had a purge flow of 60 SCCM N_2 (maintained by a critical orifice) over each mirror to prevent particle deposition. The aerosol sample was pulled through the instrument with a small diaphragm pump (KNF Neuberger, Inc., Trenton, NJ) and the flow rate was maintained at 330 SCCM total flow with a critical orifice (Lenox Laser, Glen Arm, Maryland). All lasers were operated simultaneously. The refractive index from Bluvshstein et al. [11] was used to calculate nigrosin absorption cross sections using Mie theory assuming a geometric standard deviation of 1.05. Mie theory calculations were performed in MATLAB.

7.3 Results

We chose to take an alternative approach to calibrating with ozone compared to prior studies. [11, 12] Instead of using the flow directly out of an ozone generator, we trapped ozone on a silica gel trap prior to analysis. This allows us to achieve lower overall oxygen concentrations than available with an O_3 generator and more fully map out the behavior of ozone in response to oxygen. Further, while others have used single-wavelength PASs in parallel, we used a 4-wavelength, single-cell PAS. This gave us the opportunity to operate some lasers in continuous-wave mode and probe for signal loss due to photodissociation. The results presented here will be discussed first in terms of our typical calibrant (NO_2) and a particle-based calibration (nigrosin). We will then discuss the use of ozone in relation to those calibrants and finally end with a discussion of oxygen's effect on ozone signals in the PAS.

7.3.1 Non-ozone Methods of Calibration

We prefer to calibrate with NO_2 by measuring the PAS signal at 662 nm and comparing to the absorption measured by the CRD at 662 nm. Because each of the instruments is illuminated by the same laser, the error is dependent only on the error of the CRD and the precision of the PAS; all errors associated with flow measurement and comparison of absorption cross sections become irrelevant. Further, because all of our wavelengths are contained in a single cell, the power-normalized calibration at 662 nm can be applied to all wavelengths (including 406 nm, where NO_2 photodissociates). [7, 17] This, however, adds some additional error from the measurement of the effective power of each wavelength.

Here, we will compare all slopes to our particle based method, nigrosin. Historically our PAS has provided a calibration slope of just over $m = 10 \times 10^{-4} \text{ V Mm W}^{-1}$ with NO_2 . In this work we obtain a slope of $m = 10.7 \times 10^{-4} \text{ V Mm W}^{-1}$ with nigrosin, as expected based

on previous work with NO_2 . Likewise, NO_2 and the CRD provide a slope within 10% of nigrosin at $m = 11.9 \times 10^{-4} \text{ V Mm W}^{-1}$. Because we used a 10 ppm calibrated mixture of NO_2 , we were able to independently determine the concentration of NO_2 for validation of the CRD calibration. Although this “ $N\sigma$ ” calibration has a larger error due to uncertainties in flow measurements, it provided a slope of $m = 11.7 \times 10^{-4} \text{ V Mm W}^{-1}$, which is within 1.5% of the CRD method and still within 10% of the nigrosin method. The calibration curves for these methods can be seen in Figure 7.2A.

7.3.2 Ozone as a Calibrant

We initially began investigating O_3 as a calibrant for use in the field due to its ability to be generated from air with a Hg pen lamp. In doing so, we noticed discrepancies between ozone and NO_2 calibrations. In Figure 7.2, the most dramatic outlier is the dashed grey-green line obtained from ozone in pure N_2 , which yields a slope more than 50% lower than the slope obtained with nigrosin at $m = 5.1 \times 10^{-4} \text{ V Mm W}^{-1}$, and agrees with no other method of calibrating. We hypothesized that this was due to photolysis of ozone under irradiation by visible light via $\text{O}_3 + h\nu (> 1.1\text{eV}) \rightarrow \text{O}_2 + \text{O}(^3\text{P})$. If this were the case, we further hypothesized that diluting ozone with oxygen instead of nitrogen would yield a larger calibration slope because the oxygen would promote recombination of ozone upon dissociation. Indeed, as the dotted teal line in Figure 7.2A indicates, the calibration slope under conditions of 100% O_2 was within 10% of the slope from nigrosin at $m = 9.8 \times 10^{-4} \text{ V Mm W}^{-1}$. Figure 7.2B shows the same data as Figure 7.2A in bar plot form. In this form, it is easier to discern the various methods and it shows more concentrations for the oxygen-added calibrations. The clear outlier here is again the ozone-nitrogen calibration.

To search for evidence of O_3 photolysis, we operated our 532 nm laser in continuous-wave mode. This prevented the laser from contributing the PAS signal and yielded maximum continuous power to search for photodissociation. The PAS signal due to ozone was monitored

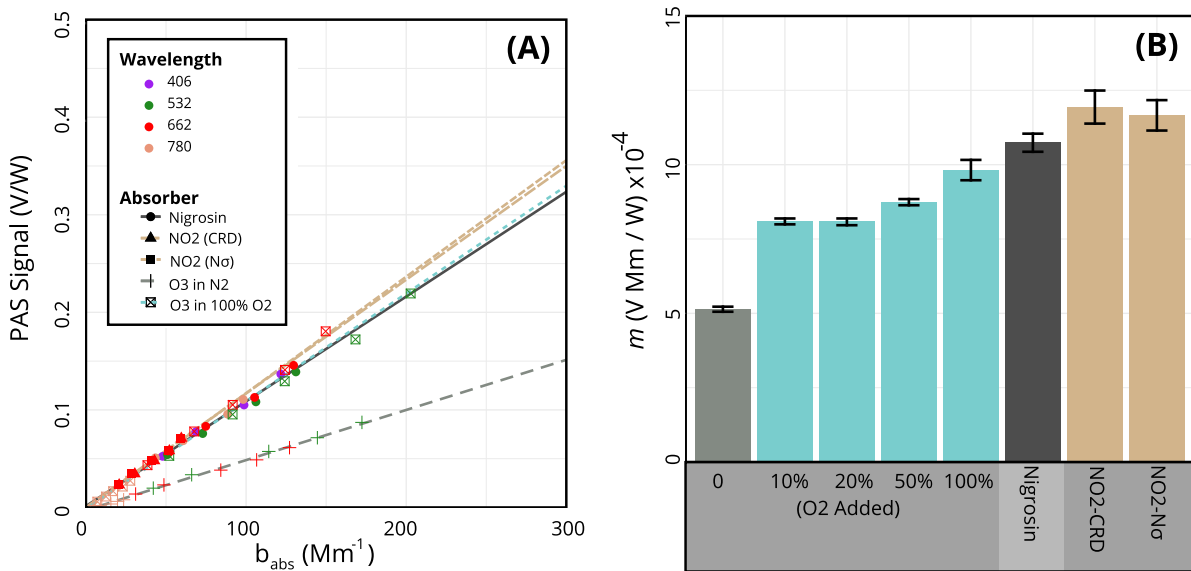


Figure 7.2: Calibrations via various methods. (A) Calibration curves from various methods. Points are colored by wavelength. (B) Barplot of PAS calibration slopes from various methods. Error bars represent the standard error on the slope from the linear regression. The line colors in (A) correspond to the color groups in (B)

with the 662 nm PAS channel and the concentration of ozone was monitored with the cavity ringdown spectrometer. This allowed us to separate effects due to a lowering of the ozone concentration (which would be evident with the CRD) and any additional loss of PAS signal due to energy loss due to breaking chemical bonds. The green shaded regions in Figure 7.3 indicate when the 532 nm laser was turned on to illuminate the ozone inside the PAS. An immediate decrease in both the PAS signal and the ozone concentration measured with the CRD is noticed, further hinting at a loss of signal during the relaxation step. Furthermore, this process was not observed when oxygen was present in the cell at 5% of the total sample flow, as shown in Figure 7.3B. This suggests oxygen must be present for calibrations with ozone, but leads to the question: How much oxygen must be present? For example, others

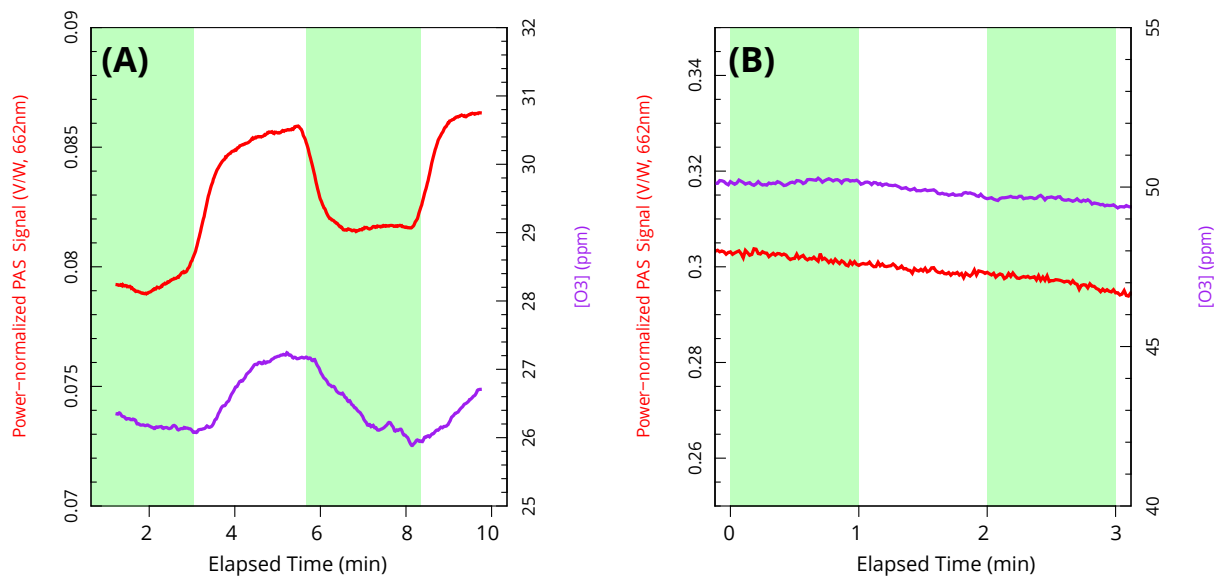


Figure 7.3: Photolysis of ozone in the PAS. (A) Response of PAS signal and [O₃] to irradiation at 532 nm with no oxygen present and (B) with 5% oxygen present. Green shaded regions represent times when the 532 nm laser was turned on, and white regions when it was off.

have calibrated in 10% oxygen, and it may be convenient to calibrate in 20% oxygen (i.e. air).

7.3.3 Effect of Oxygen on Ozone Signal

The effects of oxygen on the PAS signal can be clearly seen Figure 7.4. In Figure 7.4A, oxygen was added to the sample line such that the oxygen made up 5% of the total flow. The red regions indicate when O₂ was added to the sample stream, and the white regions indicate when it was removed. There is a clear difference upon addition or subtraction of O₂ from the sample flow, with it increasing the signal roughly 75%, and a similar trend was observed at all four measurement wavelengths available in our PAS. This cannot be due to changes in the concentration of ozone, which were monitored with the CRD and actually decreased slightly when oxygen was added (due to the slight dilution of the sample

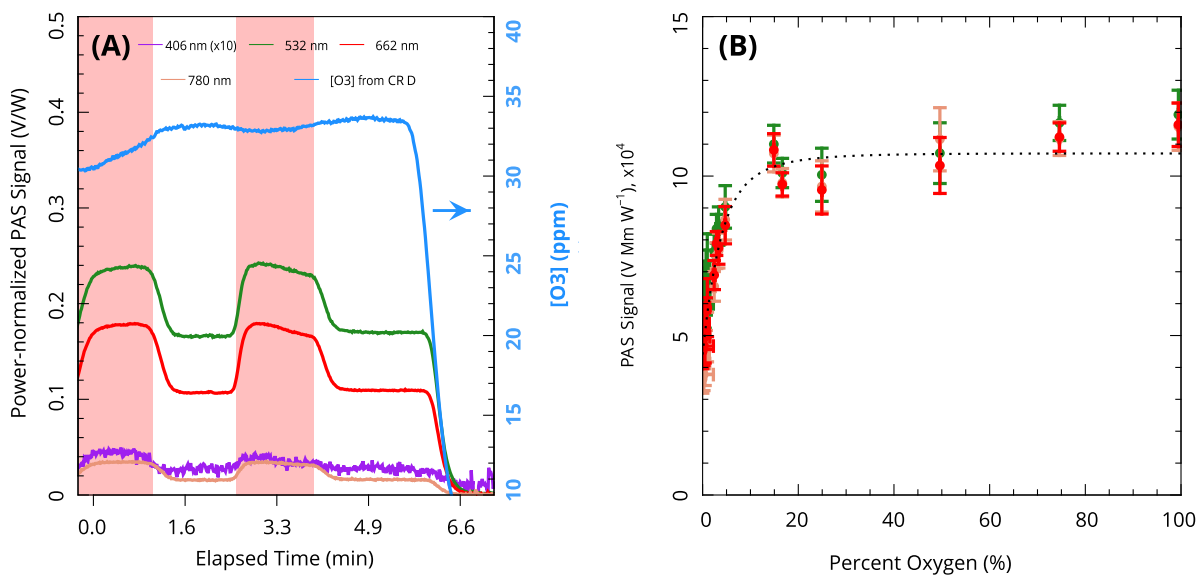


Figure 7.4: Time series of O₂ addition (A) and PAS signal (normalized to absorption cross section) as a function of [O₂] (B). Red shaded regions in (A) represent times when 5% oxygen was added to the sample stream. Error bars in (B) are ± 1 SD of a 30-second average (y) and accuracy specifications of flow meters (x). The large SD in the 406 nm data is due to the near-background absorption at that wavelength.

flow). An alternative explanation would be a shift in the resonant frequency upon addition of oxygen. However, because the resonant frequency was measured in nitrogen, any shift in resonant frequency should only decrease the signal. Further, measurements of the resonant frequency showed negligible differences between nitrogen-diluted samples and 5% oxygen-added samples. Thus, it was not enough to have an appreciable effect on the resonant frequency of our low- Q (wide-bandwidth) PAS cell. We therefore conclude that the observed increase in signal upon addition to oxygen is indeed an effect associated with oxygen, ozone, and nitrogen. Finally, such a phenomenon was not observed when adding argon instead of oxygen (data not shown), implying that the effect is unique to oxygen.

Figure 7.4B shows the effect of adding oxygen in varying amounts from 0–100% of the bath gas. A clear trend is observed in relation to the oxygen concentration at 532, 662, and 780 nm; the effect likely exists at 406 nm as well, but that wavelength was not measured because of ozone’s low absorption cross section at that wavelength. Again, it is clear that oxygen has an effect on the PAS signal, with oxygen causing an increase in the measured PAS sensitivity. This sensitivity starts off at about $4 \times 10^{-4} \text{ V Mm W}^{-1}$ for 0% O_2 , more than a factor of 2 lower than the normal PAS cell sensitivity measured with either NO_2 or nigrosin. The sensitivity increases quickly as oxygen is added up to about 20% oxygen in nitrogen, at which point it begins to asymptotically approach an upper limit that is more in line with the sensitivities measured by other methods. Others have observed similar effects with HCN when adding water vapor into the cell [19] and when adding oxygen into a mixture of NO_2 and N_2 , although in this case adding oxygen caused a decrease in the signal [20].

Explanation of this effect appears to follow a kinetic model. An underlying assumption of PAS is that all the photon energy absorbed by the sample is transferred to the bath gas as thermal energy to create a pressure wave. For trace gases (e.g. O_3) in a bath gas (like N_2), this requires efficient coupling of the analyte’s “hot” state (e.g. O_3^*) into translational, rotational, and/or vibrational modes of the bath gas, and the further relaxation of the bath gas molecule. If the transfer of energy from the analyte to the bath gas is inefficient or the excited state of the bath gas is long-lived with respect to the modulation frequency of the light source, the photon energy will not be efficiently coupled into the microphone, which is observed as a decreased cell sensitivity. The dotted black line in Figure 7.4B represents a fit of the 662 nm data to:

$$m = \frac{m_0}{\sqrt{1 + \left(\frac{A}{1 + \frac{rx}{(1-\chi)}}\right)^2}} \quad (7.2)$$

where m is the cell sensitivity coefficient in V Mm W^{-1} , m_0 is the asymptotic sensitivity coefficient, χ is the oxygen concentration as a fraction of total bath gas (i.e. 0–100%/100), r is ratio of the quenching rate constants for oxygen and nitrogen ($k_{\text{O}_2}/k_{\text{N}_2}$), and:

$$A = 2\pi f\tau_{\text{N}_2} \quad (7.3)$$

where f is the modulation frequency and τ_{N_2} is the deactivation lifetime of pure, dry N_2 . For efficient transfer of the PAS signal to the microphone, the deactivation lifetime must be significantly faster than the modulation frequency, meaning A must be $\ll 1$. The data here give $A = 2.20$, and the experimentally measured was $f = 1414$ Hz (for pure, dry N_2). Thus, $\tau = 247$ μs , and it is obvious that the deactivation of ozone by N_2 is not fast with respect to the modulation frequency and nitrogen is a poor bath gas for detecting ozone with the PAS. We note that the magnitude of the effect that this inefficient deactivation has on the PAS signal is a function of modulation frequency and will be worse at higher frequencies.

7.4 Conclusions

We show direct evidence of ozone photodissociation inside a PAS cell. Although this photodissociation pathway is historically well-known, there has been a dearth of discussion on the topic within the aerosol PAS literature and its effects on the accuracy of PAS calibrations seem to have been ignored until very recently. We provide evidence that the issue lies with ozone itself by presenting more particle-based calibrations that agree with gas-phase NO_2 calibrations. We show that adding oxygen can significantly enhance the PAS signal when ozone is present (up to a point). In general, the results presented here appear to agree with Bluvshstein et al. [11], in which a lower cell calibration constant was observed for ozone than for aerosols. We further expand on this work by suggesting this effect can be explained by inefficient deactivation of O_3^* by N_2 . While Davies et al. [12] saw no issues when calibrating

with ozone, and we note it may be possible to do so under the right conditions (e.g. 100% O₂), these are not the conditions typically used for ozone calibration and we suggest choosing other calibrants for aerosol PAS. We suggest further study of the phenomenon, with ozone and other gas-phase calibrants, to investigate the physical chemistry involved and fully vet other calibrants. Although these issues would not be expected with aerosols, in which rate constants for deactivation are more similar to reactions in the liquid phase rather than gas phase, aerosol calibrations can present a host of other uncertainties, including those associated with measuring particle number concentration (roughly 10%) and the refractive index. Thus, we conclude that NO₂ provides the best balance between usability, availability, and accuracy for calibration of visible-NIR calibrations of aerosol PASs and specifically caution against the use of ozone.

References

- (1) Roessler, D.; Faxvog, F. *Applied Optics* **1980**, *19*, 578–581.
- (2) Japar, S. M.; Szkarlat, A. C. *Combustion Science and Technology* **1980**, *24*, 215–219.
- (3) Moosmüller, H.; Arnott, W.; Rogers, C.; Chow, J.; Frazier, C.; Sherman, L.; Dietrich, D. *Journal of Geophysical Research: Atmospheres* **1998**, *103*, 28149–28157.
- (4) Arnott, W. P.; Moosmüller, H.; Rogers, C. F.; Jin, T.; Bruch, R. *Atmospheric Environment* **1999**, *33*, 2845–2852.
- (5) Lewis, K.; Arnott, W. P.; Moosmüller, H.; Wold, C. E. *Journal of Geophysical Research: Atmospheres* **2008**, *113*.
- (6) Lambe, A. T.; Cappa, C. D.; Massoli, P.; Onasch, T. B.; Forestieri, S. D.; Martin, A. T.; Cummings, M. J.; Croasdale, D. R.; Brune, W. H.; Worsnop, D. R., et al. *Environmental science & technology* **2013**, *47*, 6349–6357.
- (7) Wiegand, J. R.; Mathews, L. D.; Smith, G. D. *Analytical chemistry* **2014**, *86*, 6049–6056.
- (8) Zhang, X.; Kim, H.; Parworth, C. L.; Young, D. E.; Zhang, Q.; Metcalf, A. R.; Cappa, C. D. *Environmental science & technology* **2016**, *50*, 1681–1690.
- (9) Lack, D. A.; Lovejoy, E. R.; Baynard, T.; Pettersson, A.; Ravishankara, A. *Aerosol Science and Technology* **2006**, *40*, 697–708.
- (10) Lack, D. A.; Richardson, M. S.; Law, D.; Langridge, J. M.; Cappa, C. D.; McLaughlin, R. J.; Murphy, D. M. *Aerosol Science and Technology* **2012**, *46*, 555–568.
- (11) Bluvshstein, N.; Flores, J. M.; He, Q.; Segre, E.; Segev, L.; Hong, N.; Donohue, A.; Hilfiker, J. N.; Rudich, Y. *Atmospheric Measurement Techniques* **2017**, *10*, 1203–1213.

- (12) Davies, N. W.; Cotterell, M. I.; Fox, C.; Szpek, K.; Haywood, J. M.; Langridge, J. M. *Atmospheric Measurement Techniques Discussions* **2018**, *2018*, 1–19.
- (13) Miklós, A.; Hess, P.; Bozóki, Z. *Review of scientific instruments* **2001**, *72*, 1937–1955.
- (14) Arnott, W. P.; Moosmüller, H.; Walker, J. W. *Review of Scientific Instruments* **2000**, *71*, 4545–4552.
- (15) Cross, E. S.; Onasch, T. B.; Ahern, A.; Wrobel, W.; Slowik, J. G.; Olfert, J.; Lack, D. A.; Massoli, P.; Cappa, C. D.; Schwarz, J. P., et al. *Aerosol Science and Technology* **2010**, *44*, 592–611.
- (16) Yung, Y.; DeMore, W., *Photochemistry of Planetary Atmospheres*; Oxford University Press: 1999.
- (17) Fischer, D. A.; Smith, G. D. *Aerosol Science and Technology* **2017**, *52*, 393–406.
- (18) Silver, J. A. *Applied Optics* **2005**, *44*, 6545–6556.
- (19) Gillis, K. A.; Havey, D. K.; Hodges, J. T. *Review of Scientific Instruments* **2010**, *81*, 064902.
- (20) Kalkman, J.; van Kesteren, H. *Applied Physics B* **2008**, *90*, 197–200.

CHAPTER 8

MULTIPAS-UV: A PORTABLE, THREE-WAVELENGTH, SINGLE-CELL PHOTOACOUSTIC SPECTROMETER FOR AMBIENT AEROSOL ABSORPTION IN THE UV AND VISIBLE

8.1 Introduction

Photoacoustic spectroscopy (PAS) is a photothermal method of measuring absorption of light by a sample. It has become increasingly used to measure aerosol absorption due to its insensitivity to scattering. It has been described thoroughly in chapters 4 and 6, as well as in the literature, so its operating principal will not be discussed here and the reader is instead referred to those discussions. However, what is generally lacking from those sources and what will be discussed here is the prospect of ultraviolet (UV) photoacoustic spectroscopy.

Traditionally, most photoacoustic spectrometers have provided absorption measurements in the visible and near-infrared portions of the spectrum. Table A.1 provides an overview of existing PAS instrumentation. Initially, PASs operated at a single wavelength or achieved multiple wavelengths by using multiple sample cells with a single wavelength per cell. For example, this is the case of Lack et al. [1] and Ajtai et al. [2]. More recently, researchers have employed supercontinuum lasers and multiple diode lasers with a system of dichroic mirrors to obtain data at multiple wavelengths in a single cell. Such approaches include the commercially available, diode laser, 3-wavelength PASS-3 (Droplet Measurement Technologies, Boulder, CO) [3], the instrument of Sharma et al. [4] using a supercontinuum laser to access 417, 475, 542, 607, and 675 nm with bandwidths of 56–80 nm, the work of Radney and

Zangmeister [5] with a tunable laser accessing 500–840 nm, the PAS of Linke et al. [6] that operates at 445, 532, and 660 nm, and the work described here in chapter 6 and in Fischer and Smith [7] that operates at 406, 532, 662, and 780 nm. Notably, only one of these instruments, that of Ajtai et al. [2], which operates at the standard Nd:YAG harmonics of 266, 355, 532, and 1064 nm, provides any coverage in the UV. Although the commercially available photoacoustic extincometer (PAX, Droplet Measurement Technologies) is available at the wavelength of 375 nm, it is a single-wavelength instrument with coverage very close to the visible region of the spectrum, and therefore provides little advantage over multi-wavelength instruments with coverage at 405 nm. The work of Wiegand et al. [8] and the subsequent work described here in chapter 4 that used a Hg-arc lamp to access 301, 314, 364, 406, 436, 546, 578, and 662 nm provided a step towards providing a multi-wavelength UV-visible PAS, though these instruments suffered from relatively high detection limits.

In this chapter, I will describe the construction and development of a three-wavelength, single-cell, multipass UV-visible photoacoustic spectrometer structured around three diode lasers. The instrument, called “MultiPAS-UV”, represents a significant improvement on the work presented in chapter 4 and an extension of the modular PAS design presented in chapter 6. The design and calibration methods will be presented along with a discussion of preliminary data and the current limitations of the instrument.

8.2 Materials and Methods

8.2.1 Instrument Description

Figure 8.1 shows a block diagram of MultiPAS-UV (MP-UV). The entire setup is constructed with a cage system for stability and portability (Thorlabs) and is mounted on a custom-made honeycomb breadboard (Thorlabs); the breadboard itself is mounted on top of an aluminum frame made of 80/20 aluminum extrusion that houses the electronics for the PAS. The

entire setup fits inside a standard Pelican case for protection and transport. The optical system consists of three diode lasers that operate at 445 nm (Coherent OBIS), 377 nm (Coherent OBIS), and 320 nm (LASOS Lasertechnik, GmbH); the lasers provide 75, 50, and 20 mW output power, respectively. Commercial optical isolators (Thorlabs) protect the 445 and 377 nm lasers from optical feedback; the 320 nm is not protected due to a lack of suitable isolators/optics for that wavelength. The lasers are made colinear with a series of dichroic mirrors (Semrock), and turned into the PAS cell using a silver mirror. From there, the colinear beams pass through a central aperture in a custom-made, highly reflective, cylindrical mirror ($R > 99\%$), pass through the PAS cell, and strike an identical cylindrical mirror at the rear of the PAS cell (although the second mirror lacks the central aperture). In this arrangement, the mirror forms a multipass laser cell to provide a power enhancement of roughly 30; [9] the rear mirror is held in a standard kinematic mount (Thorlabs) for alignment in the horizontal and vertical directions, while the front mirror is held in a rotatable mirror mount (Thorlabs) for rotational alignment. The mirror substrates were purchased from Thorlabs and custom-coated by Evaporated Coatings, Inc. (ECI); the holes were drilled by Precision Glassblowing (Centennial, Colorado). The mirrors were further processed by hand polishing the back surface of the mirrors with 1 μm polishing paper to remove the frosted surface finish to improve laser transmission. The windows of the cell are UV-transmissive quartz windows with a custom anti-reflection coating on both sides to minimize losses during window transmission (Evaporated Coatings, Inc.). The small amount of light transmitted through the back multipass mirror is captured with a 50.8 mm diameter, $f = 40$ mm UV-coated mirror (Thorlabs) to focus the light onto an amplified Si photodiode (Thorlabs) for measurements of the effective power within the cell. The photodiode is calibrated to a power (rather than intensity) scale using a commercial power meter (Newport 918D UV-Si + 841-PE-USB).

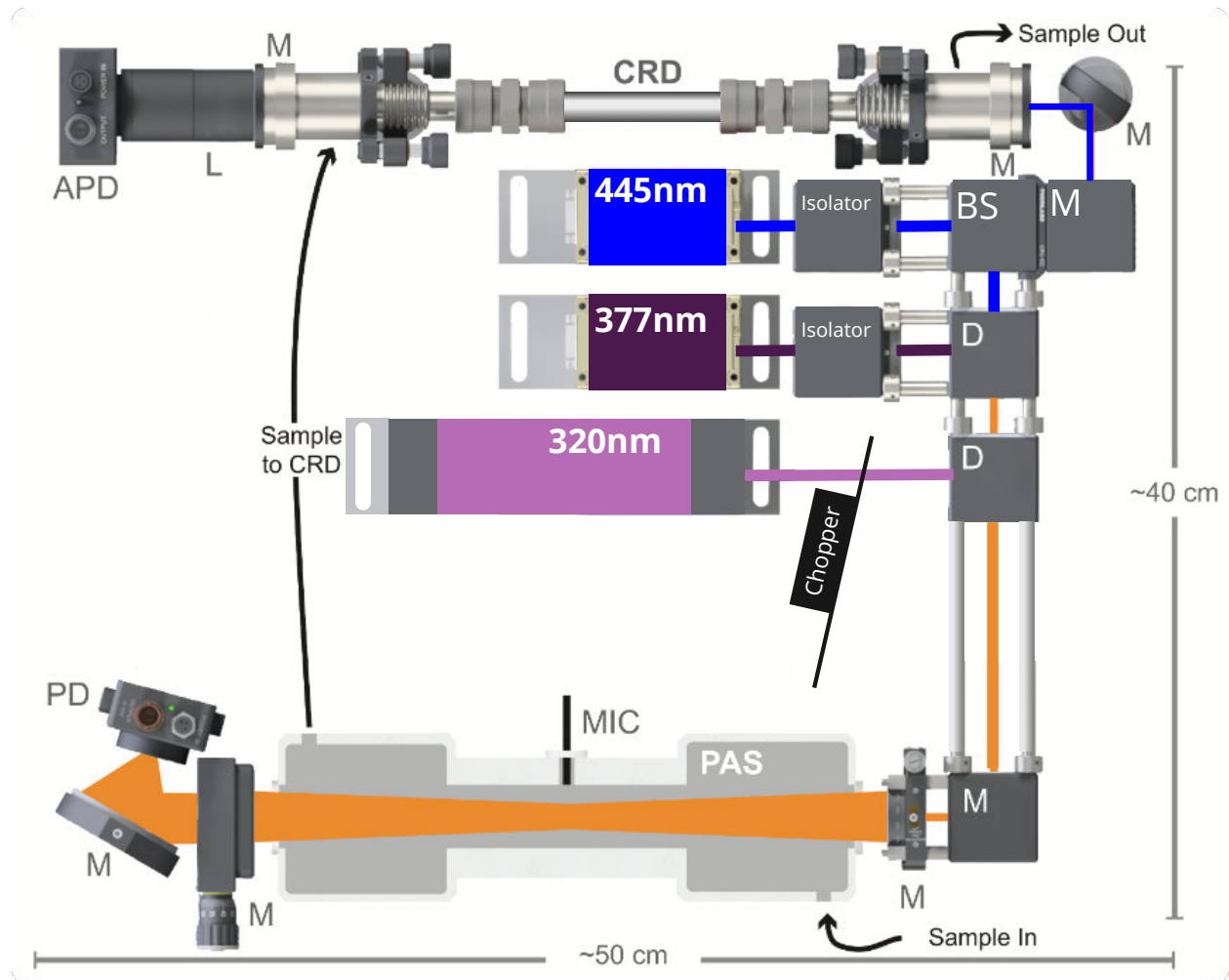


Figure 8.1: Schematic diagram of the MP-UV. M = mirror, D = dichroic mirror, L = lens, BS = 90:10 beamsplitter, and (A)PD = (avalanche) photodiode.

The PAS cell is machined from aluminum (UGA Instrument Shop). It consists of a central resonator 150 mm long by 25 mm diameter with $\lambda/4$ acoustic resonators on either end to minimize window noise; it is the same design described in chapter 6, Fischer and Smith [7], and Lack et al. [10]. An optoacoustic microphone (Optimic 4110, Optoacoustics, Moshav Masor, Israel) is placed at the center point of the cell for detection of the acoustic signal. The microphone signal is digitized with a 24-bit USB sound card (ICUSBAUDIOMH, Startech.com, Lockbourne, OH, USA) that samples at 44 kHz; an identical sound card is used to digitize the photodiode signal. The 445 and 377 nm lasers are modulated electronically using a standard 3.3V square wave from a Teensy 3.6 microcontroller platform. The 320 nm lacks the ability for electronic modulation and is instead modulated with a mechanical chopper wheel (Thorlabs) using a 100-slot chopper wheel; the reference signal for the chopper is provided using the same Teensy microcontroller that modulates the other lasers. The lasers are modulated around the resonant frequency of the cell (typically 1400 Hz, determined experimentally), each separated by a gap of 1 Hz (see Figure A.1 as an example). A custom LabVIEW program acquires the signals from the sound cards and performs a fast-Fourier transform (FFT) on each signal to extract the microphone and PD signal for each wavelength. The LabVIEW program also communicates with the microcontroller to set the modulation frequencies of the lasers and also a built in pinch valve/HEPA filter (N-research and Pall, respectively) combination for automated backgrounds (see Appendix E).

For the 445 nm laser, a 90:10 beamsplitter is used to divert 10% of the laser beam into a cavity ringdown (CRD) cell, as described in chapter 2 and chapter 6. The custom-made CRD cell is roughly 0.4 m in length and 12 mm internal diameter (UGA Instrument Shop). The mirrors for the CRD cell were custom made to be centered at 445 nm and are 99.996% reflective (FiveNine Optics, Boulder, CO), and the mirror mounts are held in standard kinematic mounts (Thorlabs). The CRD signal is acquired with an avalanche photodiode (Thorlabs PDA100A) and digitized with a digital USB oscilloscope (PicoScope 2000A, Pico

Technology). The oscilloscope acquires a block of waveforms in an on-board buffer and sends the block to the LabVIEW program for co-addition and fitting using a discrete Fourier transform method. [11–13]

8.2.2 Instrument Calibration

The PAS is calibrated to a 10.29 ppm ($\pm 5\%$) standard mixture of NO₂ in N₂ (Airgas). The mixture is further diluted with clean, dry N₂ (Airgas). Although a standard mixture was used for calibration, it is not necessary to explicitly know the concentration of the NO₂ because the CRD measures absorption by NO₂ directly. Its primary purpose is to provide a calibration method for the PAS. It allows measurement of absorption due to NO₂ at *exactly* the same wavelength used in the PAS (445 nm) because the same laser is used; thus any uncertainties in the concentration or absorption cross-section become irrelevant. The known concentration from the standard mixture is used only as a secondary check to ensure the CRD is measuring the correct absorption .

8.2.3 Aerosol Generation

Nigrosin aerosol was generated using a constant output atomizer (TSI 3076) with an aqueous solution of nigrosin (4 g L⁻¹, Sigma Aldrich, CAS# 8005-03-6) and dried using a homemade silica-gel diffusion dryer. Atomized, dried particles were size selected using an electrostatic classifier (TSI 3080) and differential mobility analyzer with a 10:1 sheath flow to sample flow ratio (DMA, TSI 3085). Monodisperse aerosols were sent to the PAS cell and then in series to a condensation particle counter (CPC, TSI 3775). They were delivered to each instrument using conductive silicone tubing. The aerosol sample was pulled through the instrument using the internal pump of the CPC and the flow rate was maintained at 330 SCCM total flow with a critical orifice (Lenox Laser, Glen Arm, Maryland). The refractive index from Bluvshstein et al. [14] was used to calculate nigrosin absorption cross sections

using Mie theory assuming a geometric standard deviation of 1.05. Mie theory calculations were performed in MATLAB.

Carbon black aerosols were provided by the National Institute of Standards (NIST) as part of a blind study (those performing the measurements did not know the composition of the sample). The concentrated solution provided by NIST was diluted according to the included instructions by diluting one vial of the provided sample into 100 mL of deionized water.

8.2.4 Ambient Aerosol

Ambient aerosols were sampled in Athens, Georgia (33.948875 N, -83.374428 W) during March 2018. Aerosol-laden air was drawn through a silica gel diffusion dryer and split in parallel to MP-IV and MP-UV. Each PAS had an identical diaphragm pump and flow-limiting orifice that set the flow at approximately 320 SCCM for each instrument. The instruments were operated in autonomous mode, in which a background is automatically performed every 30 minutes using a built-in valve and HEPA filter; a frequency sweep is conducted at the same time. The background and frequency sweep consumes 6 minutes, such that the overall sample time is 24 minutes.

8.2.5 Curve Fitting

Carbon black spectra and ambient aerosol spectra were fit to a power law function:

$$b_{abs}(\lambda) = \beta\lambda^{-\hat{a}} \quad (8.1)$$

where b_{abs} is the absorption due to aerosols, β is a scaling factor, λ is the wavelength of light, and \hat{a} is the absorption Ångström exponent (AAE). The data were fit in R using non-linear least squares.

8.3 Results and Discussion

8.3.1 Calibration and Stability

Calibration with Nitrogen Dioxide

Figure 8.2 shows a typical calibration curve, wherein the absorption due to NO_2 is plotted on the x -axis and the PAS signal is plotted on the y -axis, both at 445 nm. The dark blue points and error bars show the absorption as measured with the CRD and its uncertainty (± 1 SD), while the light blue points and error bars represent the absorption calculated according to $b_{abs-445} = N\sigma_{445}$ (where N is the NO_2 number density and σ_{445} is the NO_2 absorption cross section at 445 nm according to Burrows et al. [15]) and the uncertainty on the accuracy of $[\text{NO}_2]$, respectively. The uncertainty on the $N\sigma$ method is dominated by the uncertainty on the rotameter used to control the flow of NO_2 ; clearly, using a CRD for calibration significantly reduces the uncertainty on the calibration, although the two methods provide nearly the same calibration constant.

The PAS calibration constant (i.e. the slope of the line in Figure 8.2) depends on the PAS cell sensitivity constant, the microphone constant, and the power impinging upon the sample. Therefore, if the power is known and each wavelength is normalized to the effective power inside the PAS cell, a single calibration constant can be used for all wavelengths. Further, this calibration constant can be measured at one wavelength and applied to others without the need to measure a calibrant at those wavelengths (as in chapters 4 and 6). This is useful when a suitable calibrant does not exist for a particular wavelength, as is the case for 320 and 377 nm, which are in a region of the spectrum where there are few gas-phase absorbers and those that do exist (such as NO_2) photodissociate and thereby lead to erroneous calibrations. The 445 nm laser was explicitly chosen for use in the MP-UV and as the CRD wavelength for calibration purposes. Because 445 nm is beyond the photodissociation threshold for NO_2 (approximately 420 nm), it allows for a simple calibration using NO_2 , which – in theory –

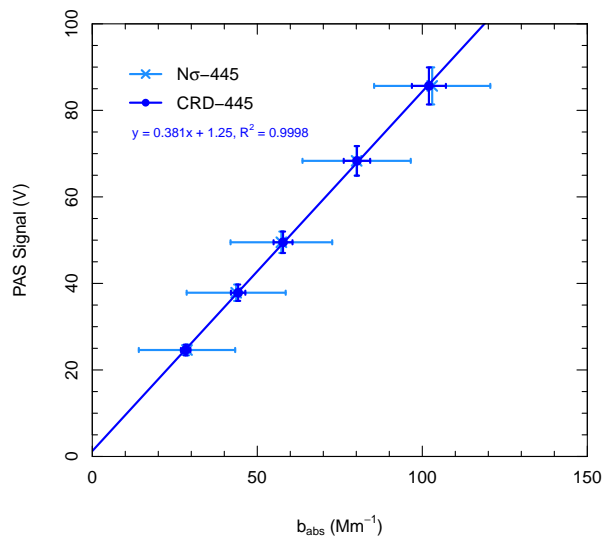


Figure 8.2: Calibration curve for MP-UV obtained with NO_2 . Dark blue points are compared directly to the 445 nm CRD; light blue points are obtained through calculations based on $[\text{NO}_2]$ and σ_{NO_2} and demonstrate that the CRD agrees well with expected values. The x-error bars for the $N\sigma$ case are dominated by errors in knowing the flow rate for NO_2 dilutions; the error on the CRD is much smaller. The line represents the best-fit to the CRD data.

can then be applied to 320 and 377 nm by normalizing to power. However, it is apparent in Figure 8.2 that the y -axis is not normalized to power, as in $(S - S_0)/p$ (in V/W), where S is the PAS signal for a given calibrant, S_0 is the PAS background signal, and p is the effective laser power in the PAS cell. The calibration here differs in that only PAS signal ($S - S_0$, in mV) is plotted on the y -axis. This is done due to difficulties in measuring the effective power at all three wavelengths used in the MP-UV. Specifically, the multipass mirrors and/or the coating applied to them appears to absorb UV light (but not blue light) such that very little UV light reaches the photodiode that is used to measure the effective power. This is further compounded by the fact that the photodiode's responsivity is smallest in the UV, and in fact it is not rated for measurements below 320 nm. This has so far prohibited successful measurement of the effective power at 320 and 377 nm and made calibration difficult.

Power Calibration with Nigrosin

To circumvent the difficulties associated with measuring the effective power at 320 and 377 nm, the calibration is repeated with nigrosin aerosols. Figure 8.3 shows the calibration as performed with nigrosin. Here, the x -axis was calculated using Mie theory and the refractive index of nigrosin as measured by spectroscopic ellipsometry. [14] The slopes of each best-fit line relative to the 445 nm line provide the scaling factor for the effective power of each wavelength. Coincidentally, the 320 and 377 nm laser appear to have very close to the same effective power, while the 445 nm laser has a higher effective power; this trend will, however, change with mirror alignment.

Stability

In order to test the stability of the instrument, an Allan deviation test was performed. Allan deviation provides a measure of an instrument's "ultimate" (best-case-scenario) detection limit. [16, 17] It was performed by flowing clean, dry nitrogen through the instrument

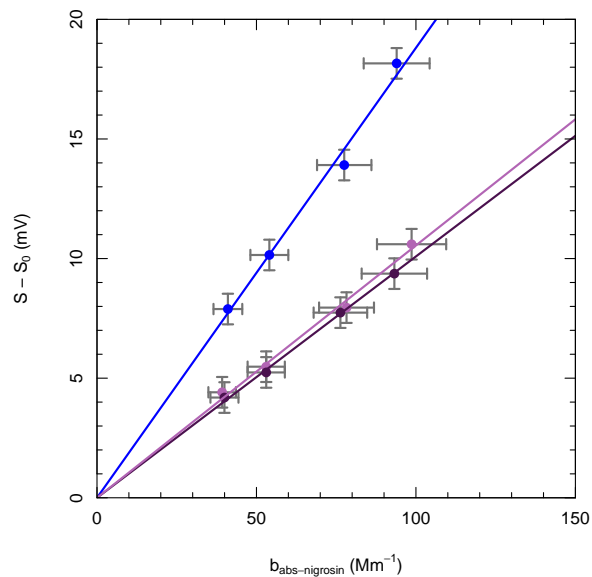


Figure 8.3: Determination of PAS effective powers with nigrosin. The blue line is the PAS signal from nigrosin against predicted absorption calculated from Mie theory at 445 nm. The pink line is the same for 320 nm, and the purple line is the same but for 377 nm. When normalized by effective power, all wavelengths should fall on the same line; however, because power cannot be easily measured, the ratio of the best-fit slopes provides the ratio of the effective powers. Error bars are uncertainty on the particle concentration and refractive index (X) and 1 standard deviation of a 30-second PAS measurement (S) and background (S_0). Slopes for each line are 0.18809, 0.10089, and 0.10548, for 445, 375, and 320 nm, respectively.

overnight and then performing the Allan deviation calculations on the data using the “allanvar” package for R. [18, 19] Figure 8.4 shows the results of the Allan deviation experiment. The x -axis shows the averaging or cluster time, while the y -axis shows the Allan deviation in absorption units (Mm^{-1}). The initial portion of the curve, with a negative slope, indicates improvement in the signal with increased averaging times as random noise is averaged out. The turnover represents the optimum averaging time, which is roughly 100–500 seconds for all channels here; the y value at the turnover represents the instrument’s ultimate detection limit, which is 0.2–0.3 Mm^{-1} for all channels. Beyond the turnover, where the slope becomes positive, is the region where instrument drift begins to outweigh the benefit of increased averaging. The curves for the PAS data are typical of other PAS instruments, although the optimum averaging time is relatively short. For example, the 4-wavelength PAS presented here is more stable with an optimum averaging time of approximately 1000 seconds (Figure 6.2). Further, the detection limits are slightly higher, although still $<1 \text{ Mm}^{-1}$. The addition of the chopper for the 320 nm was expected to make that wavelength less stable than the electronically modulated lasers used for other wavelengths, and indeed it is the least stable channel according to Allan deviation. Likewise, the lower powers associated with the UV lasers were expected to increase the detection limits over those of the 4-channel PAS.

The CRD (triangles in Figure 8.4A) does not behave as expected from a typical Allan deviation analysis. Although the deviation begins to decrease as normal, it turns over after a very short time (about 10 seconds). Then, at about 100 seconds, the signal quickly decreases again and levels off at the expected optimum averaging time of roughly 1000 seconds (expected through comparison to Figure 6.2A and Langridge et al. [17]). This indicates a non-random component of the signal with a time constant between 10 and 100 seconds. In other words, averaging more than 10 seconds causes the drift to be included in the measurement, while averaging more than 100 seconds causes it to be averaged out. In Figure 6.2B there is a clear sinusoidal drift present in the ringdown time that is on the order of 0.2–0.3

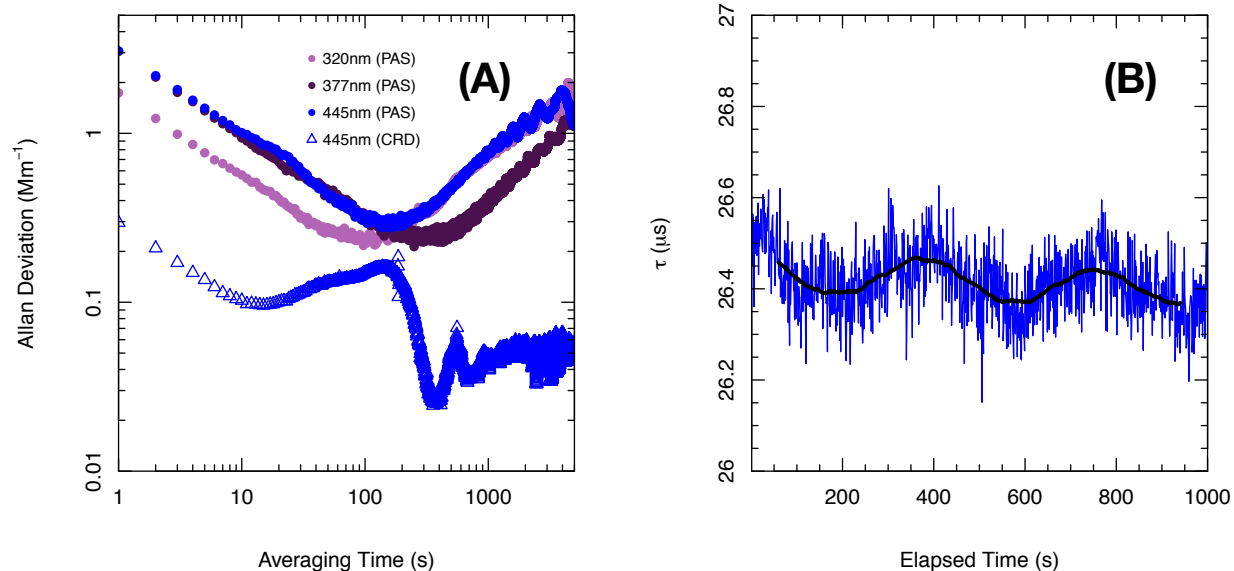


Figure 8.4: Results of Allan deviation from MP-UV (A) and time series of τ_0 (B). The results suggest in (A) an ultimate detection limit of approximately 0.2 Mm^{-1} for all three channels, with an optimum averaging time of approximately 500 seconds. The CRD has a much lower detection limit, but exhibits non-random noise, as evident as a sinusoid with a period of roughly 200 seconds in (B). The blue line in (B) represents the 1-second data; the solid black line is a 120-second rolling average of the data, shown to highlight the sinusoidal trend.

μs ($<1\%$ of τ_0). The source of this drift remains unknown, but future developments should attempt to stop it. In the meantime, averaging for more than two minutes (as we typically do) negates this drift, and its overall effect is orders of magnitude smaller than the extinction expected by ambient aerosols.

8.3.2 Carbon Black

MultiPAS-UV and MultiPAS-IV were used as part of a global PAS intercomparison organized by NIST during July of 2017. Figure 8.5 shows the results of this study. Although the spectral shape and AÅE of this sample are unknown to the author, the sample was selected by NIST as a surrogate for black carbon. Thus, it was expected to have a power law dependence with

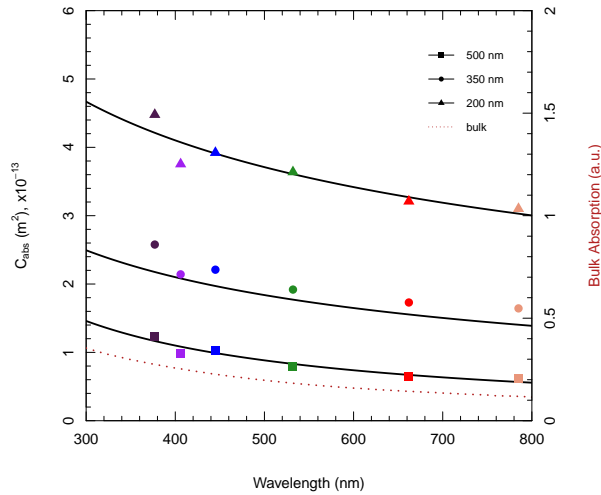


Figure 8.5: UV-visible spectrum of a commercial carbon black ink provided by NIST as part of a global intercomparison of PASs.

wavelength and an AÅE of approximately 1 or less. The AÅEs obtained by fitting a power law function (8.1) to the data shown here are 0.98, 0.58, and 0.45, for 200, 350, and 500 nm particle sizes, respectively. The 320 nm laser was not yet functional during this study, and so was not used.

8.3.3 Ambient Aerosol Absorption

Figure 8.6 shows a spectrum of ambient aerosol obtained with both the MP-UV and MP-IV during March 2018 in Athens, Georgia. At first glance, the spectra from the two instruments, shown in Figure 8.6A, do not appear to agree. This highlights an important design choice when developing the MP-UV: The wavelength of 445 nm was chosen to allow NO₂ calibrations (as described above) and also to provide overlapping spectra from MP-UV and MP-IV in the case of mismatched spectra. Such a mismatch could result from systematic differences in instrument calibrations or particle losses in the sample line that differ between the two instruments. In this case, a power law was fit to the spectrum from each instrument, and

the values calculated for 406 nm were averaged; the data points from each instrument were then scaled accordingly to match the average (i.e. the MP-UV data were scaled up and the MP-IV data were scaled down). The resulting spectrum, shown in Figure 8.6B still does not follow a single power law, as may be initially expected. However, there is no reason the spectrum of ambient aerosols must follow a single power law. In fact, if the sample were composed partially of brown carbon and partially of black carbon, as may be expected for the well-mixed and aged “background” aerosols in Athens, GA where samples were collected, the spectrum may fit a dual power law function more closely. Specifically, a high-AAE would be expected toward the UV and a lower AAE close to 1.0, would be expected in the red and near-IR. Figure 8.6C shows the results of fitting a dual power law function to the ambient spectrum. The 662 and 785 nm points (where absorption by C_{Br} is essentially non-existent) were log transformed and fit with a linear least-squares regression, such that the slope of the best fit line represents the AAE. The extrapolation of this fit provides the black line in Figure 8.6C, and the area under the curve (black shaded region) represents the absorption due to BC. The BC absorption was then subtracted from the combined dataset to remove the BC contribution to absorption. A power law (8.1) was then fit to the residual spectrum to retrieve the absorption due to C_{Br} (brown line/shaded brown area in Figure 8.6C). A dual power law seems to approximate the spectral shape much more closely. Moreover, the AAEs generally agree with values expected for BC and C_{Br} . The retrieved AAE_{BC} was 0.9, which is close to the generally-accepted literature value of 1.0 [20] and matches previous observations of aerosols in Athens, Georgia. [7] The $AAE_{C_{Br}}$ was approximately 6, which falls in the middle of the range reported for C_{Br} in the literature (2–9). [21, 22]

8.4 Conclusions

The MP-UV presented here provides a significant improvement over existing PAS instruments by providing measurements well into the UV portion of the spectrum (320 and 377

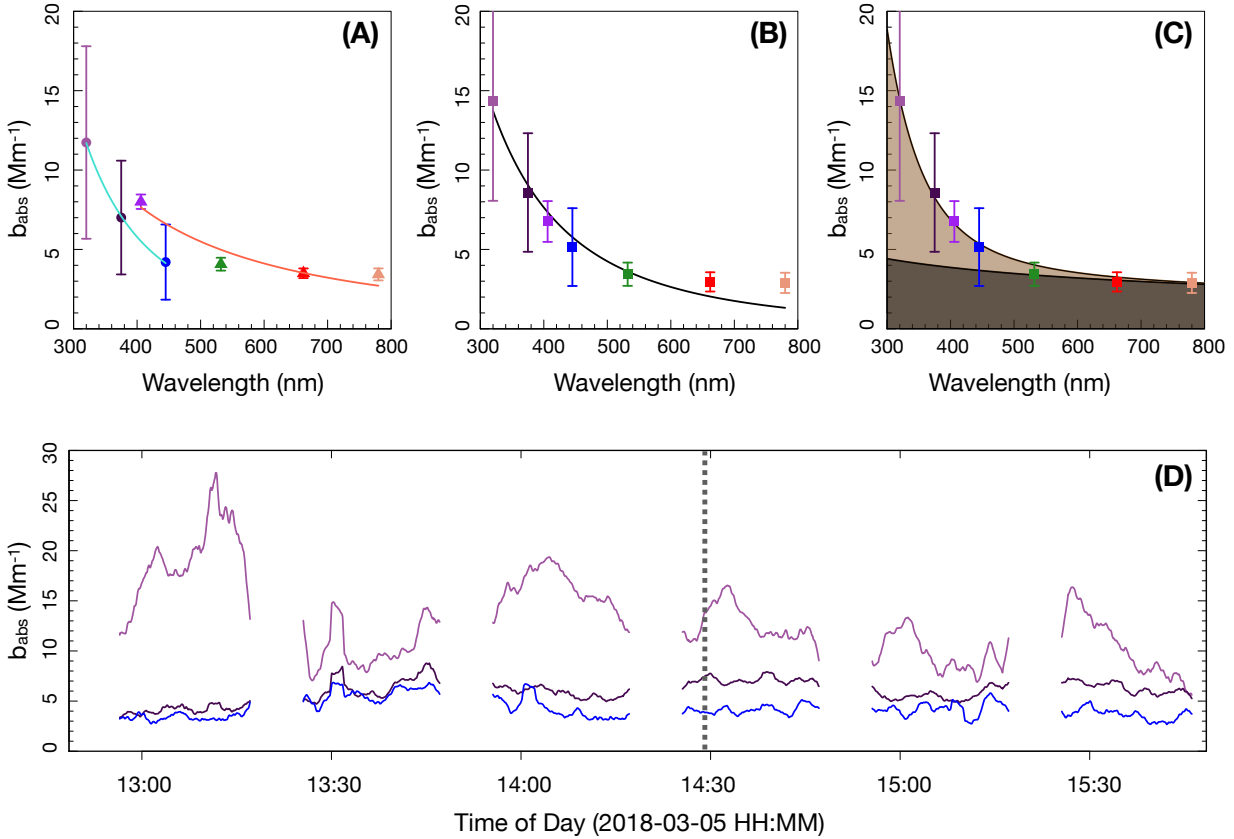


Figure 8.6: UV-visible spectrum (A-C) and absorption time series of ambient aerosols in Athens, Georgia on March 5, 2018. (A) Uncorrected spectra from the two PASs fit to individual power laws. (B) Spectra scaled to each by overlapping data and fit to a single power law. (C) Spectra scaled and fit to a dual power law representing black carbon absorption (black shaded region) and the residual brown carbon absorption (brown shaded region). (D) Two-minute rolling averages of absorption from the MP-UV; the dashed grey line represents the time of the spectra shown in (A-C). Error bars in (A-C) represent ± 1 SD of the 2-minute average plus an estimate of the accuracy on the calibration and the error involved in scaling the spectra; error bars are bigger for the MP-UV due to difficulties in measuring the effective powers of the lasers.

nm) in a compact and portable instrument that uses low-power, continuous-wave lasers. Previously, one group had provided measurements at 266 nm using a Nd:YAG laser, though this has been used primarily on solid, inorganic aerosols, likely due to a propensity for pulsed lasers to vaporize liquid aerosols. [2, 23] This problem has been overcome here by using low-power diode lasers. A commercial instrument, the PAX, is available for measurements at 375 nm, but it is only available in a single-wavelength version and does not provide measurements deep into the UV. The instrument presented here is improved by combining 3 wavelengths into a single cell to provide measurements down to 320 nm while simultaneously providing overlap with visible PAS instruments; ultimately, this feature reduces uncertainty in calculating the AÅE. Although this instrument provides advances over previous instruments, it is not without issues. Specifically, measurement of the effective power at 320 and 377 nm has proven nearly impossible; future work should attempt to develop a better (optical) method to do this that does not rely on aerosol calibrations. To date, this is the major limitation of this instrument, and fixing the problem will greatly aid in sampling.

8.5 Acknowledgements

The carbon black samples presented in this chapter were provided by Dr. Chris Zangmeister at the National Institute of Standards in Gaithersburg, Maryland.

References

- (1) Lack, D. A.; Richardson, M. S.; Law, D.; Langridge, J. M.; Cappa, C. D.; McLaughlin, R. J.; Murphy, D. M. *Aerosol Science and Technology* **2012**, *46*, 555–568.
- (2) Ajtai, T.; Filep, Á.; Utry, N.; Schnaiter, M.; Linke, C.; Bozóki, Z.; Szabó, G.; Leisner, T. *Journal of Aerosol Science* **2011**, *42*, 859–866.
- (3) Nakayama, T.; Suzuki, H.; Kagamitani, S.; Ikeda, Y.; Uchiyama, A.; Matsumi, Y. *Journal of the Meteorological Society of Japan. Ser. II* **2015**, *93*, 285–308.
- (4) Sharma, N.; Arnold, I. J.; Moosmüller, H.; Arnott, W. P.; Mazzoleni, C. *Atmospheric Measurement Techniques* **2013**, *6*, 3501–3513.
- (5) Radney, J. G.; Zangmeister, C. D. *Analytical Chemistry* **2015**, *87*, 7356–7363.
- (6) Linke, C.; Ibrahim, I.; Schleicher, N.; Hitzenberger, R.; Andreae, M. O.; Leisner, T.; Schnaiter, M. *Atmospheric Measurement Techniques* **2016**, *9*, 5331–5346.
- (7) Fischer, D. A.; Smith, G. D. *Aerosol Science and Technology* **2017**, *52*, 393–406.
- (8) Wiegand, J. R.; Mathews, L. D.; Smith, G. D. *Analytical chemistry* **2014**, *86*, 6049–6056.
- (9) Silver, J. A. *Applied Optics* **2005**, *44*, 6545–6556.
- (10) Lack, D. A.; Lovejoy, E. R.; Baynard, T.; Pettersson, A.; Ravishankara, A. *Aerosol Science and Technology* **2006**, *40*, 697–708.
- (11) Mazurenka, M.; Wada, R.; Shillings, A. J. L.; Butler, T. J. A.; Beames, J. M.; Orr-Ewing, A. J. *Applied Physics B* **2005**, *81*, 135–141.
- (12) Everest, M. A.; Atkinson, D. B. *Review of Scientific Instruments* **2008**, *79*, 023108.
- (13) Bostrom, G.; Atkinson, D.; Rice, A. *Review of Scientific Instruments* **2015**, *86*, 043106.

- (14) Bluvshstein, N.; Flores, J. M.; He, Q.; Segre, E.; Segev, L.; Hong, N.; Donohue, A.; Hilfiker, J. N.; Rudich, Y. *Atmospheric Measurement Techniques* **2017**, *10*, 1203–1213.
- (15) Burrows, J.; Dehn, A.; Deters, B.; Himmelmann, S.; Richter, A.; Voigt, S.; Orphal, J. *Journal of Quantitative Spectroscopy and Radiative Transfer* **1998**, *60*, 1025–1031.
- (16) Allan, D. *Proceedings of the IEEE* **1966**, *54*, 221–230.
- (17) Langridge, J. M.; Richardson, M. S.; Lack, D.; Law, D.; Murphy, D. M. *Aerosol Science and Technology* **2011**, *45*, 1305–1318.
- (18) Carrio, J. H. allanvar: Allan Variance Analysis., R package version 1.1, 2015.
- (19) R Core Team R: A Language and Environment for Statistical Computing.; R Foundation for Statistical Computing, Vienna, Austria, 2017.
- (20) Bond, T. C.; Bergstrom, R. W. *Aerosol Science and Technology* **2006**, *40*, 27–67.
- (21) Bond, T. C. et al. *Journal of Geophysical Research: Atmospheres* **2013**, *118*, 5380–5552.
- (22) Yang, M.; Howell, S. G.; Zhuang, J.; Huebert, B. J. *Atmospheric Chemistry and Physics* **2009**, *9*, 2035–2050.
- (23) Ajtai, T.; Filep, Á.; Schnaiter, M.; Linke, C.; Vragel, M.; Bozóki, Z.; Szabó, G.; Leisner, T. *Journal of Aerosol Science* **2010**, *41*, 1020–1029.

CHAPTER 9

THE SPECTRAL DEPENDENCE OF THE AETHALOMETER CORRECTION FACTOR¹

¹ Fischer, D.A., Z. Cheng, R. Saleh, and G.D. Smith. 2018. To be submitted to *Atmosphere*.

9.1 Introduction

The routine, “push-button” measurement of absorbing aerosols is important for climate models, air quality monitoring, and industrial research and development. Numerous techniques exist for measuring aerosol absorption, although they typically have serious data artifacts, present limitations that inhibit their use as push-button instruments, and/or are prohibitively expensive for wide-spread deployment. One widely employed technique for measuring aerosol absorption is the aethalometer. The aethalometer was first proposed by Hansen et al. [1], and was quickly commercialized into an autonomous push-button instrument. [2] The name is derived from *aeth-*, the Greek root for fiery or sooty, and the instrument was initially intended as a “soot-o-meter”. [1] The operating principle of the instrument is to draw particle-laden air over a filter while measuring the transmission of light through the filter; in theory, any change in light transmission through the filter can be attributed to aerosol absorption. The wavelength of the light source can be changed quickly to measure the absorption at numerous wavelengths. Early versions of the aethalometer used only a single wavelength, and the first published version of the instrument was used to measure black carbon (BC) at 530 nm. [1] Subsequent versions operated at various wavelengths, including 325 nm, 632 nm, and 880 nm. [3, 4]. More versions have used 2 wavelengths, [5] and most recently a 7-wavelength version has been developed. [6] The “set-it-and-forget-it” nature of the aethalometer combined with its relative affordability, compactness, and wide wavelength coverage have led it to become widely adopted for the measurement of aerosol absorption.

Initial intercomparisons to then-state-of-the-art instruments were quick to validate the aethalometer as a viable method for measuring BC. [3, 4, 7, 8] Since that time, the science of measuring aerosol absorption has been advanced greatly, and artefacts have begun to emerge with accompanying correction routines. [9] These include filter loading effects, in which the transmission of the filter is not linearly related to [BC] [10, 11] and multiple-scattering effects

wherein the aethalometer reports an overly high absorption due to scattering by the filter medium [6, 12]. Moreover, the multiple scattering factor has been shown to vary based on filter material, aerosol type, and sampling location. [13–15] While some sources have also noted a dependence on single scattering albedo (and thus wavelength), other sources state that the multiple-scattering factor is independent of wavelength; the instrument manufacturer and most literature sources recommend a single, wavelength-independent constant based only on the filter material. This constant is even built in to the data processing algorithms of newer aethalometers.

Much of the recent work on aerosol absorption has focused on measuring the wavelength dependence of absorption. Typically, this dependence is represented by the absorption Ångström exponent (abbreviated AÅE and represented as \hat{a}):

$$b_{abs}(\lambda) = \beta\lambda^{-\hat{a}} \quad (9.1)$$

where b_{abs} is absorption, λ is wavelength, and β is a scaling factor. Thus, a larger AÅE indicates a sharper increase in absorption in ultraviolet regions of the spectrum. This is typical of brown carbon (C_{Br}) aerosols, whereas BC aerosols typically have a smaller AÅE (roughly 1.0). [16] As such, this quantity is useful in climate modeling, has been used to differentiate different contributors to the aerosol absorption spectrum, and provides valuable information for source appointment. The 7-wavelength aethalometer provides exceptional wavelength coverage for these studies and has seen widespread application. [17–19] Although it has been noted in these studies that correction factors are necessary to quantitatively measure absorption with an aethalometer, they often use the aethalometer to get the shape of the spectrum and scale it absolutely with a more quantitative method at a single wavelength. This assumes any correction factors are wavelength independent; if they are not, it could significantly affect the value of the AÅE and the interpretation of the results.

Many of the studies that have focused on aethalometer intercomparisons have used other filter-based methods. Those that have compared to measurements of suspended aerosols have been limited in their wavelength coverage due to the sparse wavelength coverage of most *in-situ* instrumentation (e.g. photoacoustic spectrometers). Here, we perform an intercomparison between a 7-wavelength aethalometer (AE-33, Magee Scientific, Inc.) and three custom, multi-wavelength photoacoustic spectrometers. The aethalometer provides measurements from 370–950 nm, while the three PAS’s combined measure at 7 unique wavelengths spanning from 375–780 nm, with several wavelengths that directly overlap with the aethalometer. This provides an unrivaled comparison of the 7-wavelength aethalometer to measurements of suspended aerosols. We used the instruments to measure absorbing aerosols generated under various combustion conditions, which yielded a range of ÅÅ’s. This intercomparison definitively shows a wavelength dependence of the aethalometer’s correction factors.

9.2 Materials and Methods

9.2.1 Aethalometer Operating Principle

The aethalometer used in this study was a 7-wavelength, dual-spot aethalometer by Magee Scientific AE-33. Although it is a commercial instrument and has been described in detail elsewhere, [1, 6] its operating principle will be presented here to aid in the interpretation and discussion of our results. The instrument is illuminated by LEDs at 370, 470, 520, 590, 660, 880, and 950 nm. It contains two detectors, one reference detector that measures transmission through the blank filter and one sensing detector that measures the transmission through the sample-laden filter. The attenuation then would appear to follow the Beer-Lambert Law:

$$ATN = -\ln \left[\frac{I}{I_0} \right] \quad (9.2)$$

Here, ATN is the optical attenuation, I is the sensing detector’s signal, and I_0 is the reference detector’s signal. Over some time, dt , the absorption coefficient for each wavelength is then obtained by:

$$b_{abs}(\lambda) = \frac{dATN(\lambda)}{dt} \frac{A}{QC_s} \quad (9.3)$$

where Q is the instrument’s volumetric flow rate, A is the spot area, and t is time. C_s is the multiple scattering parameter, as introduced by Weingartner et al. [12], which corrects for multiple scattering events on the filter that would seemingly increase the absorption. C_s is assumed to be 1.79 for a quartz filter and 2.14 for a PTFE-coated filter. The instrument further processes the data to BC concentration by dividing b_{abs} by an assumed mass-absorption cross-section for BC (σ): $[BC](\lambda) = b_{abs}(\lambda)/\sigma(\lambda)$. Because the AE-33 is a “DualSpotTM” instrument, it introduces the sample over the filter at two separate spots with two distinct flow rates. This allows it to adjust $[BC]$ by the loading compensation parameter, k , in real-time. Thus, the AE-33 reports data as equivalent $[BC]$ (in units of $\mu\text{g m}^{-3}$ as a function of wavelength. Although this does not make sense physically because the concentration of a species should be independent of the measurement wavelength, it is the standard that has been adopted. For this work, we are uninterested in $[BC]$, and multiply the reported values by $\sigma(\lambda)$ as reported by Weingartner et al. [12] and the AE-33 manual, $\sigma(\lambda) = 14625/\lambda$ $\text{m}^2 \text{g}^{-1}$, to obtain b_{abs} :

$$b_{abs}(\lambda) = [BC](\lambda) \times \sigma(\lambda) \quad (9.4)$$

Thus, the data here include the dual-spot loading correction and the built-in multiple scattering factor.

9.2.2 Photoacoustic Spectrometers

We used our custom-built MultiPAS series of photoacoustic spectrometers for this experiment, which are described in detail elsewhere. [20] We used three versions of the instrument presented by Fischer and Smith [20]: (1) the 4-wavelength version exactly as described therein (406, 532, 662, and 780 nm), (2) a 3-wavelength UV version described in the supplemental information (320, 375, and 445 nm), and (3) a 3-wavelength visible version described in the supplemental information (422, 532, and 782 nm). The 4-channel and 3-channel UV PASs were calibrated with NO_2 to a built in cavity ringdown spectrometer; the remaining 3 channel instrument was calibrated to NO_2 using known dilutions of a standard mixture. The flow to each PAS was controlled by a miniature diaphragm pump and a critical orifice on each instrument and was held at approximately 300 SCCM for the 4-channel and 3-channel UV instruments and 180 SCCM for the other 3-channel instrument.

9.2.3 Aerosol Generation

Figure 9.1 displays a block diagram of the experimental setup. Aerosols were generated by the combustion of benzene in a custom-made quartz combustion chamber that was 12 cm long and had an inner diameter of 0.5 cm (Scientific Glass Blowing Shop, University of Georgia). Two semi-cylindrical heating elements (Thermcraft RH252-S-L) are positioned opposite each other on either side of the tube to create a furnace with a maximum temperature of 1200 °C. The temperature was measured with K-type thermocouples and controlled using commercial PID controllers (Omega, CNi3244). Compressed air was filtered and passed through a 30 cm by 3.5 cm inner diameter bubbler (UGA Scientific Glass Blowing Shop) containing benzene, which allowed control of the air-to-fuel ratio via Dalton's law. An additional stream of nitrogen acts as a passive diluent to allow further fine-tuning of the combustion conditions. The passive diluent has the apparent effect of making the combustion conditions richer. [21,

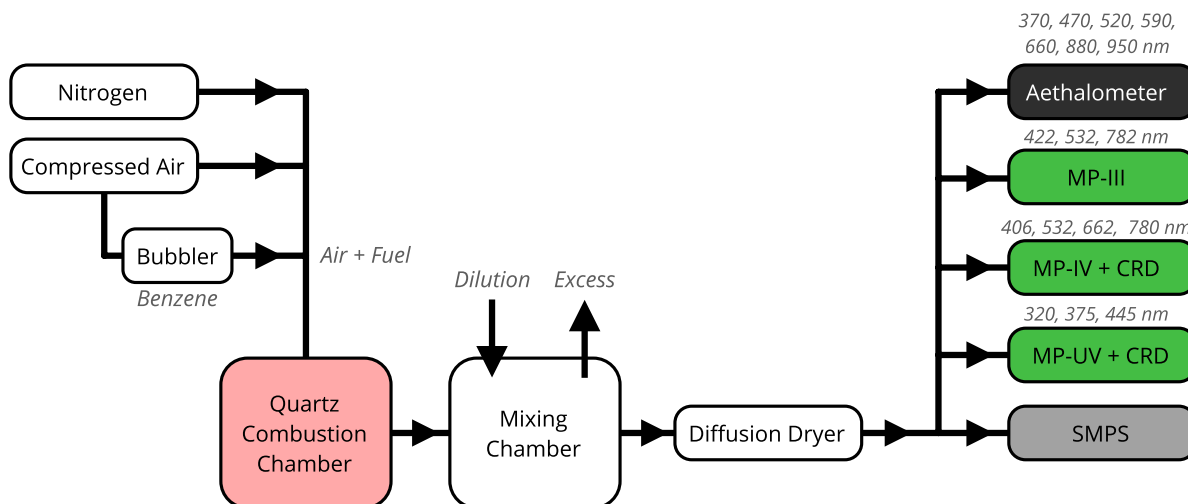


Figure 9.1: Block diagram of the experimental setup for the aethalometer-PAS intercomparison.

22]. This passive diluent also acts to inhibit ignition and/or self-ignition and explosion inside the combustion chamber and provide a more even temperature inside the furnace. [23, 24] The combustion products are emitted into a glass mixing chamber (13 cm by 13 cm I.D., UGA Glass Shop) and diluted with filtered, compressed air. The diluted sample is dried in a silica-gel diffusion dryer and conveyed to the instruments in quarter-inch copper tubing, and the internal pump of each instrument is allowed to pull each instrument’s desired flow. The full details of the combustion system will be presented in a forthcoming publication. [25] For this work, two types of sample were used: (1) a C_{Br} -like, high AÅE sample and a BC-like, low-AÅE sample; however the low-AÅE sample has some C_{Br} present due to limitations in the combustion system.

9.2.4 Data Processing

Due to a hardware malfunction, the 780 nm laser on the MultiPAS-IV was not available during this study and the 320 nm channel was still under development at the time of the

study. Thus, these two data points were excluded from all data sets. Due to errors in measuring the effective power of the 375 nm laser, those data were scaled by a factor of 1.48, which was determined from the difference of 375 nm PAS measurements of nigrosin compared to Mie theory. To align the MP-III and MP-IV data, the MP-III data was scaled to the MP-IV data at 532 nm (where the two instruments share a common wavelength); the 532 nm point from the MP-III was then discarded from all fits to avoid over-weighting that wavelength.

Data were first fit to a power law (Equation 9.1) via non-linear least squares in R. However, the near-zero values at long wavelengths combined with the relatively low number of data points led to poor fits at long wavelengths for both the PAS and aethalometer, as shown in Figure 9.2A. As a result, the spectra were instead fit by performing a linear fit to the log-transformed data. Doing so provided a better fit across the spectrum, especially at long wavelengths, as shown in Figure 9.2B. Although this seems a small detail, it has a significant effect on the retrieved AÅEs and the perceived wavelength-dependence of the aethalometer correction factors.

To derive correction factors for each of the two AAE cases, unscaled aethalometer data were fit as above, and all PAS data were treated as a single data set and fit also as above. The fits were then divided (AE-33/PAS) to derive the correction factors from 370-850 nm. Note that this requires extrapolation of the PAS data from 375 back to 370 nm and from 782 nm to 950 nm.

9.3 Results and Discussion

The accuracy error of the aethalometer is clearly evident in Figure 9.3. At first glance, the AE-33 appears to report absorption values roughly 10 times higher than the PAS throughout the UV-Visible-NIR spectrum. This is not unexpected, as other groups have observed similar factors that have been dependent on the sample type. Further investigation of this

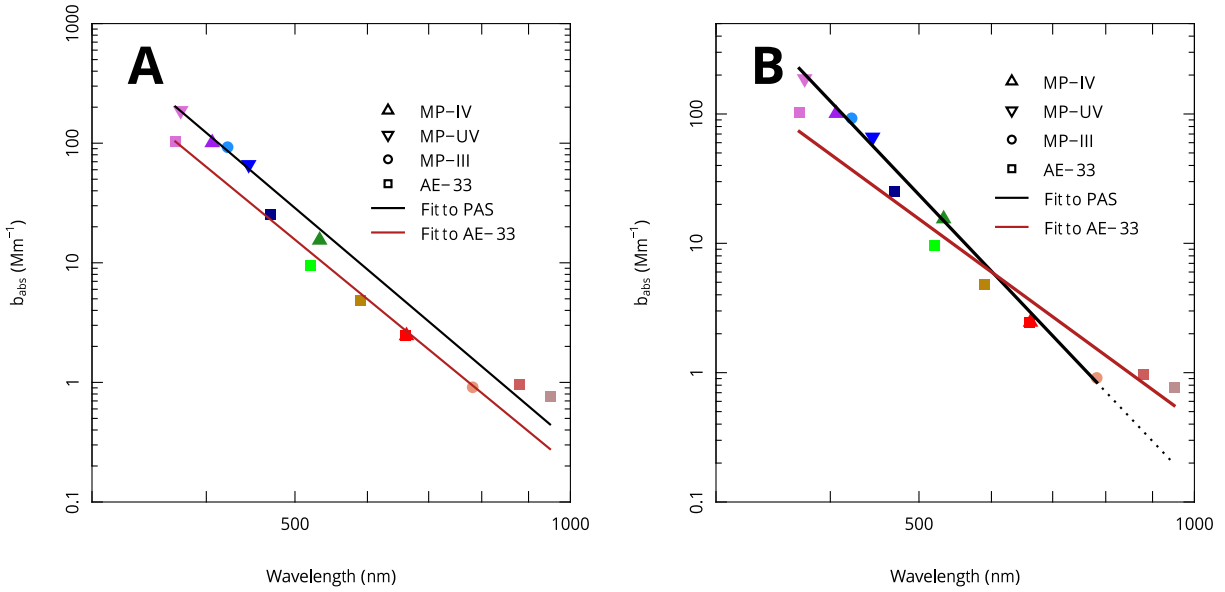


Figure 9.2: Comparison of non-linear least squares fit to Equation 9.1 (A) and Log-transform Fits (B). Aethalometer data have been scaled by $b_{abs-662-PAS}/b_{abs-660-aeth}$ for plotting purposes. $\hat{A}AE_{PAS-nls} = 6.5$, $\hat{A}AE_{aeth-nls} = 6.3$, $\hat{A}AE_{PAS-log} = 7.5$, $\hat{A}AE_{aeth-log} = 5.2$.

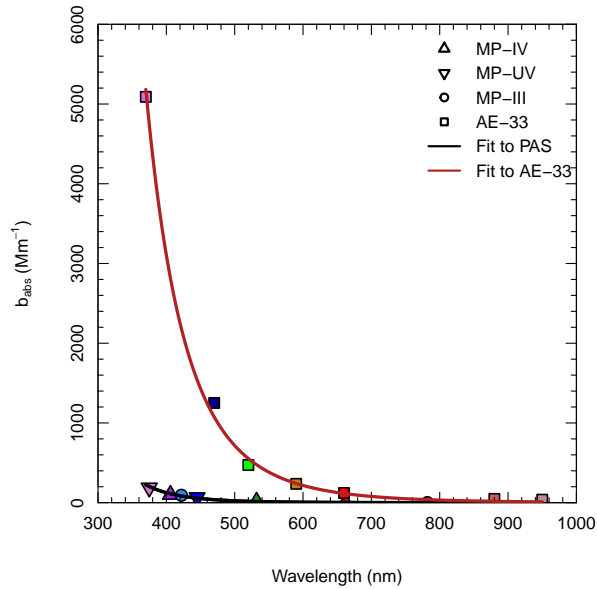


Figure 9.3: The same data as Figure 9.2, but without scaling the aethalometer data. Plotted as the raw data, there is clearly a large error in the aethalometer.

phenomenon reveals the aetholometer offset is also dependent on wavelength; although this has been suggested in the literature, it is typically ignored and has not been well-studied. This wavelength dependence becomes more easily visible when the aetholometer data are scaled to the PAS by the factor $b_{abs-662-PAS}/b_{abs-660-aeth}$ to enable plotting on the same scale. Figure 9.2 shows the same data as Figure 9.3, but scaled to the PAS and plotted on a log-log plot. These data, representing a C_{Br} -like sample, show a smaller aethalometer correction factor at short wavelengths and a larger factor at long wavelengths. Although the non-linear power law fit in Figure 9.2A provides very similar AÅE's for both the aethalometer and PAS data (6.3 and 6.5, respectively), this appears to be coincidental as it is evident upon closer inspection that the power law does not fit the long-wavelength data well. The linear fit to the log-transformed data in Figure 9.2B fits the data much better (at least qualitatively), and provides a more C_{Br} -like AÅE of 7.5; conversely, the AÅE derived from the aethalometer data shows a lower AÅE (5.2) than was obtained with the non-linear fit, although the log-transform fit does seem to match the data better. Although there is no way of knowing what the “correct” AÅE is for the data, the sample used here was expected to have a very high AÅE in the range of 7–8.

Figure 9.4 shows the log-transform data and fits for a sample representing a BC-heavy mix of C_{Br} and BC; the AÅE of this sample was expected to be slightly above 1. Here, the PAS provides a lower AÅE than the aethalometer, with the PAS yielding 1.4 and the aethalometer yielding 1.9. Again, neither of these can be chosen as correct or excluded as incorrect, but the AÅE of 1.4 is closer to the expected value of close to 1. Interestingly, the AE-33 provided a lower AÅE than the PAS for a high-AÅE sample and a higher AÅE for the low-AÅE sample, implying the correction factors for the aethalometer are not only wavelength dependent but also sample dependent.

Figure 9.5 shows the correction factors for the aethalometer across the UV-visible-NIR spectrum. The y -axis represents the value the aethalometer data should be multiplied by

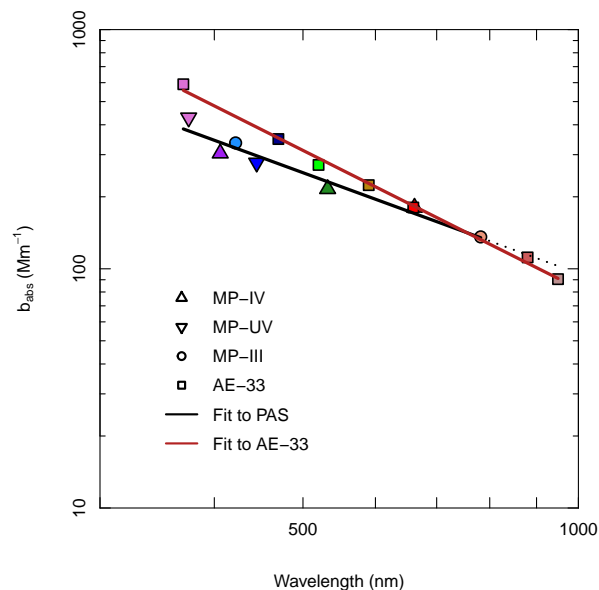


Figure 9.4: Comparison of low-AÅE spectra for the PAS and aethalometer. Aethalometer data have been scaled by $b_{abs-662-PAS}/b_{abs-660-aeth}$ for plotting purposes. $A\AA E_{PAS} = 1.4$, $A\AA E_{aeth} = 1.9$

to match the PAS data (or, more precisely, the fits to the data). Thus, a value of 1 implies perfect agreement, while smaller values imply a larger difference between the PAS and aethalometer. It is evident that the correction factor is a strong function of both wavelength and AÅE, with shorter wavelengths and lower AÅEs requiring a smaller correction factor. Also shown in Figure 9.5 (as points) are the slopes from the linear regressions between the AE-33 and MP-IV shown in Figure A.3. Thus, the points represent comparisons of the aethalometer at 4 wavelengths for ambient aerosol data collected in March 2017 in Athens, GA (see chapter 6 for more details). The aerosols in Athens are likely well-aged background aerosols that represent a mix of BC and C_{Br} . The short wavelength absorption (i.e. at 406 nm) is primarily due to C_{Br} , while the long-wavelength absorption (i.e. 532, 662, and 785 nm) is primarily due to BC. Thus, the data at 406 nm would be expected to exhibit a similar correction factor as the high-AÅE laboratory case (blue line), while the other points

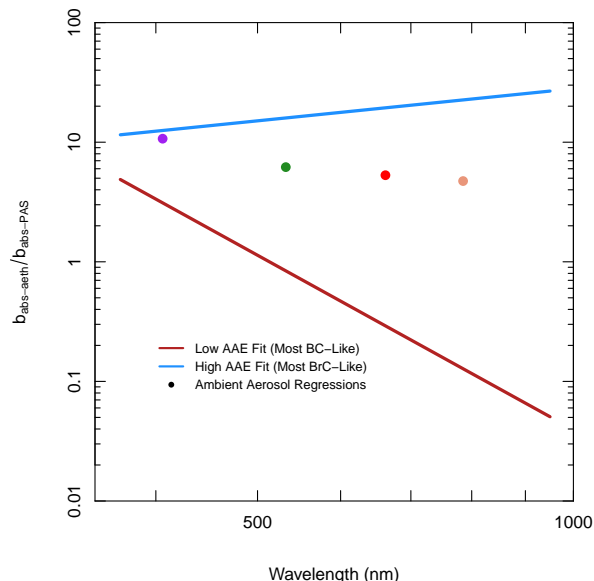


Figure 9.5: The wavelength-dependent correction factors derived for the aethalometer for each of the samples generated here. Points represent linear regression of previously collected ambient data, shown in Figure A.3.

would be expected to be more similar to the low-AAE case. This is indeed the trend that is observed, and all points fall within the curves calculated for the two cases. Although this is useful information, it calls into question many aethalometer measurements.

9.4 Conclusions

The work here calls into question the validity of aethalometer measurements. Specifically, it appears that the aethalometer exhibits falsely high readings by up to an order of magnitude. Although this was in large part already known, it has to now been widely believed that the data could be easily corrected by (1) applying a multiple scattering factor or (2) scaling the 7-wavelength aethalometer data to a single-wavelength PAS measurement (or both). Unfortunately, it appears that the correction factors are both wavelength- and sample-dependent.

Thus, correcting the aethalometer data either requires prior knowledge of the sample or a detailed set of (e.g.) PAS measurements to compare to. The first case here is impossible with most samples, especially ambient samples for which the aethalometer is often used; the second case is impractical, and calls into question the reason for using the aethalometer if PAS measurements spanning the spectrum are available.

Notwithstanding, this work has been a preliminary investigation into the aethalometer correction factors. With more studies, it may be possible to derive correction factors based on easily measurable parameters, such as the SSA. Similar corrections have already been used for aethalometer data. [6, 17] Although these results call the validity of the aethalometer into question, they are still very preliminary and more work is needed to explore the full effects of AÅE (or sample type) and sample concentration (neglected here) on the correction factors. Further, more comparisons to ambient data should be performed to test any derived correction factors. The goal of this work was not to discredit the aethalometer. Indeed, it is an easy-to-use, widely adopted instrument that makes wavelength-resolved measurements of aerosol absorption routinely possible. Hopefully, additional studies will reveal methods of determining correction factors and allow accurate retrieval of aerosol absorption using aethalometers.

9.5 Acknowledgements

This work was conducted in collaboration with Dr. Rawad Saleh and Zezhen Cheng of the UGA College of Engineering.

References

- (1) Hansen, A.; Rosen, H.; Novakov, T. *Science of The Total Environment* **1984**, *36*, 191–196.
- (2) Hansen, A. D. Aethalometer., US Patent 4,893,934, Jan. 1990.
- (3) Babich, P.; Davey, M.; Allen, G.; Koutrakis, P. *Journal of the Air & Waste Management Association* **2000**, *50*, 1095–1105.
- (4) Hansen, A. D. A.; McMurry, P. H. *Journal of the Air & Waste Management Association* **1990**, *40*, 894–895.
- (5) Wang, Y.; Hopke, P. K.; Rattigan, O. V.; Xia, X.; Chalupa, D. C.; Utell, M. J. *Environmental Science & Technology* **2011**, *45*, 7387–7393.
- (6) Arnott, W. P.; Hamasha, K.; Moosmüller, H.; Sheridan, P. J.; Ogren, J. A. *Aerosol Science and Technology* **2005**, *39*, 17–29.
- (7) Hansen, A. D. A.; Novakov, T. *Aerosol Science and Technology* **1990**, *12*, 194–199.
- (8) Allen, G. *Atmospheric Environment* **1999**, *33*, 817–823.
- (9) Coen, M. C.; Weingartner, E.; Apituley, A.; Ceburnis, D.; Fierz-Schmidhauser, R.; Flentje, H.; Henzing, J. S.; Jennings, S. G.; Moerman, M.; Petzold, A.; Schmid, O.; Baltensperger, U. *Atmospheric Measurement Techniques* **2010**, *3*, 457–474.
- (10) Virkkula, A.; Mäkelä, T.; Hillamo, R.; Yli-Tuomi, T.; Hirsikko, A.; Hämeri, K.; Koponen, I. K. *Journal of the Air & Waste Management Association* **2007**, *57*, 1214–1222.
- (11) Drinovec, L.; Močnik, G.; Zotter, P.; Prévôt, A. S. H.; Ruckstuhl, C.; Coz, E.; Rupakheti, M.; Sciare, J.; Müller, T.; Wiedensohler, A.; Hansen, A. D. A. *Atmospheric Measurement Techniques* **2015**, *8*, 1965–1979.

- (12) Weingartner, E.; Saathoff, H.; Schnaiter, M.; Streit, N.; Bitnar, B.; Baltensperger, U. *Journal of Aerosol Science* **2003**, *34*, 1445–1463.
- (13) Biagio, C. D.; Formenti, P.; Cazaunau, M.; Pangui, E.; Marchand, N.; Doussin, J.-F. *Atmospheric Measurement Techniques* **2017**, *10*, 2923–2939.
- (14) Saturno, J. et al. *Atmospheric Measurement Techniques* **2017**, *10*, 2837–2850.
- (15) Backman, J.; Schmeisser, L.; Virkkula, A.; Ogren, J. A.; Asmi, E.; Starkweather, S.; Sharma, S.; Eleftheriadis, K.; Uttal, T.; Jefferson, A.; Bergin, M.; Makshtas, A.; Tunved, P.; Fiebig, M. *Atmospheric Measurement Techniques* **2017**, *10*, 5039–5062.
- (16) Bond, T. C.; Bergstrom, R. W. *Aerosol Science and Technology* **2006**, *40*, 27–67.
- (17) Ran, L.; Deng, Z.; Wang, P.; Xia, X. *Atmospheric Environment* **2016**, *142*, 132–144.
- (18) Zotter, P.; Herich, H.; Gysel, M.; El-Haddad, I.; Zhang, Y.; Mocnik, G.; Hugglin, C.; Baltensperger, U.; Szidat, S.; Prevot, A. S. H. *Atmospheric Chemistry and Physics* **2017**, *17*, 4229–4249.
- (19) Rivellini, L.-H.; Chiapello, I.; Tison, E.; Fourmentin, M.; Feron, A.; Diallo, A.; N’Diaye, T.; Goloub, P.; Canonaco, F.; Prevot, A. S. H.; Riffault, V. *Atmospheric Chemistry and Physics* **2017**, *17*, 10291–10314.
- (20) Fischer, D. A.; Smith, G. D. *Aerosol Science and Technology* **2017**, *52*, 393–406.
- (21) Zabetakis, M. G. *Flammability characteristics of combustible gases and vapors*; tech. rep.; 1964.
- (22) Li, W. F.; Liu, Z. C.; Tian, J.; Wang, Z. S.; Xu, Y. *International Journal of Automotive Technology* **2015**, *16*, 721–731.
- (23) Wagnon, S. W.; Wooldridge, M. S. *Combustion and Flame* **2014**, *161*, 898–907.

- (24) Kozubková, M.; Kozubek, E.; Nevrlý, V.; Bitala, P.; Štěpánek, O.; Dlabka, J.; Vašínek, M.; Bojko, M.; Zelinger, Z.; Kubát, P.; Grigorová, E. *Procedia Engineering*, 42, 1826–1839.
- (25) Cheng, Z.; Atwi, K.; Tarquinio, D.; Saleh, R. **2018**, *In Preparation*.

CHAPTER 10

SUMMARY AND CONCLUSIONS

Atmospheric aerosols are important components of Earth's radiative budget. Although all aerosols scatter light, and tend to reflect sunlight back toward space to cool Earth, some also absorb sunlight. As the sunlight is absorbed, it is converted to thermal energy in the atmosphere. The exact balance of these effects remains unknown, and as such aerosols are one of the largest uncertainties in climate models. Therefore, narrowing the uncertainties on predictions of Earth's future temperature requires more accurate and precise measurements of aerosol optical properties (scattering and absorption). Making these measurements necessitates the development of new instrumentation for measuring extinction, scattering, and/or absorption by aerosols. This work has worked toward that regard, especially toward developing photoacoustic methods of measuring aerosol absorption.

Initially, this work focused on developing a 4-channel broadband cavity enhanced spectrometer for measuring aerosol extinction from 370–690 nm. This instrument was developed from a single-channel, laboratory instrument into a 4-channel, compact, portable instrument. However, limitations in the cavity ringdown mirrors ultimately limited the instrument's signal to noise ratio. This project was put on hold until new mirrors could be purchased and ultimately transferred to another student for further development; it remains under active development as of this writing.

After stalling on the BBCES project, this work moved toward developing methods of measuring aerosol absorption using photoacoustic spectroscopy. This was initially focused on improving a lamp-based instrument (operating at 301, 314, 464, 405, 436, 546, 578, and 678 nm) with the addition of two lasers to improve detection limits at 405 and 662 nm. This instrument was used to measure the first UV-visible absorption spectrum of laboratory-generated soot during a collaboration at Boston College in Spring 2015. This laboratory campaign put the “hybrid” PAS to the test and revealed some of its flaws. Specifically, it necessarily used short averaging times to successively scan through each wavelength, which limited its detection limits. It was also generally large and bulky, which made traveling with the instrument difficult and expensive. Moreover, further experiments revealed that the lamp was heating the cell over time by a large enough amount to alter the resonant frequency and limit the ultimate detection limit of the instrument. Because of this, subsequent work focused on developing laser-based PASs, while attempting to maintain the wavelength coverage and single-cell nature of the lamp-PAS. The overarching goals of building the laser PASs were to create small, robust, and portable instruments capable of detecting ambient aerosols in very clean environments. This was achieved by constructing a 4-wavelength, single-cell, multipass PAS operating at 406, 532, 662, and 780 nm and a separate 3-wavelength, single-cell, multipass UV PAS operating at 320, 377, and 445 nm. These instruments represent significant improvements over existing instruments from the perspective of detection limits, portability, and wavelength coverage. An additional 3-wavelength, single-cell, multipass PAS was constructed for Dr. Rawad Saleh (UGA College of Engineering), and it operates at 422, 532, and 782 nm (Appendix B). Already, these instruments have been used for varied applications. The 4-wavelength PAS has been used to measure ambient aerosols and to test the efficacy of using ozone as a PAS calibrant. Both the 4-channel and UV-PAS were used in a global intercomparison study of PAS measurements of carbon black. Similarly, all

three of the laser PASs were used to test the accuracy of aethalometer measurements of laboratory-generated soot and brown carbon.

10.0.1 Recommended Future Directions

10.0.2 Instrument Development

Specific future goals related to this work should include further development of the BBCES to make it entirely portable and potentially combining all channels into a single cell. [1] recently published the design for a BBCES capable of acquiring data from 400–650 nm using a laser-driven white light source and custom mirrors, and such a design would offer to streamline the BBCES and solve many of the issues related to flow splitting between the 3 BBCES cavities in the current design. Likewise, the mirror mounts used for the BBCES and CRD are very easy to move out of alignment either through the introduction of external forces (such as sample tubing or an accidental bump from a hand) or heating and cooling of the bellows that form part of the mount, causing expansion and contraction. Many instruments have moved to fixed-mirror design, and such a design is recommended here. [2, 3]

Further development of the UV PAS is needed to develop a more robust method of measuring the effective power. Other improvements to both PASs could include the development of an alternative cell design that is lighter and smaller and adding the components necessary to make the PASs fully self-contained. A single board computer and touch screen in each PAS case would alleviate the need for any external equipment to run the PAS. Adding a mains-power relay that is controlled by a microcontroller would allow the PAS to be controlled entirely from a remote location and would provide the mechanism for an emergency shut off if a necessary situation arose (it currently has to be turned on and off on site, but then can be run remotely, albeit without the ability to shut off the main power).

Future related projects might focus on creating more compact and inexpensive PASs. The relatively recent proliferation of high-power (5W) LEDs has created high power, inexpensive

light sources throughout the visible and near-IR spectrum. Such an instrument might use a tubular cell (as is the employed in the current PAS) or an integrating sphere with multiple LEDs and a single microphone to provide wavelength coverage (although the size of a sphere necessary to achieve accessible resonant frequencies might prove prohibitive).

10.0.3 Instrument Applications

The instruments described here should be used in collaborations involving in-depth studies of absorption and extinction by laboratory-generated and ambient aerosols, ideally paired with other techniques such as filter-based methods, aerosol mass spectrometry, and mass and size measurements. For example, expanding on the work presented in chapter 9 by exploring the dependence of the aethalometer correction factors on wavelength, sample type, and combustion conditions to parameterize them as a function of (e.g.) the absorption Ångström exponent or single scattering albedo could aid greatly in providing a relatively low-cost, low-barrier method of monitoring aerosol absorption. More immediately, the PASs will be used in an upcoming collaboration at Boston College (“BC5”) to study inter-particle mixing of black carbon-containing particles as a function of absorption enhancement by non-absorbing coatings. Finally, the instruments can be paired with wavelength-resolved measurements of extinction and angle-resolved measurements of the scattering phase function to determine an effective complex refractive index of ambient aerosols.

References

- (1) He, Q.; Bluvshstein, N.; Segev, L.; Meidan, D.; Flores, J. M.; Brown, S. S.; Brune, W.; Rudich, Y. *Environmental Science & Technology* **2018**, *52*, 3456–3465.
- (2) Onasch, T. B.; Massoli, P.; Keibarian, P. L.; Hills, F. B.; Bacon, F. W.; Freedman, A. *Aerosol Science and Technology* **2015**, *49*, 267–279.
- (3) Min, K.-E.; Washenfelder, R. A.; Dubé, W. P.; Langford, A. O.; Edwards, P. M.; Zarzana, K. J.; Stutz, J.; Lu, K.; Rohrer, F.; Zhang, Y.; Brown, S. S. *Atmospheric Measurement Techniques* **2016**, *9*, 423–440.

APPENDIX A

SUPPLEMENTAL INFORMATION: A PORTABLE, FOUR-WAVELENGTH, SINGLE-CELL PHOTOACOUSTIC SPECTROMETER FOR AMBIENT AEROSOL ABSORPTION¹

¹ Fischer, D.A and G.D. Smith. 2017. *Aerosol Science and Technology*. DOI: 10.1080/02786826.2017.1413231. Reprinted here according to the usage guidelines of the publisher, Taylor & Francis.

A.1 Comparison to a 7-wavelength Aethalometer

The 7-wavelength aethalometer is a filter-based commercial instrument routinely used to measure aerosol absorption. Here, we use it to assess the performance of the MultiPAS-IV measuring ambient aerosol. Qualitatively, the aethalometer and MultiPAS-IV agree well and track changes in the size distribution and number density, as shown in the time series in Figure 3 and the correlation plots in Figure A.3 with R^2 values of 0.86 to 0.91. Despite the good correlation, the slopes of the linear regression range from 2.2 to 5.0 suggesting that the aethalometer is overestimating the aerosol absorption despite the fact that it ostensibly corrects for multiple scattering effects.

Others have also found that the aethalometer and other filter-based instruments overestimate absorption; for example, Saturno et al. [1] compared an aethalometer to a MAAP and measured the multiple-scattering correction to range from approximately 5 to 7. Likewise, Lack et al. [2] found that a PSAP reported absorption that was up to 1.69 times larger than that measured by a PAS, which they surmised may have originated from the redistribution of liquid-like organics that coat the filter fibers thereby altering their scattering or from an enhancement related to the coating by organic species of embedded absorbing particulate matter. Given the high SSA (662 nm) measured in the present study (median value of 0.87, interquartile range of 0.04), it seems plausible that the particles we sampled also contained a significant organic fraction, and thus similar artifacts may have influenced the aethalometer measurements. Nonetheless, the high degree of correlation between them and the PAS measurements provides a good indication of the PAS's ability to measure ambient aerosol absorption.

A.2 Calibration with Nitrogen Dioxide and Nigrosin

For validation of the NO_2 calibration method, we performed several tests. First, we calculated the expected absorption from the known concentration of NO_2 based on the number density of our stock calibrated mixture, dilutions, and the NO_2 absorption cross sections of Burrows et al. [3] (see Figure A.2A). These data are shown in grey. Note that although they agree well with the CRD data, the x-axis uncertainty is much higher due to uncertainties in the dilution factor and absorption cross section, which are represented by the x-error bars. These errors are explicitly eliminated with the CRD method, with the error there dominated by the standard deviation of the CRD measurements. The good agreement between these two methods suggest no gas losses between the PAS and CRD and indicates that the CRD is a viable calibration method.

Second, we measured NO_2 with the 532 nm PAS channel and plotted it against simultaneous absorption measurements with the 662 nm CRD Figure A.3A. The PAS signal (y-axis) for the 532 nm data has been scaled by the ratio of the absorption cross sections given by Burrows et al. [3] for plotting. Importantly, the power-normalized 532 nm data lie on the same line as the 662 nm data, confirming that the 662 nm calibration is valid for other wavelengths.

Third, we also plotted the nigrosin data collected at all four PAS wavelengths (406, 532, 662, and 780 nm) vs. the predicated absorption calculated using Mie theory in Figure A.2B. The linear least-squares fit to the data yields nearly the same slope as the NO_2 calibration indicating the gas-phase calibration is valid for particles. Also important, all wavelengths fall on the same line (as in the NO_2 calibration), suggesting a single-wavelength calibration is suitable for use at all wavelengths.

Table A.1: Comparison of Aerosol PAS Instruments

Table S1. Comparison of Aerosol PAS Instruments

Citation	Institute / Company	Wavelength(s)	Detection limits	Notes	Portable ? (weight)	
			Mm ⁻¹ (averaging time)	method		
this work	UGA	406, 532, 662, 785 nm	0.71, 0.62, 0.61, 0.75 (2 min.)	2 σ from background	a,f,g,h	yes (34 kg)
Petzold & Niessner (1992)	Technical University of Munich	800 nm	260 (time not specified)	calculated from quoted LOD = 50 μ g/m ³ C	a	no
Petzold & Niessner (1995)	Technical University of Munich	802 nm	4.5 (time not specified)	3 σ from background	a	yes
Arnott et al. (1999)	UNR / DRI	532, 685 nm	0.4 (time not specified)	not specified	a	yes
Kramer et al. (2001)	Technical University of Munich	680 nm	not specified		a	yes
Arnott et al. (2005)	DRI	1047 nm	not specified		a	???
Lack et al. (2006)	NOAA	532 nm	0.08 (60 sec.)	1 σ from Allan deviation	a,f	yes
Lewis et al. (2008)	UNR / DRI	405, 870 nm	not specified		a,g	???
Ajtai et al. (2010)	University of Szeged / Karlsruhe Institute of Technology	266, 355, 532, 1064 nm	35.5, 23.5, 5.2, 0.2 (5 min.)	3 σ from background	b	no
Havey et al. (2010)	NIST / University of Maryland	405 nm	4 (60 sec.)	2 σ from Allan deviation	a	no
Ajtai et al. (2011)	University of Szeged / Karlsruhe Institute of Technology	266, 355, 532, 1064 nm	6.7, 3.5, 0.7, 0.17 (time not specified)	(not specified)	b	yes (100 kg)
Lack et al. (2012)	NOAA	404, 532, 659 nm	0.2, 0.15, 0.4 (1 sec.)	2 σ from background	a,f	yes
Gyawali et al. (2012)	UNR / DRI	355 nm	0.4 (time not specified)	(not specified)	b	???
Haisch et al. (2012)	Technical University of Munich	410 - 710 nm	0.25 - 0.57 (time not specified)	3 σ of soot data	c,g	no
Sharma (2013)	Michigan Tech / UNR / DRI	417, 475, 542, 607, 675 nm *	0.5 - 4.0 (60 sec.)	1 σ from Allan deviation	d,g	no
Wiegand et al. (2014)	UGA	301, 314, 364, 405, 436, 546, 578, 678 nm **	1.3 - 10.2 (20 sec.)	2 σ from NO ₂ sample	e,g	no

Citation	Institute / Company	Wavelength(s)	Detection limits	Notes	Portable ? (weight)	
			Mm ⁻¹ (averaging time)	method		
Radney & Zangmeister (2015)	NIST	500 - 840 nm ***	11 - 21 (5 min.)	not specified	d,g	no
PASS-3 (Nakayama et al. (2015))	DMT	405, 532, 781 nm	1.0, 1.9, 0.7 (10 min.)	2 σ from background	a,g	yes (33 kg)
PAX 375 (Nakayama et al. (2015))	DMT	375 nm	1.3 (10 min.)	2 σ from background	a	yes (18 kg)
Zhang et al. (2016)	UC - Davis	405 and 532 nm	1.7 and 0.8 (2 sec.)	2 σ from background	a,f	yes
Linke et al. (2016)	Karlsruhe Institute of Technology	445, 532, 660 nm	5.6, 6.6, 18 (time not specified)	3 σ from background	a,g	yes
Bluvshstein et al. (2016)	Weizmann Institute	404 nm	not specified		a,f	no
Wang et al. (2017)	University of the Littoral Opal Coast	442 nm	0.28 (200 sec.)	1 σ from Allan deviation	a	yes
Yu et al. (2017)	Aerodyne	532 nm	0.68 (100 sec.)	2 σ from Allan deviation	a	???
Signorell et al. (2017)	ETH	445 nm	not specified		a,h	no

a: single-wavelength laser, b: Nd:YAG laser (fundamental and/or harmonic(s)), c: tunable optical parametric oscillator laser, d: tunable supercontinuum laser, e: Hg lamp, f: multipass laser alignment, g: multiple wavelengths measured with a single PAS cell, h: single optically-trapped particle

* bandwidths of 56 to 80 nm

** bandwidths of 6 to 49 nm

*** bandwidths of 10-20 nm

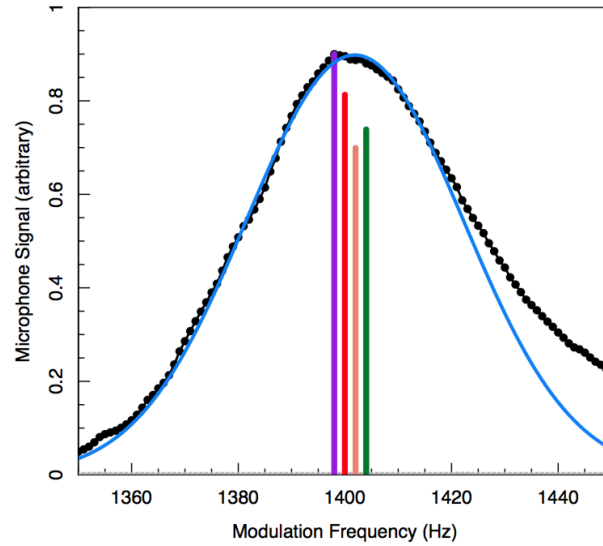


Figure A.1: Microphone response (black circles) as a function of modulation frequency using just the 406 nm laser with NO_2 in the cell. Blue curve is a fit of the data to a Gaussian function. The colored lines (color coded by wavelength) represent the frequency-resolved signals of ambient aerosol absorption derived from a fast Fourier transform (FFT) of the 1-second microphone waveform. The modulation frequencies of the four lasers are separated by 2 Hz.

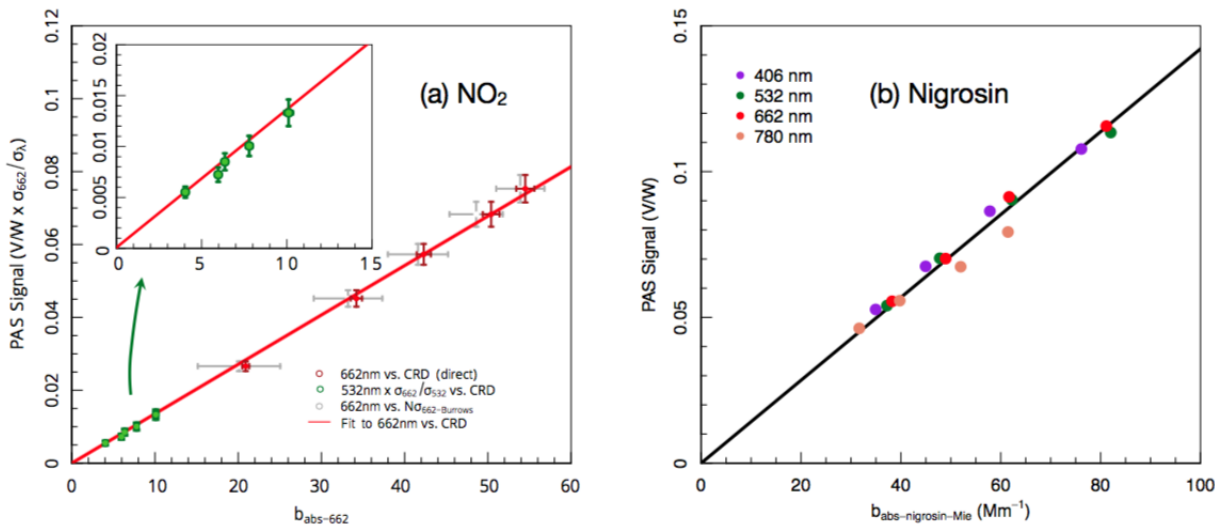


Figure A.2: Calibration Curves for the MP-IV (a) The PAS is calibrated with NO₂ at 662 nm by regressing the power-normalized 662 nm PAS signal against the absorption measured by cavity ringdown spectroscopy at the same wavelength (red circles). The red line is the linear fit to just these data ($y = 1.35 \times 10^{-3}x$, $R^2 = 0.9993$). Grey circles represent $b_{abs-662}$ calculated from the product of NO₂ number density (N) and absorption cross section from Burrows et al. [3]. Also shown is NO₂ absorption measured with the PAS at 532 nm and scaled by the cross section relative to 662 nm. (b) Alternate calibration using size-selected nigrosin particles with absorption calculated using Mie theory. The black line is a linear least-squares fit to the data ($y = 1.42 \times 10^{-3}(VWm^{-1})x$, $R^2 = 0.9980$).

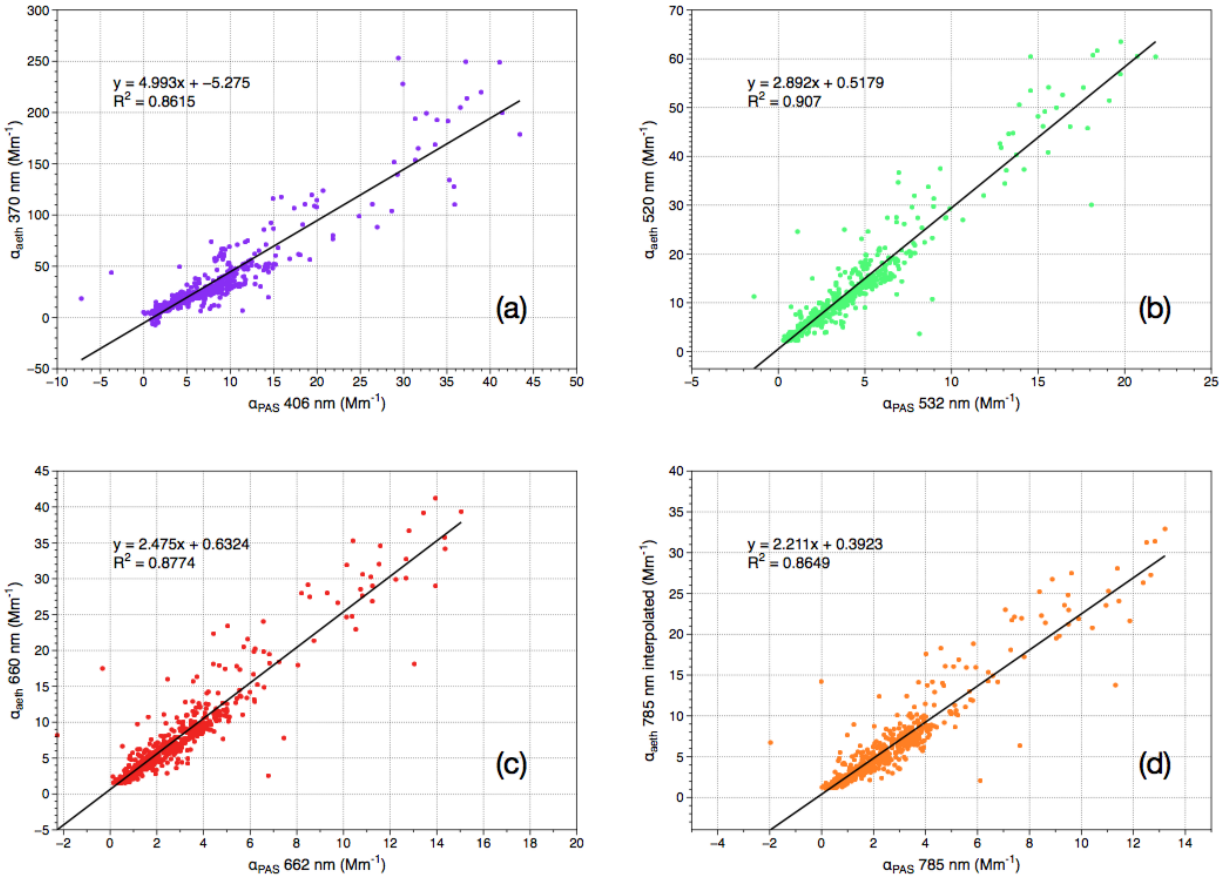


Figure A.3: Correlation plots of aethalometer and PAS absorption measurements of ambient aerosol (Athens, GA; March 3-7, 2017): (a) 370 nm from the aethalometer vs. 406 nm from the PAS, (b) 520 nm from the aethalometer vs. 532 nm from the PAS, (c) 660 nm from the aethalometer vs. 662 nm from the PAS, (d) 785 nm interpolated from the 660 nm and 880 nm data from the aethalometer (assuming an $\text{AAE} = 1$) vs. 785 nm from the PAS. Each data point represents a 10-minute average. Good correlation between the instruments is observed, but the aethalometer overestimates absorption at all wavelengths.

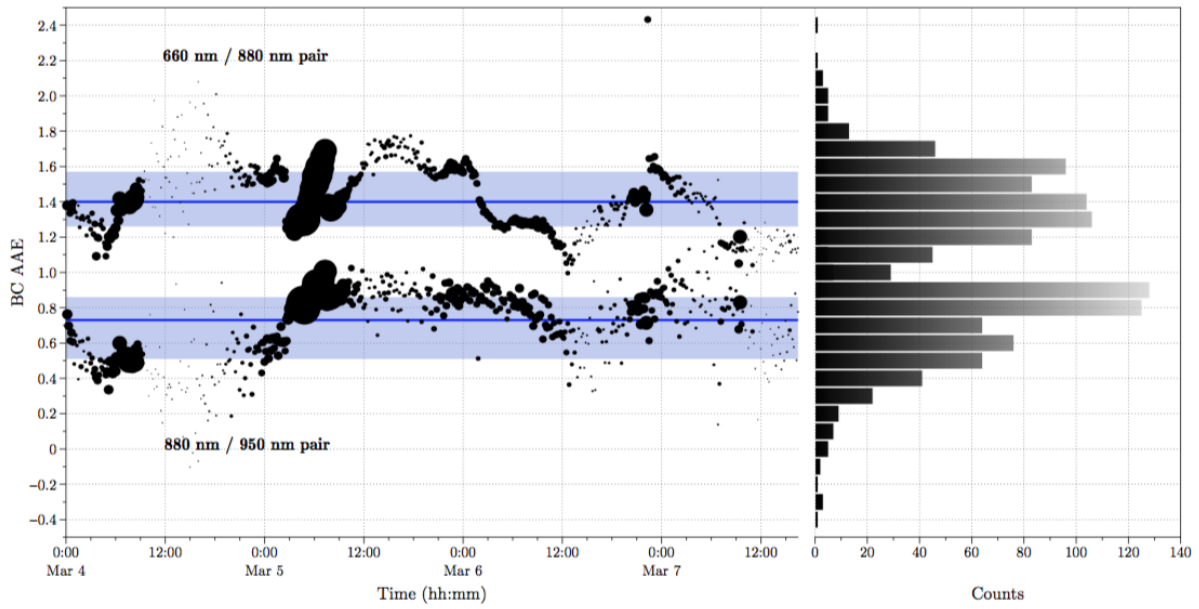


Figure A.4: Time series and histograms of AAE_{BC} values calculated using the aethalometer absorbance values at 660 nm and 880 nm (top plot) or 880 nm and 950 nm (bottom plot). Points are sized in relation to the magnitude of absorption at 660 nm. The median values of AAE_{BC} (0.73 and 1.40 for the bottom and top plots, respectively) are represented by the blue lines, and the interquartile ranges are represented by blue shaded regions.

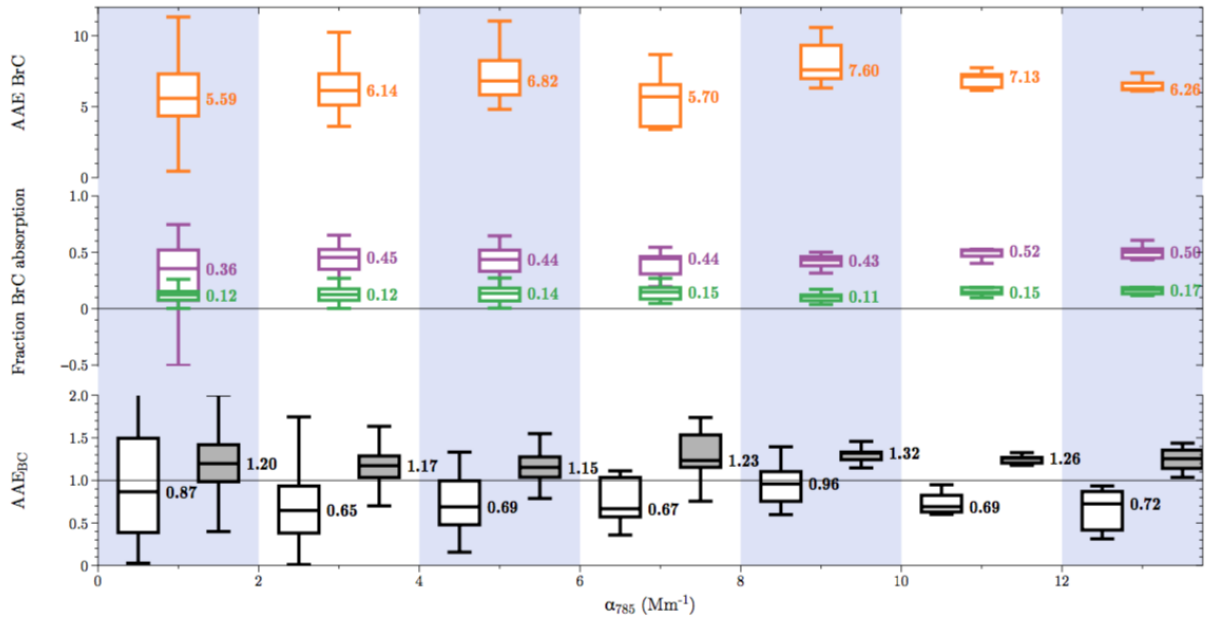


Figure A.5: Representation of AAE_{BC} (white and grey boxes), fraction of absorption due to C_{Br} at 406 nm (purple box and whiskers) and 532 nm (green box and whiskers), and $\text{AAE}_{C_{Br}}$ (orange box and whiskers) for different values of α_{785} . AAE_{BC} was calculated using both the two-wavelength (white boxes) and three-wavelength (grey boxes) approaches. Each box represents the interquartile range (IQR), the horizontal line represents the median, and the whiskers represent ± 1.5 the IQR from the median. The values of the calculated quantities is fairly independent of the magnitude of absorption at 785 nm at 2 Mm^{-1} and higher.

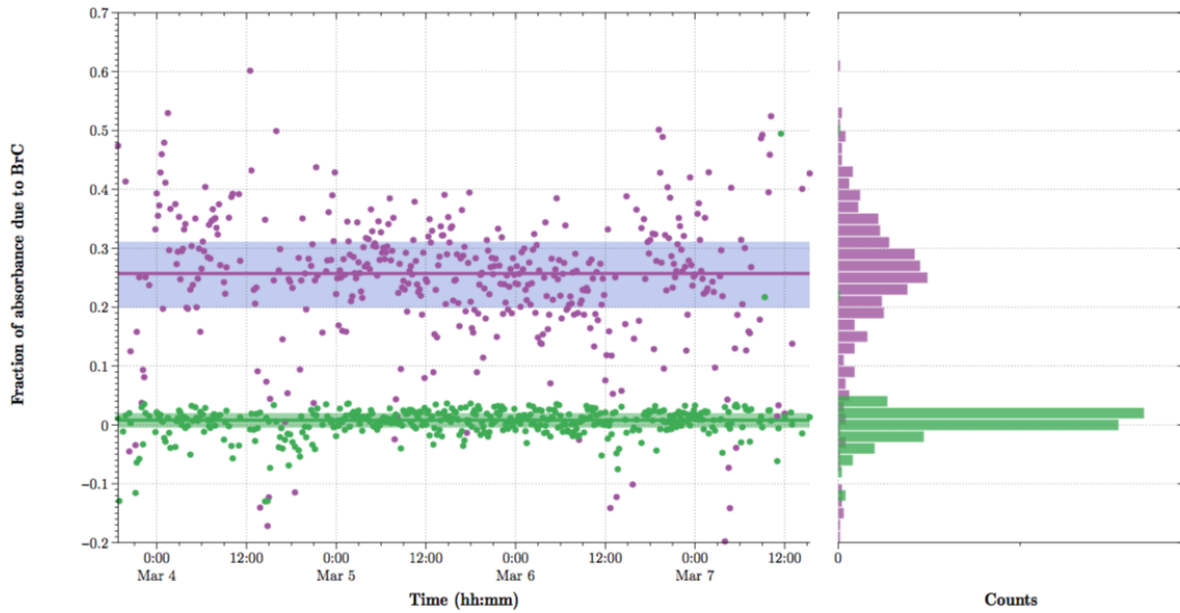


Figure A.6: Time series and histograms of fraction of absorption due to C_{Br} at 406 nm and 532 nm using Equation 6.5 in the manuscript and the three-wavelength approach to calculate $\hat{A}AE_{BC}$ (i.e. assuming absorption at 532 nm, 662 nm, and 785 nm only originates from black carbon). Horizontal lines represent median values (0.26 and 0.01 for 406 nm and 532 nm, respectively) while shaded regions represent interquartile ranges.

References

- (1) Saturno, J. et al. *Atmospheric Measurement Techniques* **2017**, *10*, 2837–2850.
- (2) Lack, D. A.; Cappa, C. D.; Covert, D. S.; Baynard, T.; Massoli, P.; Sierau, B.; Bates, T. S.; Quinn, P. K.; Lovejoy, E. R.; Ravishankara, A. R. *Aerosol Science and Technology* **2008**, *42*, 1033–1041.
- (3) Burrows, J.; Dehn, A.; Deters, B.; Himmelmann, S.; Richter, A.; Voigt, S.; Orphal, J. *Journal of Quantitative Spectroscopy and Radiative Transfer* **1998**, *60*, 1025–1031.
- (4) Petzold, A.; Niessner, R. In *International Conference on Monitoring of Toxic Chemicals and Biomarkers*, ed. by Vo-Dinh, T.; Cammann, K., SPIE: 1993.
- (5) Petzold, A.; Niessner, R. *Applied Physics Letters* **1995**, *66*, 1285–1287.
- (6) Arnott, W. P.; Moosmüller, H.; Rogers, C. F.; Jin, T.; Bruch, R. *Atmospheric Environment* **1999**, *33*, 2845–2852.
- (7) Kramer, L.; Bozoki, Z.; Niessner, R. **Jan. 2001**, *17*.
- (8) Arnott, W. P.; Hamasha, K.; Moosmüller, H.; Sheridan, P. J.; Ogren, J. A. *Aerosol Science and Technology* **2005**, *39*, 17–29.
- (9) Lack, D. A.; Lovejoy, E. R.; Baynard, T.; Pettersson, A.; Ravishankara, A. R. *Aerosol Science and Technology* **2006**, *40*, 697–708.
- (10) Lewis, K.; Arnott, W. P.; Moosmüller, H.; Wold, C. E. *Journal of Geophysical Research* **2008**, *113*, DOI: 10.1029/2007jd009699.
- (11) Ajtai, T.; Filep, Á.; Schnaiter, M.; Linke, C.; Vragel, M.; Bozóki, Z.; Szabó, G.; Leisner, T. *Journal of Aerosol Science* **2010**, *41*, 1020–1029.
- (12) Havey, D. K.; Bueno, P. A.; Gillis, K. A.; Hodges, J. T.; Mulholland, G. W.; van Zee, R. D.; Zachariah, M. R. *Analytical Chemistry* **2010**, *82*, 7935–7942.

- (13) Ajtai, T.; Filep, Á.; Utry, N.; Schnaiter, M.; Linke, C.; Bozóki, Z.; Szabó, G.; Leisner, T. *Journal of Aerosol Science* **2011**, *42*, 859–866.
- (14) Lack, D. A.; Richardson, M. S.; Law, D.; Langridge, J. M.; Cappa, C. D.; McLaughlin, R. J.; Murphy, D. M. *Aerosol Science and Technology* **2012**, *46*, 555–568.
- (15) Gyawali, M.; Arnott, W. P.; Zaveri, R. A.; Song, C.; Moosmüller, H.; Liu, L.; Mishchenko, M. I.; Chen, L.-W. A.; Green, M. C.; Watson, J. G.; Chow, J. C. *Atmospheric Chemistry and Physics* **2012**, *12*, 2587–2601.
- (16) Haisch, C.; Menzenbach, P.; Bladt, H.; Niessner, R. *Analytical Chemistry* **2012**, *84*, 8941–8945.
- (17) Sharma, N.; Arnold, I. J.; Moosmüller, H.; Arnott, W. P.; Mazzoleni, C. *Atmospheric Measurement Techniques* **2013**, *6*, 3501–3513.
- (18) Wiegand, J. R.; Mathews, L. D.; Smith, G. D. *Analytical Chemistry* **2014**, *86*, 6049–6056.
- (19) Radney, J. G.; Zangmeister, C. D. *Analytical Chemistry* **2015**, *87*, 7356–7363.
- (20) Nakayama, T.; Suzuki, H.; Kagamitani, S.; Ikeda, Y.; Uchiyama, A.; Matsumi, Y. *Journal of the Meteorological Society of Japan. Ser. II* **2015**, *93*, 285–308.
- (21) Zhang, X.; Kim, H.; Parworth, C. L.; Young, D. E.; Zhang, Q.; Metcalf, A. R.; Cappa, C. D. *Environmental science & technology* **2016**, *50*, 1681–1690.
- (22) Linke, C.; Ibrahim, I.; Schleicher, N.; Hitzenberger, R.; Andreae, M. O.; Leisner, T.; Schnaiter, M. *Atmospheric Measurement Techniques* **2016**, *9*, 5331–5346.
- (23) Bluvshstein, N.; Flores, J. M.; He, Q.; Segre, E.; Segev, L.; Hong, N.; Donohue, A.; Hilfiker, J. N.; Rudich, Y. *Atmospheric Measurement Techniques* **2017**, *10*, 1203–1213.

- (24) Wang, G.; Yi, H.; Hubert, P.; Deguine, A.; Petitprez, D.; Maamary, R.; Fertein, E.; Rey, J. M.; Sigrist, M. W.; Chen, W. In *Quantum Sensing and Nano Electronics and Photonics XIV*, ed. by Razeghi, M., SPIE: 2017.
- (25) Yu, Z.; Assif, J.; Magoon, G.; Kebabian, P.; Brown, W.; Rundgren, W.; Peck, J.; Miakelyle, R.; Liscinsky, D.; True, B. *Aerosol Science and Technology* **2017**, *51*, 1438–1447.
- (26) Signorell, R.; Cremer, J.; Covert, P. In *Optical Trapping and Optical Micromanipulation XIV*, ed. by Dholakia, K.; Spalding, G. C., SPIE: 2017.

APPENDIX B

BLOCK DIAGRAM OF THE THREE-WAVELENGTH PAS

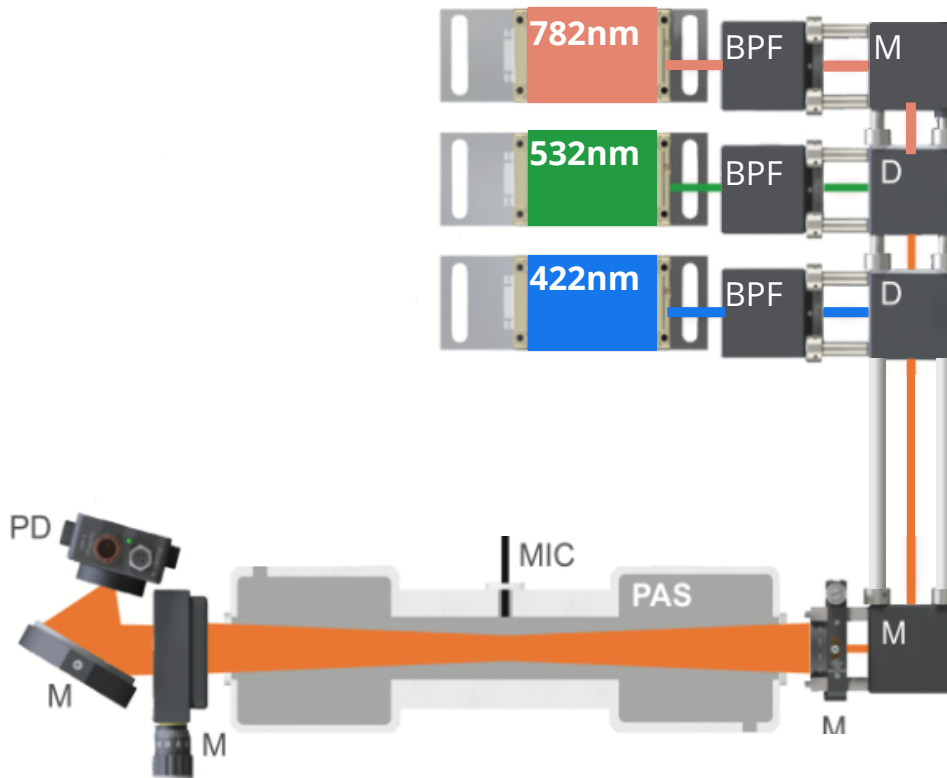


Figure B.1: Block diagram of MultiPAS-III, as built for Dr. Rawad Saleh, UGA College of Engineering. The PAS follows the same basic design as MP-IV (chapter 6) and MP-UV (chapter 8). BPF = bandpass filter (to protect lasers from backreflections at other wavelengths), M = mirror, D = dichroic mirror, PD = photodiode.

APPENDIX C

PAS DATA PROCESSING WITH aeRo

The MultiPAS system outputs two types of files during autonomous running: (1) the `pas.txt` tab-separated document containing both the raw and processed data for the PAS and (2) text files in the `sweeps` folder containing a record of each frequency sweep conducted. Although the main data file contains data that has been processed in real time, it is recommended that data is post-processed from the raw data prior to publication. Although data can be processed in any scientific computing or spreadsheet software, an R package, `aeRo`, has been developed to aid in data processing and is available via GitHub.

The R package `aeRo` has been developed to aid in processing MultiPAS data with R. R is open-source and freely available from the R Project for Statistical Computing. [1] If using R, RStudio, an open-source and freely available IDE for R, is *highly* recommended for ease of using R. In this Appendix, R code is represented with monospaced font.

C.1 aeRo Package

The first step to processing data in R is to install `aeRo`. The package `devtools` will be needed to install `aeRo` from the command line.

```
# Install the devtools package and then load it
options(repos="http://archive.linux.duke.edu/cran/")
install.packages("devtools")
library(devtools)
# Now, use it to install aeRo and then load aeRo
```

```
install_github("alphonse/aeRo")
library(aeRo)
```

You can see the functions available in `aeRo` by clicking on its name in the "Packages" tab within RStudio, executing `help(package = aeRo)`, or with the `ls()` command.

```
ls('package:aeRo')
```

Output:

```
## [1] "averagePower"      "averagePower.waves" "blockMeans"
## [4] "blockMeans.single" "chooseFilterStart"  "compileAeth"
## [7] "convertToAbs"      "convertToExt"      "fillToLength"
## [10] "fitAAE"            "getBg"              "getBg.waves"
## [13] "getTau0"           "importAeth"         "importPAS"
## [16] "plot.abs"          "plot.ssa"
```

More information on any command can be obtained by typing a question mark followed by the command. For example, the help file for `importPAS` is found with `?importPAS`.

C.2 Loading Data into R

To load data into R, first call `importPAS()` and then subset and align the data via the graphical display to the start index of the first filter period using `chooseFilterStart`. `chooseFilterStart` requires user input to the console based on the values selected on the plot. Alternatively, if the start index is already known, you may use the argument `graph = FALSE` and `start = index` to bypass the graphical selector. The function will also make the data length a multiple of `period`.

```
library(dplyr)
setwd("/Volumes/CHEM/Groups/Smith_G/MultiPAS-IV/ambient/20170303")
pas <- importPAS("pas.txt", no.cols = 18) %>%
  # chooseFilterStart() ## typically uncommented, for graphical interface
  chooseFilterStart(graph = FALSE, start = 1430) # only used when start
  point is known, comment otherwise.
```

C.3 Exploring MultiPAS Data

The PAS outputs a tab-separated text file of the raw and processed MultiPAS data. Columns are named according to the content, with the convention Ch1 = shortest laser wavelength. The data file contains the following columns (18 total):

1. **Time:** Sample time in the UNIX/POSIX time standard, "YYYY-MM-DD HH:MM:SS".
2. **micCh1_mV – micCh4_mV:** The raw microphone signal in mV for each channel; if only 3 channels are present Ch4 will be filled with 0.
3. **pdCh1_mV – pdCh4_mV:** The raw photodiode signal in mV for each channel; if only 3 channels are present Ch4 will be filled with 0.
4. **tau_sec:** The ringdown time in seconds; for systems without a CRD, will be filled with 0.
5. **babsCh1_Mm – babsCh4_Mm:** The real-time absorption in 1/Mm for each channel; if only 3 channels are present Ch4 will be filled with 0.
6. **bextCh1_Mm:** The real-time extinction in 1/Mm for each channel; if no CRD is present no extinction is measured and column will be filled with 0.
7. **fres_Hz:** The resonant frequency in Hz used during each sampling period.
8. **filter_state:** A boolean indicating whether the filter is out (0) or inline (1).
9. **elapsedTime_min:** The elapsed time in minutes since the start of the last filter; displays the maximum value during the frequency sweep.

C.4 Processing the Data

With `aeRo`, data can be processed by stringing together a few functions.

```
# Calculate powers, backgrounds, and tau_0, and add to main data.frame
pas <- cbind(pas, getBg(pas)) %>%
  cbind(averagePower(pas)) %>%
  cbind(tau0_s = getTau0(pas$tau_sec))

# Convert data to absorption & extinction
pas <- cbind(pas, convertToAbs(x=pas[, 2:5], bg=pas[, 19:22], p=pas[,
23:26], m=114000)) %>%
  cbind(ext662_Mm = convertToExt(pas$tau_sec, pas$tau0_s))

# Set background periods to NA for cleanliness in plotting
pas[which(pas$filter_state == 1 | pas$elapsedTime_min > 23.5 | pas$
elapsedTime_min < 2.0), 28:32] <- NA

# Add rolling average via "zoo" package, but exclude NAs
library(zoo)
pas[!is.na(pas$abs406_Mm), 28:32] <- rollmean(na.exclude(pas[, 28:32]),
k = 120, fill = NA)
```

C.5 Plotting the Data

`aeRo` includes a plot class specifically for absorption data: `plot.abs()`. Arguments can be passed to `plot()` to change the look of the plot.

```
plot.abs(x = pas$Time, y = pas[, 28:32])
```

APPENDIX D

TROUBLESHOOTING THE PAS

D.1 Common Software Errors

1. *VISA Read/Write: Device not found.* Either the incorrect COM ports have been selected or the USB communication has frozen. In the case of the latter, exit LabVIEW completely and reset the PAS by turning off the main power switch on the control box and disconnecting the USB cable. Reconnect and restart.
2. *VISA Read/Write: Device is valid but VISA cannot open it.* Another program is communicating with one of the PAS's components. Close other programs and restart LabVIEW.
3. *Valve will not switch and/or frequencies will not change.* USB communication broken – exit LabVIEW completely and reset the PAS by turning off the main power switch on the control box and disconnecting the USB cable. Reconnect and restart.
4. *WaveIO Device Not Found.* Known bug with unknown cause. To fix, stop the program, increase the PD and mic device ID's (under the Utilities tab) by 1 and start the program. Then, stop the program, set them back to their original values and start the program again. The errors should go away after the final restart.
5. *Extremely fast acquisition (x-axis) on PD or mic plots.* See WaveIO Device Not Found, above.

D.2 Common Hardware Errors

1. *No Signal or Excessive Noise.* Excessive noise or a cancellation of signal may occur if:
 - (a) *There is an opening on the PAS cell.* Make sure the inlet and outlet are attached to the control box, a gas line, or plugged; check all fittings on the PAS cell to ensure they are tight.
 - (b) *There is an opening on the PAS cell.* Make sure the inlet and outlet are attached to the control box, a gas line, or plugged; check all fittings on the PAS cell to ensure they are tight.
 - (c) *The flow rate is too high.* Lower the flow rate.
2. *High Background.* The cell may be dirty.
3. *Low Laser Powers.* Low laser power may be observed if:
 - (a) The multipass alignment is bad.
 - (b) The optics are dirty.
 - (c) The optics are misaligned.

APPENDIX E

MICROPROCESSOR CODE AND CUSTOM PCB FOR PASs

The MultiPAS instruments are controlled by a 32-bit, 180 MHz ARM Cortex-M4/Teensy 3.6 microcontroller (PJRC.com). The microcontroller is mounted on a custom printed circuit board (PCB, designed by the author and printed by OSHpark.com). Figure E.1 shows a schematic of the PCB. Pins 3, 23, 29, and 35 (in the case of MP-IV, for MP-III only 3 are used) provide square waves (50% duty cycle) near the resonant frequency of the cell to modulate the lasers. The ground pins of the Teensy are connected to the ground plane of the PCB. Pin 4 is connected through a transistor switch (Q1) to switch a 12 V rail on and off to control the integrated pinch valve used for backgrounds; in the final configuration, the locations for LED1 and D1 were left unpopulated on the PCB but could be added at a later date if desired. The Teensy is powered by 5 V supplied through the USB connection. As such, the microcontroller will remain on anytime the PAS is connected to a computer via a USB cable (even if the PAS itself is turned off). The remaining 12 V connectors (bottom right of the schematic) are independent from the Teensy circuit, and are only housed on the PCB for convenience. They serve as a 12 V rail for powering the laser control boxes, fans, the microphone, and other components needing 12 V. Although a Teensy 3.6 is used in the schematic, a Teensy 3.1 should be drop-in compatible if a jumper wire is provided from pin 25 on the bottom of the Teensy to the appropriate BNC connector on the PCB; appropriate changes must also be made in the code.

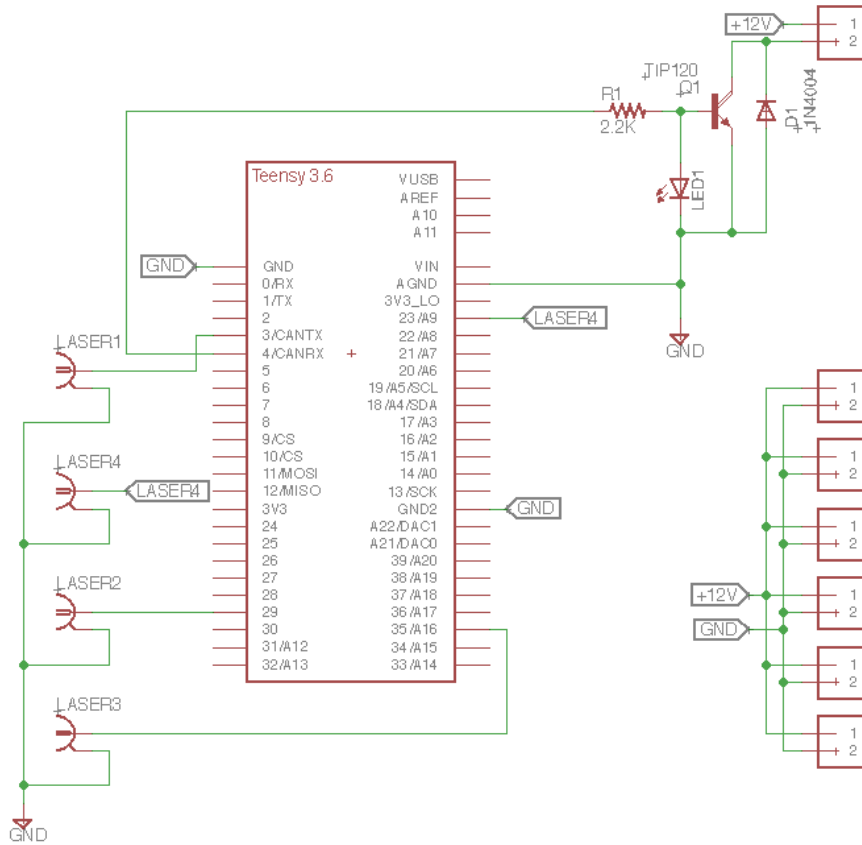
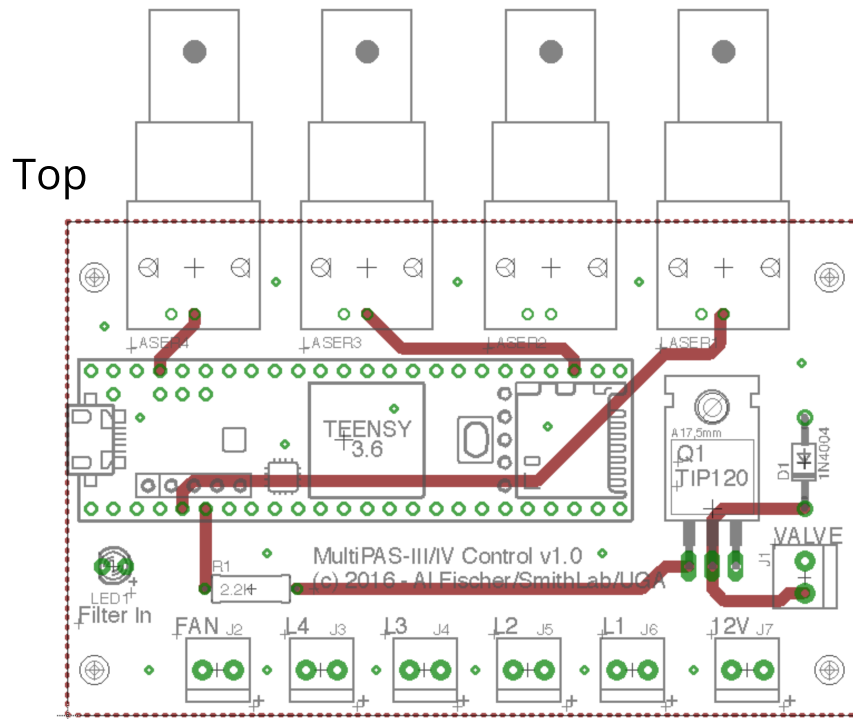


Figure E.1: Electrical schematic of the MultiPAS PCB.



Bottom

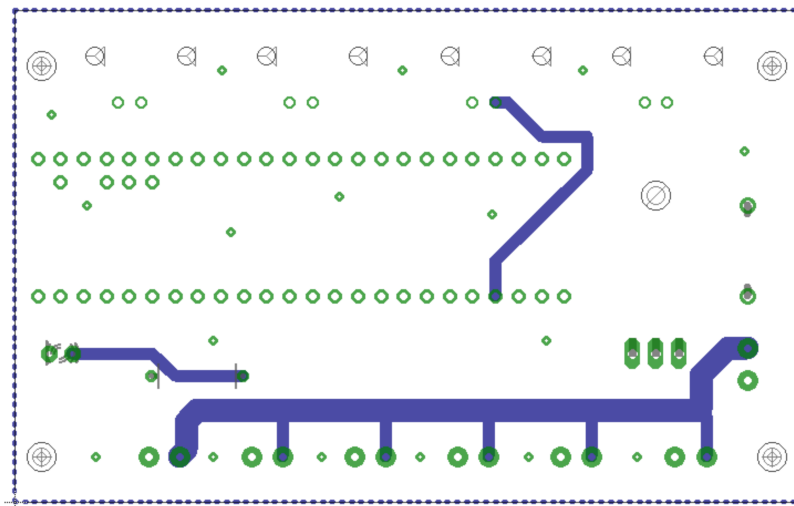


Figure E.2: Layout of the MultiPAS PCB, top (upper panel) and bottom (lower panel).

The Teensy can be controlled through LabVIEW using standard serial communication with a baud rate of 9600 and a newline character as the end of line character. The Teensy knows the following commands:

- **v.1, v.0**: Open and close the main filter valve, respectively.
- **s.f1f2**: Sweep laser modulation frequency from f_1 (in Hertz) to f_2 in 1 Hz steps; $1000 < f < 10,000$.
- **b.f, g.f, r.f, i.f**: Set the frequency of the blue, green, red, or IR laser, respectively, to f (in Hertz); $1000 < f < 10,000$.

These commands are based on the following underlying commands in the Teensy/Arduino code:

- **setupPin(pin, freq, bits)**: Performs the setup routine for the output pins; it should be called once for each laser during initialization.
 - **pin**: The pin in use (int).
 - **freq**: The frequency (in Hz) to initialize the pin to (int).
 - **bits**: The maximum number of bits to use in calculating the duty cycle (int, default 4095).
- **setFreq(laser, pin)**: Set the frequency of a given laser based on serial input.
 - **laser**: A string containing the laser to set the frequency for and the frequency for which to set it; for example, "b.1370" sets the blue laser to 1370 Hz. The function recognizes **b.XXXX, g.XXXX, r.XXXX, i.XXXX**. **pin**: The pin on which to set the frequency (int).

- `sweep(frequencies, pin)`: Sweeps output frequency from desired start to desired end in 1 Hz steps with 2 seconds per step.
 - `frequencies`: Expects format of `XXXXYYYY` where `XXXX` is the desired start frequency and `YYYY` is the desired end frequency; requires $1000 < f_1$ and $f_2 < 10000$ Hz. For example, `s.1355.1385` will sweep the frequencies on pin from 1355 Hz to 1385 Hz. `pin`: The pin on which to sweep the output (int).
- `vSwitch(vState, pin)`: Switches state of transistor switch to control valve.
 - `vState`: Turn valve on or off; `v.0` = off and `v.1` = on (String).
 - `pin`: The digital pin the valve is connected to (int).

The square wave modulation is accomplished by using the PWM output of the Teensy, and choosing digital output pins with distinct timers (FTM0, FTM1, FTM2) for each laser. A working example of code for the Teensy 3.1 follows.

```

int L1pin = 3; // FTM2
int L2pin = 25; // FTM0
int L3pin = 23; // FTM1

int vPin = 4;
int i;
char inChar[10];
String inCharStr;

void setup() {
  Serial.begin(9600);
  analogWriteResolution(12); // provides better resolution on duty cycle
  setupPin(L1pin, 1368, 4095);
  setupPin(L2pin, 1372, 4095);
  setupPin(L3pin, 1370, 4095);
  pinMode(vPin, OUTPUT);
  pinMode(13, OUTPUT);
  digitalWrite(13, HIGH);
}

void loop()
{
  while (Serial.available() > 0)
  {
    inChar[i] = Serial.read();
    i++;
  }

  if (i > 0) inCharStr = String(inChar);
  if (inCharStr.startsWith("b.")) setFreq(inCharStr, L1pin);
  if (inCharStr.startsWith("g.")) setFreq(inCharStr, L2pin);
  if (inCharStr.startsWith("r.")) setFreq(inCharStr, L3pin);
  if (inCharStr.startsWith("s.")) sweep(inCharStr, L2pin);
  if (inCharStr.startsWith("v.")) vSwitch(inCharStr, vPin);

  i = 0;
  inCharStr = " ";
  delay(1000);
}

void setFreq(String laser, int pin) {
  String freqStr = laser.substring(2, 6);
  int freq = freqStr.toInt();
  analogWriteFrequency(pin, freq);
  analogWrite(pin, 4095 / 2);
  // Serial.print("OK - "); Serial.println(freq); // useful for debugging
}

void setupPin(int pin, int freq, int bits) {
  pinMode(pin, OUTPUT);
  analogWriteFrequency(pin, freq);
}

```

```

    analogWrite(pin, bits / 2);
}

void sweep(String frequncies, int pin) {
    String freqStrStart = frequncies.substring(2, 6);
    String freqStrEnd = frequncies.substring(6, 10);
    int endFreq = freqStrEnd.toInt();
    int startFreq = freqStrStart.toInt();
    // Serial.println(startFreq); // useful for debugging
    // Serial.println(endFreq);   // useful for debugging
    // Serial.println(pin);       // useful for debugging
    for (int n = 0; n <= (endFreq - startFreq); n++) {
        analogWriteFrequency(pin, (startFreq + n));
        analogWrite(pin, 4095 / 2);
        digitalWrite(13, LOW);
        delay(2000);
        digitalWrite(13, HIGH);
    }
}

void vSwitch(String vState, int pin) {
    String valveStr = vState.substring(2, 3);
    byte state = valveStr.toInt();
    digitalWrite(pin, state);
    Serial.println("OK");
}

```

APPENDIX F

OVERVIEW OF MULTIPAS LABVIEW PROGRAM

Figure F.1 shows a simplified block diagram to aid in conceptualizing the structure of the MultiPAS LabVIEW program. One portion of the program is constructed using LabVIEW's Asynchronous Message Communication (AMC) VIs. [1] This portion of the program in general handles one-time events, especially those from user input. For example, when the user presses the front-panel button to turn on a laser, the button triggers a case in the AMC message generator that sends a message to the AMC message processor loop, which then executes the command via its own event structure. One advantage of such an approach is that it allows the front panel to remain responsive while the command is executed as the input buttons and the execution loops run in parallel.

The other part of the program functions with a producer/consumer architecture. [2] In general, this structure is used here for repetitive tasks like data acquisition and data processing. For example, a producer loop samples the USB sound card to acquire the raw waveform; it then sends the waveform to the consumer loop where it is processed and plotted. A secondary consumer loop takes data from each of the primary consumers and combines it to calculate absorption and save the data. Again, the loops run in parallel, so this structure allows calculations to occur simultaneously with data acquisition to avoid slow downs and irregularities in data acquisition.

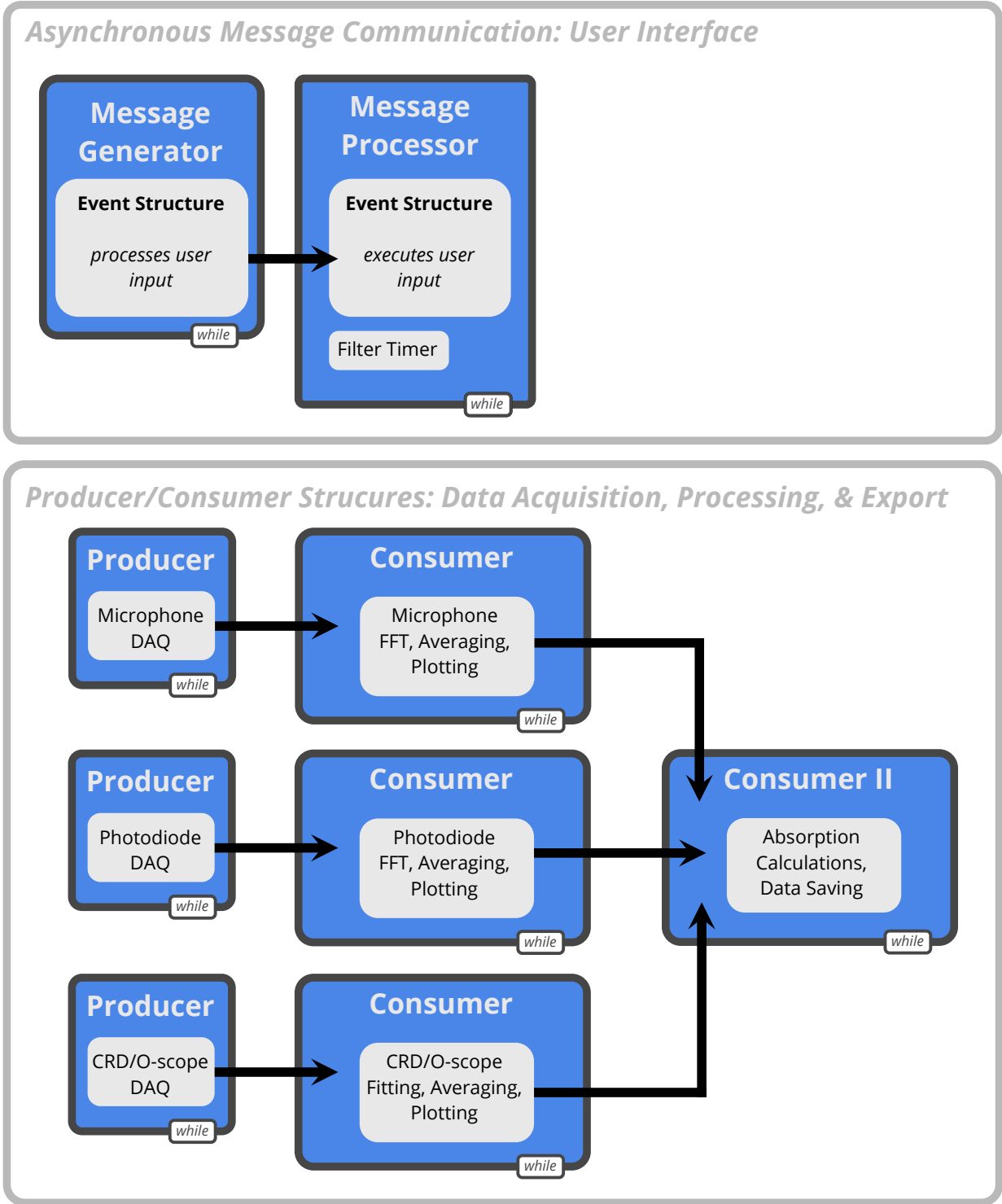


Figure F.1: Conceptual block diagram of the PAS LabVIEW program.

References

- (1) Asynchronous Message Communication (AMC) Library., <http://www.ni.com/example/31091/en/>.
- (2) Application Design Patterns: Producer/Consumer., <http://www.ni.com/white-paper/3023/en/>.

APPENDIX G

MICROPROCESSOR CODE AND DIAGRAM FOR BBCES

The LEDs for the broadband cavity enhanced spectrometer are temperature controlled with thermoelectric coolers (TECs). The star LEDs are affixed to the cold side of a thermoelectric cooler (Mouser PN 739-430801-501, 9.2W/4V) using either thermal epoxy or thermal double stick tape. The hot side of the TEC is affixed similarly to an SM1-threaded aluminum end cap (Thor Labs SM1CP2), which is then threaded into an aluminum heatsink for heat dissipation (Thor Labs HSLT2). The TEC is controlled via a PID loop that is programmed to an Arduino/Genuino Uno. A general block diagram of the system is shown in Figure G.1.

The MAX31850 thermocouple amplifiers were purchased already mounted on a breakout board (Adafruit). K-type thermocouples (Omega Engineering) were epoxied to the aluminum baseplate of the LED and used to measure the temperature. A transistor switch was used to switch a 3.3V power supply (Mouser PN 709-GS18A03-P1J) on and off for each TEC via the PWM output of the Arduino. A working example of the code follows.

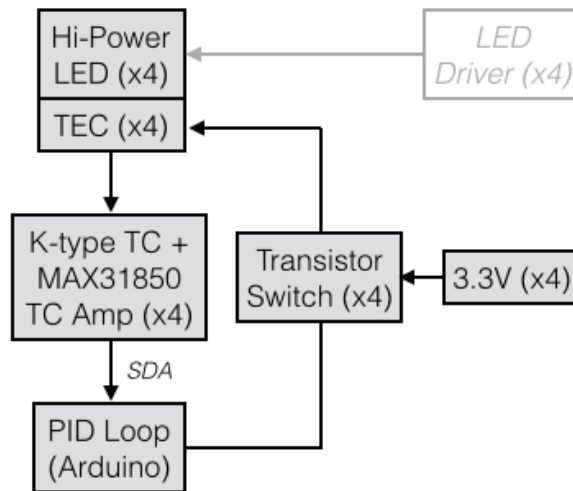


Figure G.1: Block diagram of the TEC control loop.

```

/*
Read and Control Temperature of BBCES LEDs
-----
Uses PWM to control the current through a thermoelectric cooler and
measures the temperature with K-type thermocouple and MAX31850 TC
amplifier. Uses a PID loop as a feedback to control the temperature
for up to four TC amplifiers (on a shared data line) and TECs.

Uses PID library v1.0.1 by Brett Beauregard:
http://playground.arduino.cc/Code/PIDLibrary

Uses the Adafruit's OneWire library:
https://github.com/adafruit/MAX31850_OneWire

and their DallasTemp library:
https://github.com/adafruit/MAX31850_DallasTemp

For BBCES LED control pin 6 is connected to the red LED, pin 9 is
connected to green, pin 10 to blue, and pin 11 to the UV LED.

2015-02-14
AF
*/

#include <PID_v1.h>
#include <OneWire.h>
#include <DallasTemperature.h>

```

```

// Data wire is plugged into port 2 on the Arduino
#define ONE_WIRE_BUS 2

// Setup a oneWire instance to communicate with any OneWire devices
OneWire oneWire(ONE_WIRE_BUS);

// Pass our oneWire reference to Dallas Temperature.
DallasTemperature sensors(&oneWire);

// define variables for PID
double Setpoint, SetpointB, redInput, redOutput, greenInput, greenOutput,
    blueInput, blueOutput, uvInput, uvOutput;
float temps[3];
int count;

// setup PID loops:
PID redPID(&redInput, &redOutput, &SetpointB, 33, 10, 6, DIRECT);
PID greenPID(&greenInput, &greenOutput, &Setpoint, 33, 10, 6, DIRECT);
PID bluePID(&blueInput, &blueOutput, &SetpointB, 33, 10, 6, DIRECT);
PID uvPID(&uvInput, &uvOutput, &Setpoint, 33, 10, 6, DIRECT);

void setup(void)
{
    // start serial port
    Serial.begin(9600);

    pinMode(6, OUTPUT);
    pinMode(9, OUTPUT);
    pinMode(10, OUTPUT);
    pinMode(11, OUTPUT);

    // Start up the library
    sensors.begin();

    // setup for PID:
    Setpoint = 35;
    SetpointB = 25;
    redPID.SetMode(AUTOMATIC);
    redPID.SetControllerDirection(REVERSE);
    greenPID.SetMode(AUTOMATIC);
    greenPID.SetControllerDirection(REVERSE);
    bluePID.SetMode(AUTOMATIC);
    bluePID.SetControllerDirection(REVERSE);
    uvPID.SetMode(AUTOMATIC);
    uvPID.SetControllerDirection(REVERSE);
}

void loop(void)
{
    count = sensors.getDeviceCount();
}

```

```

// call sensors.requestTemperatures() to issue a global temperature
// request to all devices on the bus
sensors.requestTemperatures();

for (int i = 0; i < count; i++) {
  temps[i] = sensors.getTempCByIndex(i);
  Serial.print(temps[i]); Serial.print(", ");
}

Serial.print(millis()); Serial.print(", ");

// adjust output with PID:
if (isnan(temps[0])) redInput = redInput;
else redInput = temps[0];
redPID.Compute();
analogWrite(6, redOutput);

if (isnan(temps[1])) greenInput = greenInput;
else greenInput = temps[1];
greenPID.Compute();
analogWrite(9, greenOutput);

if (isnan(temps[2])) blueInput = blueInput;
else blueInput = temps[2];
bluePID.Compute();
analogWrite(10, blueOutput);

if (isnan(temps[3])) uvInput = uvInput;
else uvInput = temps[3];
uvPID.Compute();
analogWrite(11, uvOutput);

Serial.print(redOutput, 0); Serial.print(", ");
Serial.print(greenOutput, 0); Serial.print(", ");
Serial.print(blueOutput, 0); Serial.print(", ");
Serial.println(uvOutput, 0);
}

```